University of California
Los Angeles

Experimental Atomic Resolution Electron Tomography

A dissertation submitted in partial satisfaction
of the requirements for the degree
Doctor of Philosophy in Physics

by

Mary Cooper Scott

2015

Abstract of the Dissertation

Experimental Atomic Resolution Electron Tomography

by

Mary Cooper Scott

Doctor of Philosophy in Physics

University of California, Los Angeles, 2015

Professor Jianwei (John) Miao, Chair

This work focus on the efforts made to obtain three-dimensional local information at atomic resolution using electron tomography. To realize this long-standing goal, state-of-the art experimental and computational methods were developed. This thesis describes the experimental portion of the collaborative project that has resulted in the first true atomic resolution reconstruction of a material while making no assumptions of crystallinity.

Chapter 1 will give background information on electron microscopy and tomography. Chapter 2 describes the experimental aspects of atomic scale electron tomography using an uncorrected electron microscope. Chapters 3 and 4 follow from this development, and describe the results obtained from implementing this methodology. By reconstructing the data obtained with these methods with an advanced algorithm, atomic scale features were observed for the first time in three dimensions. As a first demonstration, a gold nanoparticle was reconstructed with 2.4 Å resolution, revealing the internal twin boundaries and grain structure of a multiply twinned icosahedral nanoparticle. Next, improvements in data and Bragg filtering revealed the three dimensional atomic structure of edge and screw dislocations, as well as stacking faults, for the first time.

Chapter 5 then discusses the additional experimental considerations needed to employ an aberration corrected electron microscope for the tomographic data. Also in this chapter, a novel needle geometry for tomography is introduced. Chapters 6 and 7 then discuss the results of this methodology applied to both needle and conventional samples. Here, true atomic resolution is finally achieved, with atomic positions being precisely located within the sample, and a point defect identified. With the 3D atomic positions determined, displacement and strain fields can be calculated at high resolution. Work is underway to achieve not only atomic resolution, but also to differentiate between atomic species within the sample.

Electron tomography is a powerful technique for characterization in three dimensions, and this work represents the highest resolution yet achieved, and the first demonstration of true atomic resolution electron tomography. The ability to localize the three-dimensional positions of atoms in a material while making no assumptions of crystallinity, as well as measure point defects and strain, is an important breakthrough and will find broad application in many fields.

The dissertation of Mary Cooper Scott is approved.

Karoly Holczer

Paul S. Weiss

Jianwei (John) Miao, Committee Chair

University of California, Los Angeles

2015

To my family, for their love and support

Table of Contents

1 Introduction **1**

1.1 Transmission electron microscopy and scanning transmission electron microscopy 1

1.1.1 Aberration corrected electron microscopy 4

1.2 Principles of electron tomography 8

1.2.1 Experimental difficulties and limitations 9

1.2.2 Electron tomography reconstruction methods 11

1.2.3 Equally sloped electron tomography 12

2 Experimental implementation of equally sloped tomography for atomic resolution reconstructions **18**

2.1 Motivation 18

2.2 Experimental 19

2.2.1 Sample preparation 20

2.2.2 Data acquisition 24

2.3 Summary 29

3 2.4 Å resolution electron tomography **31**

3.1 Motivation 31

3.2 2.4 Å resolution electron tomography 32
3.2.1 Experimental acquisition of tilt series 32
3.2.2 Reconstruction via equally sloped tomography 33
3.3 Results 38
3.4 Summary 43

4 Three-dimensional imaging of dislocations in nanoparticles at atomic resolution 45
4.1 Motivation 45
4.2 Atomic resolution electron tomography of a 9 nm Pt nanoparticle 46
4.2.1 Experimental data acquisition and reconstruction via EST 46
4.3 Observation of edge dislocations, screw dislocations and stacking faults 48
4.4 Summary 54

5 Atomic resolution tomography on an aberration corrected electron microscope 58
5.1 Motivation 58
5.1.1 Sample geometry and sample stability 59
5.1.2 The TEAM stage 61
5.2 Tomography in a needle geometry 62
5.2.1 Preparation of tungsten needle samples 66
5.3 Data post processing 69
5.4 Summary 71

6 Three-dimensional positions of individual atoms revealed by elec-

tron tomography **74**

6.1 Motivation 74

6.1.1 Data acquisition and image preprocessing 75

6.1.2 Reconstruction, atom tracing, and refinement 77

6.2 Results 81

6.2.1 Identification of individual atoms and a point defect 81

6.2.2 Determination of 3D strain 81

6.3 Summary 87

7 Towards Z-contrast in atomic resolution tomography **93**

7.1 Motivation 93

7.2 Data collection on the TEAM I microscope 94

7.3 Differentiating between atomic species and identifying ordering defects 95

7.4 Summary 97

8 Conclusions **100**

8.1 Thesis Summary 100

8.2 Future Work 101

A Derivations **102**

A.1 The projection-slice theorem 102

A.2 Stage angles required to rotate to a set of equally sloped angles about a specified axis 103

Bibliography **106**

List of Figures

1.1 Scanning transmission electron microscope geometry 2

1.2 Annular detector geometry 3

1.3 The TEAM I microscope 8

1.4 The missing wedge 10

1.5 Back projection reconstruction scheme 11

1.6 Typical tomographic tilt series geometry 13

1.7 The pseudopolar grid 14

1.8 Flow chart of the equally sloped tomography iterative algorithm . 16

2.1 Carbon contamination in STEM 22

2.2 Elimination of carbon contamination 24

2.3 Severe sample vibration 26

2.4 A ronchigram 27

3.1 A tomographic tilt series of a gold nanoparticle 34

3.2 Fourier transforms of each image in a tomographic tilt series of a gold nanoparticle 35

3.3 0° projectional images of a gold nanoparticle acquired before, during, and after a tomographic tilt series 36

3.4 Comparison of measured and calculated projections of a gold nanoparticle . . . 37
3.5 3D resolution estimation of the reconstruction and single atom visualization inside a reconstructed gold nanoparticle . . . 39
3.6 Further demonstration of lattice resolution inside a reconstructed gold nanoparticle . . . 40
3.7 Visualization of the 3D structure of a reconstruced gold nanoparticle 41
3.8 Major crystalline grains inside a reconstructed gold nanoparticle . 42
3.9 Further visualization of crystalline grains inside a reconstructed gold nanopartile . . . 43

4.1 A tomographic tilt series of a platinum nanoparticle . . . 49
4.2 Fourier transforms of each image in a tomographic tilt series of a platinum nanoparticle . . . 50
4.3 0° projectional images of a platinum nanoparticle acquired before, during, and after a tomographic tilt series . . . 51
4.4 Tomographic reconstruction of a platinum nanoparticle with and without Bragg filtering . . . 52
4.5 Atomic steps in grain boundary in a reconstructed platinum nanoparticle . . . 55
4.6 Atomic arrangement of an edge dislocation inside a platinum nanoparticle . . . 56
4.7 Atomic arrangement of a screw dislocation inside a platinum nanoparticle . . . 57

5.1 Optimization of nanoparticle stability during tomographic data acquisition . . . 60

5.2 The TEAM stage 61
5.3 Typical sample geometry in the TEAM stage 62
5.4 Custom SiN grid for the TEAM stage 63
5.5 Needle sample geometry in the TEAM stage 64
5.6 Tomography puck sample holder for the TEAM stage 65
5.7 Wire sample holder for the TEAM stage 65
5.8 High resolution images of needle samples in the TEAM stage . . . 66
5.9 Needle sample tilting geometry 67
5.10 Tungsten tip etching setup 68
5.11 Etched tungsten wire 69
5.12 Scan distortion 71
5.13 Test sample for scan distortion 72

6.1 A tomographic tilt series of a tungsten needle 76
6.2 Slices through the reconstructed tungsten tip 78
6.3 Individual atomic positions in a tungsten needle 79
6.4 Top view of 3D atomic positions in a tungsten needle 80
6.5 Atomic resolution displacement field and point defect in a single atomic layer of a tungsten needle 83
6.6 Observation of 2D strain in a tungsten needle 84
6.7 Atomic resolution displacement field of all atomic layers in a tungsten needle 85
6.8 Strain field of a tungsten needle 86
6.9 Observation of lattice bending in a tungsten needle 88
6.10 Observation of WC_x in a tungsten needle 89

6.11 Strain calculated from a molecular dynamics simulation of a tungsten needle without carbon 90

6.12 Strain calculated from a molecular dynamics simulation of a tungsten needle with carbon 91

7.1 The $L1_0$ phase in iron-platinum bimetallic alloys 94

7.2 A reconstructed iron-platinum nanoparticle 96

7.3 Information recovery in the missing wedge 97

7.4 Z-contrast in a reconstructed iron-platinum nanoparticle 98

7.5 Atomic positions in an iron-platinum particle with species labelled 99

7.6 A missing row of iron atoms in an iron-platinum particle 99

A.1 Geometry of the tungsten tip tomography setup. 103

List of Tables

1.1 Wavelength λ and resolution d for C_3 limited microscopes, with C_3 = 1.2 mm. 6

Acknowledgments

I have been very privileged to study and work at UCLA for the past 6 years. My graduate studies in the Department of Physics and Astronomy have afforded me many opportunities for education and growth, and have put me in contact with so many people that have helped and guided me.

None of this would have been possible without the support of my advisor, John Miao. John trusted me with a challenging new project when I joined his group, and has pushed me to accomplish more than I would have thought possible in my time at UCLA. Through his mentorship I have gained invaluable experience, and I am deeply grateful.

Peter Ercius at the National Center for Electron Microscopy at Lawrence Berkeley National labs has taught me so much about aberration corrected microscopy. I am so grateful to him for sharing his substantial knowledge with me. Without his guidance, many of the atoms seen in this thesis would not be in focus.

I also thank my coworkers in Miao lab and at other groups at UCLA. Chun Zhu and C.-C. Chen were huge parts of the success of this project. Matt Mecklenburg helped me see my first lattice fringes in a microscope, and he and Chris Regan offered wonderful advice and encouragement as I learned electron microscopy. Rui Xu, Li Wu and Yongsoo Yang have also made invaluable contributions to this project.

Also at NCEM, Wolfgang Theis and Colin Ophus have both provided invaluable input to this project. Wolfgang Theis's input into the design of the experiment at NCEM was extremely important, and his work ethic is always an inspiration. Colin has helped with my understanding of the computational aspects of electron microscopy.

Many parts of this text are based on published collaborations. Chatper 3 is a version of "M.C. Scott, Chien-Chun Chen, Matthew Mecklenburg, Chun Zhu,

Rui Xu, Peter Ercius, Ulrich Dahmen, B. C. Regan and Jianwei Miao, 'Electron tomography at 2.4-angstrom resolution', *Nature*, 483, p. 444-447 (2012)", Chapter 4 is a version of "C.-C. Chen, C. Zhu, E. R. White, C.-Y. Chiu, M.C. Scott, B. C. Regan, L. D. Marks, Y. Huang and J. Miao, 'Three-dimensional imaging of dislocations in a nanoparticle at atomic resolution', *Nature*, 496, p. 74-77 (2013)", and Chapter 6 is a version of "Rui Xu, Chien-Chun Chen, Li Wu, M. C. Scott, W. Theis, Colin Ophus, Matthias Bartels, Yongsoo Yang, Hadi Ramezani-Dakhel, Michael R. Sawaya, Hendrik Heinz, Laurence D. Marks, Peter Ercius and Jianwei Miao,'Three-dimensional positions of individual atoms in materials revealed by electron tomography', (2015) (submitted)".

Finally, I owe so many things to my family for their unwavering support. Despite not being happy that I moved across the country from them, my parents Bob and Susie have always encouraged me through the phone, skype and in person visits whenever possible. Thanks also to my sister Katherine for her love and support, and for the inspiration she gives me as we tackle graduate school at our respective schools. To them, and also to my extended family, thank you so much for teaching me to never give up.

My wonderful boyfriend Scotty has kept me caffeinated when there was work to be done, and has shown me so many beautiful parts of California when I needed a break from work. I am so glad I have met him, and he has shown me so much support during my graduate career.

Lastly, I would like to thank my dog, Frankie, who has been my constant companion throughout my entire graduate career.

Vita

2007	B.S. (Aerospace Engineering) and B.S. (Physics), North Carolina State University.
2007–2008	Teaching Assistant, Department of Physics, North Carolina State University.
2007–2009	Graduate Research Assistant, Department of Physics, North Carolina State University.
2009	M.S. (Physics), North Carolina State University.
2009–2015	Graduate Research Assistant, Department of Physics and Astronomy, University of California, Los Angeles.

Publications

J. Miao, C.C. Chen, C. Zhu, **M.C. Scott**, E. R. White, C.Y. Chiu, B.C. Regan, Y. Huang, and L. D. Marks, "Reply to 'Three-dimensional imaging of dislocations', *Nature*, 503, p. E1-E2 (2013)

C. Zhu, C.-C. Chen, J. Du, M. R. Sawaya, **M.C. Scott**, P. Ercius, J. Ciston and J. Miao, "Towards three-dimensional structural determination of amorphous materials at atomic resolution", *Phys. Rev. B (Rapid Commun)*, 88, p. 100201 (2013).

C.-C. Chen, C. Zhu, E. R. White, C.-Y. Chiu, **M.C. Scott**, B. C. Regan, L. D.

Marks, Y. Huang and J. Miao, "Three-dimensional imaging of dislocations in a nanoparticle at atomic resolution", *Nature*, 496, p. 74-77 (2013).

M.C. Scott, Chien-Chun Chen, Matthew Mecklenburg, Chun Zhu, Rui Xu, Peter Ercius, Ulrich Dahmen, B. C. Regan and Jianwei Miao, "Electron tomography at 2.4-angstrom resolution", *Nature*, 483, p. 444-447 (2012).

M.C. Scott, D.R. Stevens, J.R. Bochinski, and L.I. Clarke, "Dynamics within Alkylsiloxane Self-Assembled Monolayers Studied by Sensitive Dielectric Spectroscopy", *ACS Nano.*, 2, p. 2392-2400 (2008).

S.S. Ojha, D.R. Stevens, T.J. Hoffman, K. Stano, R. Klossner, **M.C. Scott**, W. Krause, L.I. Clarke, and R.E. Gorga, "Fabrication and Characterization of Electrospun Chitosan Nanofibers Formed via Templating with Polyethylene Oxide", *Biomacromolecules*, 9, p. 2523-2529 (2008).

CHAPTER 1

Introduction

1.1 Transmission electron microscopy and scanning transmission electron microscopy

The idea that electrons could behave as a wave, with a wavelength much smaller than visible light, was introduced by de Broglie in 1925 [1, 2]. Around the same time, Busch showed that that an axially symmetric magnetic field could act as a lens for electrons [2]. The first working prototype of an electron microscope was realized by Knoll and Ruska in the 1930s [1, 2]. Less than a year after Ruska's first demonstration, an electron microscope broke the resolution limit of a light microscope [1]. It did not take long for these achievements to be commercialized, and within 5 years Siemens made electron microscopes available for purchase around the world [1].

Since Ruska's original demonstration, many electron microscope configurations have been developed. The most familiar, a conventional transmission electron microscope (TEM), is configured similarly to an optical microscope. A parallel beam of coherent electrons formed from a condenser lens system is incident on a

thin (<200 nm) sample. The electrons typically have energies in the range of 20 keV-1 MeV, and a current of 1-10 nA [1]. The electrons interact with the sample both elastically and inelastically, and those interactions are the mechanism for image contrast in an electron micrograph.

Not long after the invention of the conventional TEM, scanning analogs were built- the scanning electron microscope (SEM) and the scanning transmission electron microscope (STEM) [2]. In a STEM, the beam is focused into a sharp probe by the condenser lens system. This probe is then rastered across the sample in a grid shape. At each location on the grid, scattered electrons are collected, and an intensity map is formed. In the case of annular dark field (ADF) imaging and high-angle annular dark field imaging (HAADF) STEM, an annular detector is used to collect only the electrons that are scattered to higher angles, excluding the direct beam. The direct beam intensity can also be collected in this point-by-point manner, forming a bright field (BF) STEM image. The geometry of the STEM probe and these detectors is shown in Figure 1.2. If the direct beam is imaged on a pixelated detector, a convergent beam electron diffraction pattern is obtained. Alternatively, the direct beam can be energy filtered to give information about the atomic species present in the sample.

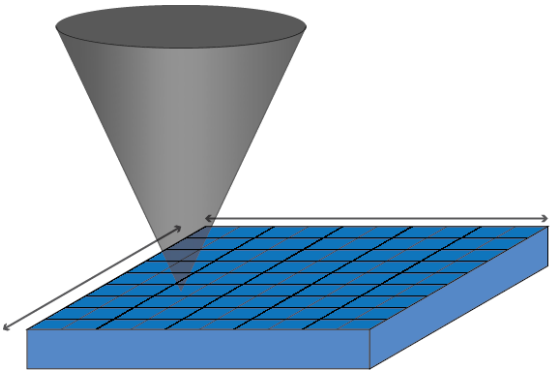

Figure 1.1: To form a STEM image, the beam is focused into a small probe. This probe is rastered over the sample in a grid shape, and at each grid location, scattered electrons are collected by detectors underneath the sample.

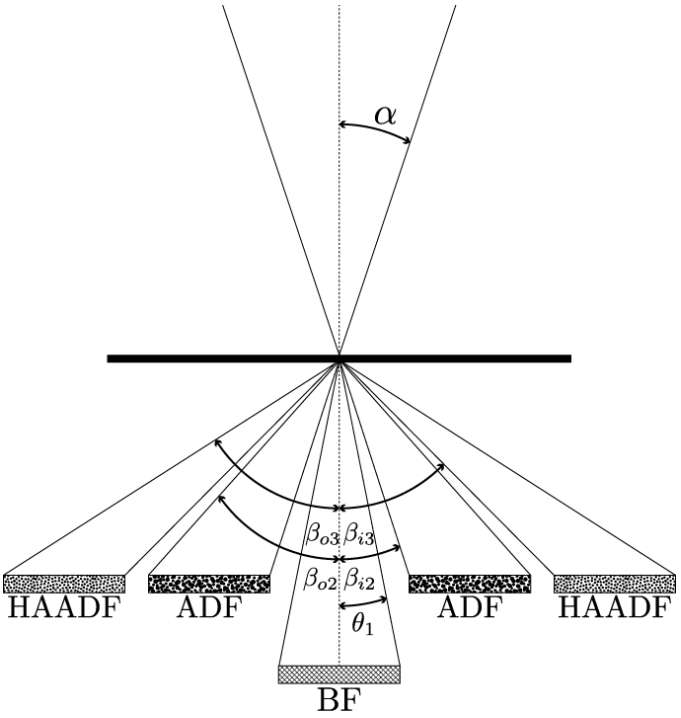

Figure 1.2: STEM geometry, showing the focused electron beam with semiangle α, and BF, ADF, and HAADF. The bright field outer collection semiangle is θ_1 and the ADF and HAADF inner and outer collection semiangles are $\beta_{o,i2}$ and $\beta_{o,i3}$, respectively.

STEM has several advantages over TEM, particularly for electron tomography. In high resolution TEM imaging of crystalline samples, the coherent beam introduces nonlinear effects when crystalline samples are imaged at high resolution [3]. ADF- and HAADF-STEM, however, form images that are linear to first order. Additionally, HAADF-STEM has built in Z-contrast, as most of the electrons that are scattered to high angles have undergone Rutherford scattering. Rutherford scattering is proportional to $\sim Z^2$, therefore elements with a higher atomic number Z appear brighter in a HAADF-STEM image.

1.1.1 Aberration corrected electron microscopy

In an electron microscope, focusing and image formation are achieved via electromagnetic lenses. Within the lens, a radially symmetric magnetic field alters the path of electrons traveling down the microscope [2, 4, 5]. Electron lens strength can be tuned by changing or even reversing the current in the coils, allowing for flexibility in the configuration of the electron microscope. To determine the resolution limit of electron microscopes, Ruska originally replaced the wavelength in equations describing light optics with the wavelength associated with the electrons in the microscope [2]. These diffraction-limited electron microscopes would theoretically have incredibly high resolving power. However, in a paper published in 1936, Scherzer pointed out that electromagnetic lenses are spherical, and therefore the resolution of electron microscopes will be limited due to the aberrations introduced by those lenses [6, 7].

For an electron beam, the non-relativistic de Broglie wavelength is given by

$$\lambda = h/p \tag{1.1}$$

where h is Planck's constant and p is the momentum of the electron. Since beam energies in electron microscopes are commonly given in terms units of eV, it is convenient to equate the accelerating voltage V to the kinetic energy of the

electrons and write

$$p = m_0 v = (2 m_0 e V)^{\frac{1}{2}}. \tag{1.2}$$

Since the electrons are moving at a significant fraction of the speed of light, it is necessary to adapt Equation 1.1 to the special relativistic case by using $p = \gamma m_0 v$ and $E = \gamma m_0 c^2$, where $\gamma = (1 - \frac{v^2}{c^2})^{-\frac{1}{2}}$. Equation 1.1 is then

$$\lambda = \frac{h}{m_0 v} \sqrt{1 - \frac{v^2}{c^2}} \tag{1.3}$$

or, in terms of the accelerating voltage V,

$$\lambda = \frac{h}{\sqrt{2 m_0 e V (1 + \frac{eV}{2 m_0 c^2})}}. \tag{1.4}$$

Substituting numbers into Equation 1.4 gives λ =1.97 pm for a 300 keV electron beam. Wavelengths for other common operating voltages are given in Table 1.1. For a diffraction-limited STEM, this would give a resolution of about 2 pm for a 300 keV operating voltage. However, most un-corrected microscopes are limited to >1 Å resolution. This is entirely due to the poor focusing power of the electromagnetic lenses used in electron microscopes. These optical elements in the microscope- the pre-sample condenser system and the post-sample imaging lens system- induce aberrations that are analogous to those found in light microscopes. In fact, as shown in Table 1.1, resolution is about two orders of magnitude higher than the wavelength.

"Geometric aberrations" refer to changes in the electron path induced by the spherical nature of the electromagnetic lens [5]. Additional types of aberrations are parasitic aberrations, which arise from imperfect machining of the lenses, or chromatic aberrations, which occur when electrons of slightly different energies have different focal planes [5]. Common aberrations include astigmatism, coma, and spherical aberration. These aberrations limit the spatial resolution of the microscope by altering the phase of the electrons, which in turn alters their trajectory [4]. In the case of TEM, this can be thought of as attenuation of the

Table 1.1: Wavelength λ and resolution d for C_3 limited microscopes, with C_3 = 1.2 mm.

Operating Voltage [keV]	λ [pm]	d [Å]
1000	0.87	0.72
300	2.0	1.3
200	2.5	1.6
80	4.2	2.3

transmission of high spatial frequencies transmitted, which correspond to the fine details of an image. In STEM, these aberrations limit the focusing power of the condenser lens system, resulting in a minimum size to which the scanning probe can be focused. In uncorrected microscopes, third-order spherical aberration, C_3 (often referred to as C_s) is the limiting factor on resolution [4, 5]. The resolution of a C_3 limited microscope in STEM mode is given by

$$d = 0.43 C_3^{\frac{1}{4}} \lambda^{\frac{3}{4}}. \tag{1.5}$$

C_3 values depend on the incident beam energy (*i.e.*, the wavelength) and the geometry of the lens system. C_3 values are typically on the order of 1-2 mm, with values of 0.5 mm being found in instruments with optimized objective lenses. For an uncorrected Titan STEM, the C_3 value is 1.2 mm, which by equation 1.5 gives a resolution of 1.36 Å for STEM at 300 keV. Table 1.1 shows resolution values for a typical C_3-limited microscope.

As electron microscopy developed, many advances were made to improve resolution. These include advances in electron sources for better beam coherency, and more stable power supply and lens systems for overall instrument stability. However, without a way to correct the geometric and chromatic aberrations of

the lenses, resolution of electron microscopes would be limited as predicted by Scherzer. Scherzer actually proposed a solution to the aberration problem- he showed that multipole lenses, with non-rotationally symmetric fields- could correct these aberrations [7, 8]. After much work on this subject, aberration correction was finally achieved in the 1990s [7, 9, 10]. The additional lens systems, or aberration correctors, do not add any magnification power to the microscope, but merely correct the aberrations introduced by the spherical lens. The aberration correctors consist of higher order (quadrapole, hexapole, or octapole) magnetic lenses, and they require special software first to measure the aberrations and then to correct them [7, 9, 10].

The Transmission Electron Aberration-Corrected Microscope (TEAM) I (Fig. 1.3) at the National Center for Electron Microscopy at Lawrence Berkeley labs is one of the most advanced corrected microscopes in the world. The TEAM I is double corrected, meaning both the geometric and chromatic aberrations are corrected in the post-sample optic system. Before the sample, the condenser lens system also contains a geometric aberration corrector. A larger beam convergence angle, α, is used to create a much smaller STEM probe (Figure 1.2). Without C_3 as a limiting factor on the resolution, the probe diameter is given by

$$d = \frac{0.61\lambda}{\alpha} \tag{1.6}$$

which for a 300 keV electron beam and 30 mrad probe is about 40 pm. Practically speaking, the microscope will be limited by higher order aberrations to a resolution slightly worse than predicted by Equation 1.6. The STEM resolution of the TEAM I is limited by higher-order aberrations to 50 pm.

Having such a large convergence angle, however, negatively affects the depth of field in STEM. The depth of field for aberration corrected STEM is about 10 nm, compared to $\sim$50 nm for an uncorrected machine [11, 12]. Therefore samples must be very thin to be imaged in an aberration-corrected STEM.

Figure 1.3: A publicity photo of the TEAM I, showing the author at the operator station, which is located outside of the room containing the microscope. The TEAM I is one of the most advanced electron microscopes in the world. It is located at the National Center for Electron Microscopy at Lawrence Berkeley National Labs in Berkeley, California.

1.2 Principles of electron tomography

In general, tomography is a method of reconstructing an object's interior in three dimensions from a series of two-dimensional (2D) projections obtained as a sample is rotated about a tilt axis. At each tilt angle, a projection is obtained. After the tilt series is completed, a mathematical reconstruction method is applied to obtain a three-dimensional (3D) reconstruction of the object. Tomography is used in many disciplines, using X-rays or electrons to form the two-dimensional projections. The general term "tomography" implies tilting about only one axis.

Electron tomography was introduced in 1968 and has primarily been used for biological applications since then [13]. However, the non-linear effects in TEM imaging that arise from coherent diffraction and channeling create large artifacts and error in tomographic reconstructions that have made high resolution TEM (HRTEM) tomography of crystalline or polycrystalline samples impossible. With the improvement of STEM resolution, however, STEM tomography became a

viable option for materials science samples where the features of interest are on the atomic scale. If the assumption that the sample is a perfect crystal can be made, then techniques such as discrete tomography [14] or one-shot quantitative analysis [15] may be used. However, to see defects and deviations from the perfect crystal lattice, or to understand the atomic arrangement of polycrystalline samples, a general tomographic method that makes no assumptions about a sample's crystal structure is needed.

1.2.1 Experimental difficulties and limitations

Prior to this work, tilt axis tomography was limited by many challenges. For example, specimens cannot usually be tilted beyond $\pm 70°$, which creates a "wedge" of missing information termed the missing wedge (Fig. 1.4). Radiation damage to the sample caused by the incident electron beam limits the number of projections that can be taken in the microscope. Additionally, after data acquisition, the projections must be aligned with atomic precision. These difficulties previously limited the resolution of electron tomography to 1 nm^3 [16, 17].

An additional consideration, in the case of STEM tomography, is carbon contamination. Carbon contamination occurs when mobile hydrocarbons present on the sample surface move into the beam area and are carbonized (*i.e.*, cross-polymerized) [18]. This results in thick layers of carbon in the beam direction, which adversely affect resolution. In the case of TEM this problem is minimal, as mobile hydrocarbons encounter the edge of the beam first, and do not build up in the center of the area of interest. However, in the case of STEM, this buildup occurs as the probe scans directly over the area of interest [19]. Contamination has also been shown to build up faster as beam current density increases [18], which means that STEM imaging is highly susceptible to carbon contamination.

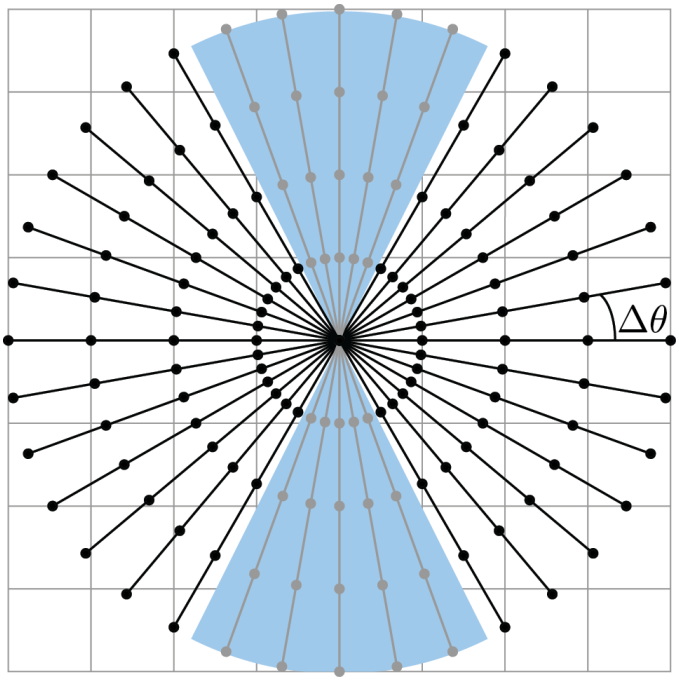

Figure 1.4: A representation of a tilt series of a 2D object, where the projections are the 1D lines shown. The area highlighted in blue shows a range high angle projections that are not accessible, forming a wedge of missing information.

1.2.2 Electron tomography reconstruction methods

A simple example of a tomographic reconstruction method is back projection. Back projection is a real space reconstruction method that integrates each pixel value of a projection along a line determined by the projection angle, θ, and the distance of the pixel from the rotation axis (Fig. 1.5). Back projection reconstruction techniques require many projections to reduce artifacts caused by the higher sampling at low spatial frequencies in Fourier space [20]. Various filters or weighting schemes can be applied to overcome the problem of higher intensity aggregating at the center of the reconstruction [21]. The process of taking experimental tomographic data is similar to a forward Radon transform, and back projection is the inverse Radon transform [22].

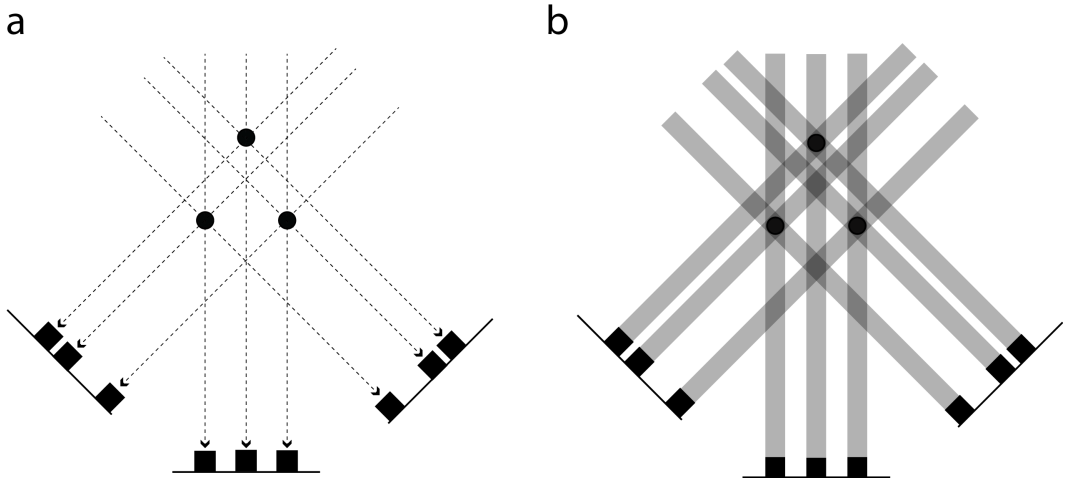

Figure 1.5: Tomographic projection and reconstruction by back projection. a) Three 1D projections of a 2D object at different angles. b) Reconstruction by simple back projection. The intensity of the five features is reproduced using this method, but there are significant artifacts.

Another popular method is an iterative method termed simultaneous iterative reconstruction technique (SIRT). This technique improves upon simple back projection by iteratively updating the reconstruction by comparing simulated pro-

jections (produced from the reconstruction by a Radon transform) to the experimental projections [23]. The reconstruction is then updated according to the difference between the calculated and experimental projections. In this way, SIRT converges on a reconstruction that is consistent with the experimental data [23].

A more elegant approach to tomographic reconstruction is to rely on the *projection-slice theorem*, which states that the two-dimensional Fourier transform of a linear projection at a tilt angle α of a three-dimensional object is equivalent to a two-dimensional central slice of the three-dimensional Fourier transform of the object at that same angle α (Appendix A). Therefore, if the two-dimensional projections of a tilt series are Fourier transformed, and assembled in three-dimensional Fourier space, one could simply apply an inverse Fourier transform to obtain the reconstructed object. However, tomography data points are sampled on a polar grid, and therefore so will be the Fourier slices [13]. Figure 1.6 shows the polar sampling of a typical tomographic tilt series, with equal angle increments, in comparison to a Cartesian grid. Unlike the case of a Cartesian grid, there is no fast, accurate inverse polar Fourier transform [24]. Therefore, this method requires interpolating to a Cartesian grid, which introduces error and artifacts into the reconstruction [25].

1.2.3 Equally sloped electron tomography

Most tomographic tilt series are collected on a polar grid with equal angle increments between neighboring projections. However, this is not a necessary condition for tomographic data acquisition or reconstruction. In fact, by using a tilt scheme with equally sloped increments, the data can be directly inverted from Fourier space and the need to interpolate to employ the projection-slice theorem is lifted. By collecting data with equally sloped increments, the tomographic data points can be placed exactly on a grid termed the *pseudopolar grid* (Fig. 1.7), which

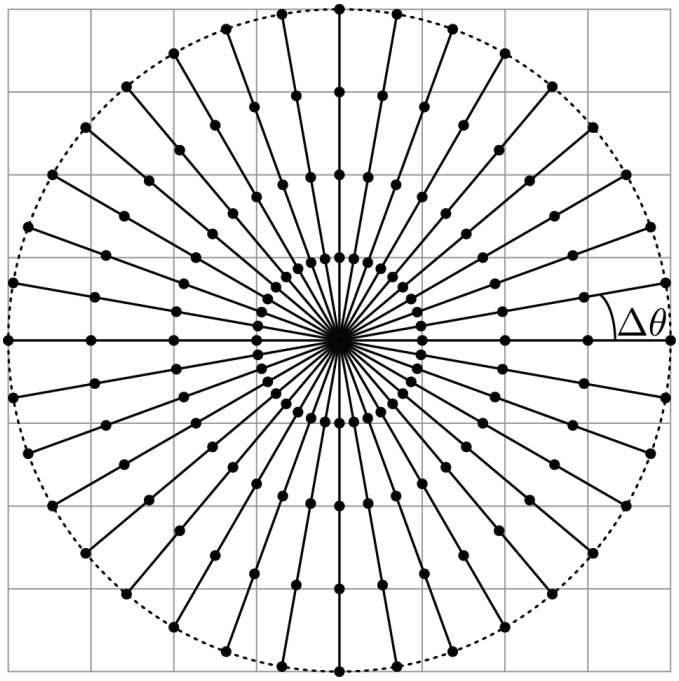

Figure 1.6: Tomographic tilt series are usually collected with equal angle increments ($\Delta\theta$). This results in data sampled on a polar grid. The polar grid points (black) do not sample a Cartesian grid (gray).

consists of concentric squares, rather than concentric circles as in a polar grid.

When the projections of a tilt series are acquired with equal slope increments, it has been shown that a direct fast Fourier transform, the pseudopolar fast Fourier transform (PPFFT)[26], exists between a pseudopolar grid and a Cartesian grid. Figure 1.7 shows a pseudopolar grid and the PPFFT. For an $N \times N$ Cartesian grid, the corresponding pseudopolar grid is defined by a set of $2N$ lines, each line consisting of $2N$ grid points mapped out on N concentric squares. The $2N$ lines are subdivided into a horizontal group (in blue) defined by $y = sx$, where s is the slope and $|s| \leq 1$, and a vertical group (in red) defined by $x = sy$, where $|s| \leq 1$; the horizontal and vertical groups are symmetric under the interchange of x and y, and $\Delta s = 2/N$. When these conditions are met, the PPFFT and its inverse algorithm are mathematically faithful [26].

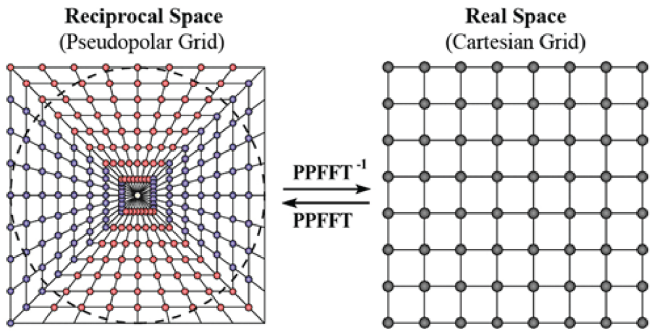

Figure 1.7: The pseudopolar grid (left) samples Fourier space on grid points located on concentric squares, rather than concentric circles as for a polar grid. The PPFFT and its inverse, the PPFFT^{-1} are accurate and can be expressed as fast Fourier algorithms.

Compared to other data acquisition approaches, the EST data acquisition approach is only different in that it acquires projections with equal slope increments in order to use the PPFFT. Although the PPFFT and its inverse provide an exact Fourier transform between the Cartesian and pseudopolar grids, there are experi-

mental difficulties that limit its direct application to electron tomography. First, the tilt range has to be from -90° to $+90^\circ$. Second, the number of projections in a tilt series needs to be $2N$ for an $N \times N$ object. These issues can be mitigated by using the PPFFT and its inverse as the kernel in an iterative reconstruction method [20, 25, 27, 28]. In Figure 1.8, a flow chart of the iterative EST method is shown. First, it is necessary to convert the electron micrograph projections to Fourier slices in the pseudopolar grid. As illustrated in Figure 1.7, the distance between the sampling points on the individual $2N$ lines of the pseudopolar grid varies from line to line. In order to calculate the Fourier slices from the projections, a fractional Fourier transform (FrFT) is used to vary the distance between grid points of the individual projection. The discrete FrFT of a vector x described by $x = (x_j, 0 < j < N)$ is

$$G_k(x, \alpha) = \sum_{j=0}^{N-1} x_j e^{-2\pi i \alpha k j} \tag{1.7}$$

where the parameter α is used to vary the output sampling distance of the Fourier slices [29]. The FrFT is actually a more general form of discrete Fourier transform,

$$F_k(x) = \sum_{j=0}^{N-1} x_j e^{\frac{-2\pi i k j}{N}} \tag{1.8}$$

where the discrete Fourier transform corresponds to the special case of the $\alpha = \frac{1}{N}$. From this relation, it is clear that the FrFT is not an interpolation, and introduces no more error than the discrete Fourier transform itself.

After this step, the inverse PPFFT is applied to obtain a 3D image in real space. A 3D support is defined that is larger than the reconstructed object. Any negative-valued voxels inside the support and all voxel values outside the support are set to zero, and a new 3D image is obtained. The forward PPFFT is applied to the new image and a set of calculated Fourier slices is obtained. Then the corresponding calculated Fourier slices are replaced with the measured ones (the

original data), and the remaining slices are kept unchanged. This iterative process, shown in Figure 1.8, is then repeated with each iteration monitored by an error metric, and the algorithm is terminated after reaching a maximum number of iterations. The EST method aims for solving the missing data by iterating between real and Fourier space while reducing the number of unknowns by applying constraints [20, 25, 27, 28].

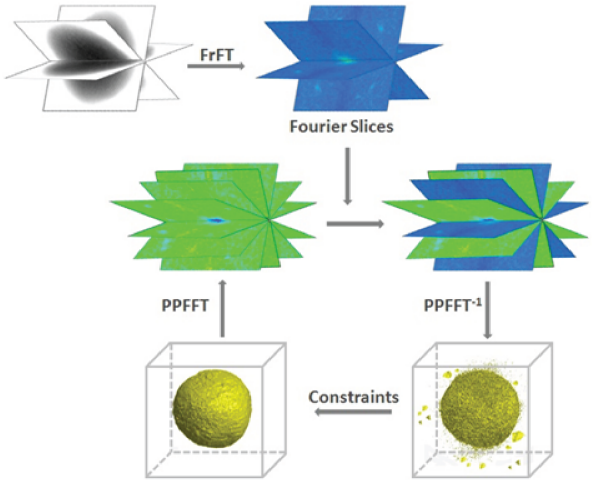

Figure 1.8: Schematic layout of the iterative EST method. The measured projections are first converted to Fourier slices by the FrFT. The algorithm iterates back and forth between real and reciprocal space using the PPFFT and its inversion. In real space, the negative-valued voxels inside the support and the voxel values outside the support are set to zero (*i.e.*, constraints are applied). In reciprocal space, the corresponding calculated slices are updated with the measured ones (in blue) and the remaining slices (in green) are unchanged. The algorithm is terminated after reaching a maximum number of iterations.

To achieve an atomic resolution reconstruction, the projections in a tilt series have to be aligned to a common axis (not necessarily the true tilt axis, but parallel to it) with atomic scale precision in both the X- and Y-axes, where the Y-axis represents the tilt axis and Z-axis the beam direction. Typically, the projections

of a tilt series are aligned after acquisition using either cross correlation or fiducial markers (gold nanoparticles) [13]. However, neither of these methods have have been able to achieve atomic resolution accuracy. Therefore prior to reconstruction with EST, a center of mass method is used to align the projections with sub pixel accuracy [30]. This method calculates the center of mass of the object of interest, and uses this as a unique point to align to in the projection. When a 3D object is tilted around the Y-axis from 0° to 360°, the CM of the object forms a circle. However, in the special geometry where the center of mass (CM) coincides with the origin of the X-axis, this circle becomes a point. To determine the CM in this special geometry, we projected each 2D projection onto the X-axis and calculated the CM along the X-axis,

$$X_{CM} = \frac{\sum_i x_i \rho(x_i)}{\rho(x_i)}. \tag{1.9}$$

The projections can be aligned in the Y direction by projecting again onto the rotation axis and fitting. The CM alignment method is ideally suited to ADF- and HAADF-STEM projections, where the signal-to-background ratio is high [30, 31]. This alignment technique has been shown to be able to align projectional data with sub-pixel accuracy, even in the case of high noise [30, 31]. Previously, EST has been shown to recover missing information from the missing wedge and to improve resolution and contrast in reconstructions compared to backprojection and SIRT [20]. The EST reconstruction algorithm was originally developed by Miao [25] to solve the phase retrieval problem in coherent X-ray diffraction. Previous applications of EST include biological and materials science applications [20, 25, 27, 28], and EST has recently been adapted to electron tomography [30, 31].

CHAPTER 2

Experimental implementation of equally sloped tomography for atomic resolution reconstructions

2.1 Motivation

Revealing a material's internal atomic structure is the goal of many materials science characterization techniques. While many methods can accurately determine the average structure, a general local 3D atomic resolution imaging technique is needed. With the increase in popularity of scanning transmission electron microscopy for materials science samples, STEM electron tomography is a natural choice. Previously, the highest resolution attained by STEM tomography was 1 nm^3 [16], [17]. However, recently our group has reconstructed a Au nanoparticle with lattice resolution [30] and, with improved experimental quality and a Bragg filtering method, were able to observe stacking faults, edge dislocations and screw dislocations as well as individual atoms in a Pt nanoparticle [31]. While the novel

reconstruction method used to obtain these results played a large role in the success of these experiments, sample preparation and data acquisition are also critical in high-resolution tomography.

To obtain an atomic scale resolution reconstruction, every aspect of sample preparation and data acquisition must be optimized. While experimental details may seem trivial compared to other aspects of the project, these details, often overlooked, have been absolutely necessary to obtaining the quality input data that resulted in the highest resolution ever tomographic reconstruction. The procedures discussed in this chapter will focus on uncorrected electron microscopy. Implementation of tomography on an aberration corrected microscope will require different considerations, and will be discussed in Chapter 5.

2.2 Experimental

In a tomography dataset, upwards of 100 projectional images will be taken of the same particle or area. To withstand such a radiation dose, and maintain good quality throughout the angles sampled, many experimental aspects must be considered. Firstly, the particle itself must remain stable and in the same position throughout the data acquisition. Another limit on the amount of data obtained is the missing wedge, that is, specimens cannot usually be tilted a full $\pm 90^{\circ}$, resulting in a wedge of missing information. Individual projections must also be of the highest possible quality. Any mechanical drift of the stage, vibration of the stage or sample, charging of the sample, or contamination of the sample will degrade the images.

2.2.1 Sample preparation

A good tomography sample needs to be clean, stable, able to be tilted to a high angle, conductive and able to withstand any necessary heat treatment. These properties can be controlled in part by the choice of substrate and the subsequent treatment of the substrate.

As mentioned above, minimizing the missing wedge is necessary for high resolution reconstructions, as the missing information in the missing wedge results in elongation of features and loss of resolution in the beam direction [17]. The upper tilting limit can be set by either the microscope itself (sample tilt range is limited by tilt range of the microscope to $\pm 80^\circ$ for a typical FEI compustage) or the geometry of the sample support. A typical TEM support grid consists of a 3 mm thicker support frame with smaller regions that are very thin (30 nm or less). For thin sample supporting frames (for example a typical copper support grid, which is 25 μm thick), the stage itself limits the tilt range. For support frame thicknesses approaching 100 μm or more, the angular range should be calculated to determine where on the grid the area of interest needs to be for maximum tilt range. Therefore for thicker grids with thin viewing windows, such as those offered by TEMwindows, the area of interest must be close to center of the grid along the rotation axis. Tilting over a range of least $\pm 65^\circ$ is critical to achieving high resolution results in general. For an uncorrected microscope, $\pm 75^\circ$ is desirable. Another consideration here is that as the sample is tilted, the apparent thickness of the sample increases as $t' = t/\cos(\theta)$, where t' is the apparent thickness, t is the sample thickness at 0°, and θ is the tilt angle. This is particularly important for membranes made of elements heavier than carbon, as they result in more scattering and a higher background.

Choice of substrate is an important consideration for TEM data. Carbon membranes are ubiquitously used in electron microscopy, as they are strong enough to

be handled, conductive, and very thin (<5 nm) membranes can be easily manufactured. While carbon is thin, stable and light, carbon contamination is a major limiting factor in high resolution STEM, and carbon substrates simply cannot be cleaned well enough to undergo 100 or more high resolution STEM images with no carbon contamination. Carbon contamination destroys resolution by creating thick layers of polymerized hydrocarbons in the beam direction [18], creating a large background and too much scattering for good resolution (Fig. 2.1). The cause of this buildup is mobile hydrocarbons on the substrate surface, which move into the beam and become carbonized and no longer mobile. In a conventional TEM imaging configuration, this occurs on the outer edges of the beam, creating "coffee rings" of contamination. However, in STEM, the buildup follows the scanning probe over the area of interest [19]. Contamination buildup rates increase with increased beam intensity [18], and therefore high resolution STEM is very susceptible to contamination. To take as many high resolution STEM projections as are required by electron tomography, the substrate needs to be truly pristine.

Carbon is attacked by plasma cleaners [32], and while this is a good method to remove hydrocarbons, it unfortunately also destroys carbon membranes, so that cleaning a thin carbon support film enough without destroying it entirely is not possible. Even with heat treatment, the hydrocarbons responsible for carbon buildup during imaging adhere too well to the elemental carbon of the grid. Therefore two other materials- silicon and silicon nitride- are used for our measurements. Both of these materials can be plasma cleaned and heat treated well enough that carbon contamination is minimal to nonexistent. Thin Si and SiN membranes are commercially available (TEMwindows.com). Silicon is more conductive than SiN, but SiN is flatter. At 300 keV or 200 keV, we prefer to use SiN with a thin, very clean carbon layer added via a high temperature, ultra-clean process. This carbon coating serves two purposes: 1) it increases the conductivity of the SiN membrane such that charging effects are minimized, even at high angles

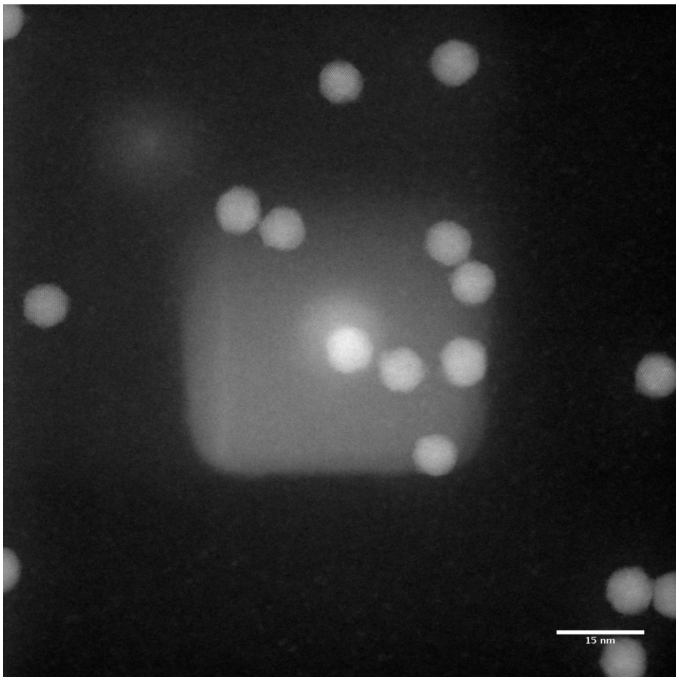

Figure 2.1: Nanoparticles after imaging a contaminated sample. In this zoomed out view, the area over which the STEM probe has rastered is evident as a significant amount of carbon has been deposited in this area. The carbon buildup will reduce both the contrast and resolution of subsequent images.

and 2) when applied after the deposition of the particles, it fixes the particles to the substrate and helps prevent any rotation or shifting on the support membrane, while also helping preserve the surface structure of the particle of interest.

At 80 keV, the beam interacts more strongly with the sample, and charging effects are more pronounced. At this voltage, these effects- apparent sample drift and vibration- are seen even in the carbon-coated SiN samples. Therefore it is necessary to switch to thin Si membranes for 80 keV. These membranes are neither as strong nor as flat as the SiN membranes, but they are conductive enough such that no charging effects, even at high angle with the apparently thicker membrane, are observed.

Especially with the delicate Si grid, care must taken to dropcast a solution of nanoparticles onto the thin membranes. It is advisable to use a nebulizer to mist the solution onto the grid, as the surface tension of a large droplet can break the thin membrane.

After deposition, plasma cleaning can be used to remove any hydrocarbons, however this will eventually destroy any carbon layer that has been added. Lighter gasses (H_2, O_2, air) are more effective at destroying the hydrocarbons than Ar, and are also gentler on the carbon layer. Vacuum baking the sample (200 °C, 1 mTorr) will also produce clean samples while not destroying the conductive carbon layer. We have successfully acquired data on clean samples produced by both vacuum baking and plasma cleaning. Figure 2.2 shows a raw image and summed intensity plot of a particle before and after a data set, showing the minimal contamination buildup. The sample shown in Figure 2.2 is a silicon nitride substrate with an ultraclean carbon layer, and was cleaned by vacuum baking.

In addition to cleaning to sample before loading it into the microscope, all tools and sample holders that come into contact with the sample must be kept clean. The sample and sample handling implements should also be stored in a low humidity environment.

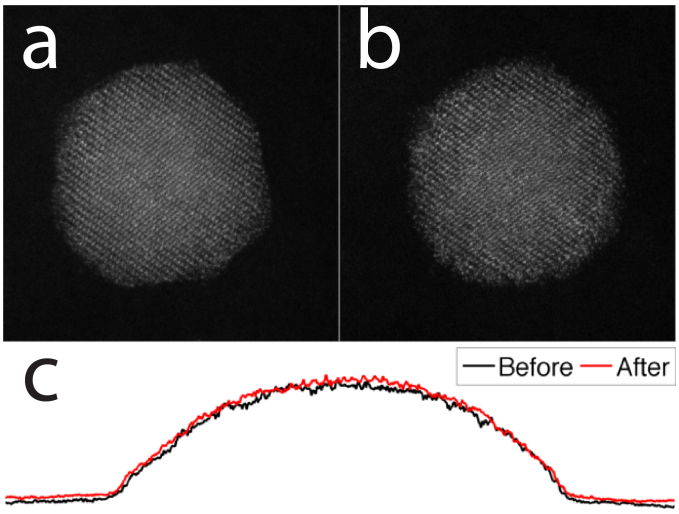

Figure 2.2: A nanoparticle a) before a dataset and b) after the dataset. c) The summed intensities along the horizontal direction for the particle before (black) and after (red) acquisition of a tomography dataset. The additional background from contamination is minimal.

2.2.2 Data acquisition

To apply the EST method to experimental electron tomography data, the only necessary change is to take angles according to the equally sloped scheme, that is

$$\theta = \begin{cases} tan^{-1}(\frac{N+2-2n}{N}) & \text{for } n = 1, ..., N \\ \frac{\pi}{2} - tan^{-1}(\frac{3N+2-2n}{N}) & \text{for } n = N+1, ..., 2N. \end{cases} \tag{2.1}$$

where n is the projection number, and N is the total number of projections. While commercial automated tomography scripts are available, the tracking and focusing is not sufficient to obtain high quality electron tomography data sets. Therefore, to test this method, the data were initially obtained completely by hand. To track a particle during data acquisition, several low magnification images are taken at 0° to help identify the particle as the sample is tilted. Then, the particle is re-centered at low magnification before the magnification is increased for focusing and imaging.

During data acquisition, many steps must be taken to reduce damage to the sample and optimize the quality of the projections in the tilt series. Equally sloped tomography has the advantage that it does not require as many projections for high quality reconstructions as other, simpler reconstruction methods [27]. However, it is still necessary to optimize many aspects of data acquisition to obtain high quality tilt series for atomic resolution reconstructions.

As mentioned above, every object that comes into contact with the sample must be cleaned thoroughly to avoid hydrocarbon contamination during data acquisition. To remove all hydrocarbons from the sample holder (a Fischione model 2020 Advanced Tomography holder) and tweezers, they were cleaned in a plasma cleaner (Gatan Solarus) for 30 minutes, then remained in vacuum for an additional 30 minutes immediately prior to data acquisition.

Obtaining atomic resolution images is dependent on minimizing vibration and drift, both of the sample holder and of the sample itself. Figure 2.3 shows how vibration can destroy resolution in an image. The settling time of the holder will vary, but for the Fischione 2020, it was sufficient to allow 5 minutes after tilting and re-centering the particle before imaging. Additionally, "drum-like" vibrations occur in thin, square, membranes, with the highest amplitude in the center of the membrane [33]. At high angles, this vibration is very apparent in the TEMwindows grids, and therefore only particles within 200 nm of the edge of the thicker frame are selected for a dataset. If the grid has been adequately aligned in the holder (with the long slot perpendicular to the rotation axis), then this will not reduce the tilting range. Furthermore, while some drift and vibration are inevitable, taking many fast images and re-centering and averaging them into a single image later can combat these effects.

During data acquisition, ideal focus and alignment should be attempted. Since radiation damage is a statistical process, focusing in an area that is not the area of interest is ideal [34]. During data acquisition in STEM, the beam can be placed

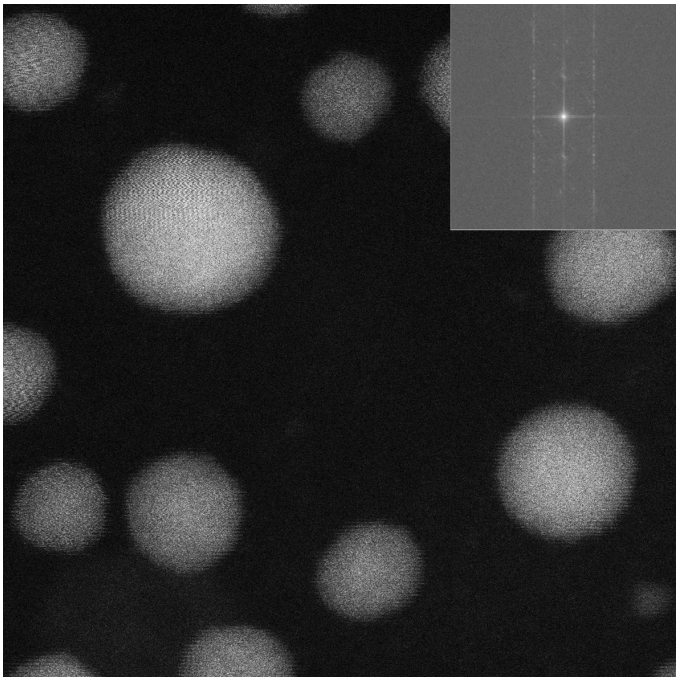

Figure 2.3: Gold nanoparticles imaged with severe vibration adversely affecting the resolution. The vibration is evident in the real space image, as well as streaks in the Fourier transform (inset).

along the tilt axis, above or below the particle, and focusing can be performed using the ronchigram (Fig. 2.4). The ronchigram is a convergent beam electron diffraction pattern of an amorphous section of the sample, and it contains information about the aberrations present in the probe [35]. Defocus, astigmatism, and coma can all be corrected by viewing the ronchigram and making adjustments to the alignments. With practice, this method of focusing is as good or better than focusing using the image and live Fourier transform. Additionally, microscope alignments can drift during long data acquisitions, and in addition to defocus, astigmatism should be checked and corrected at every projection using the ronchigram.

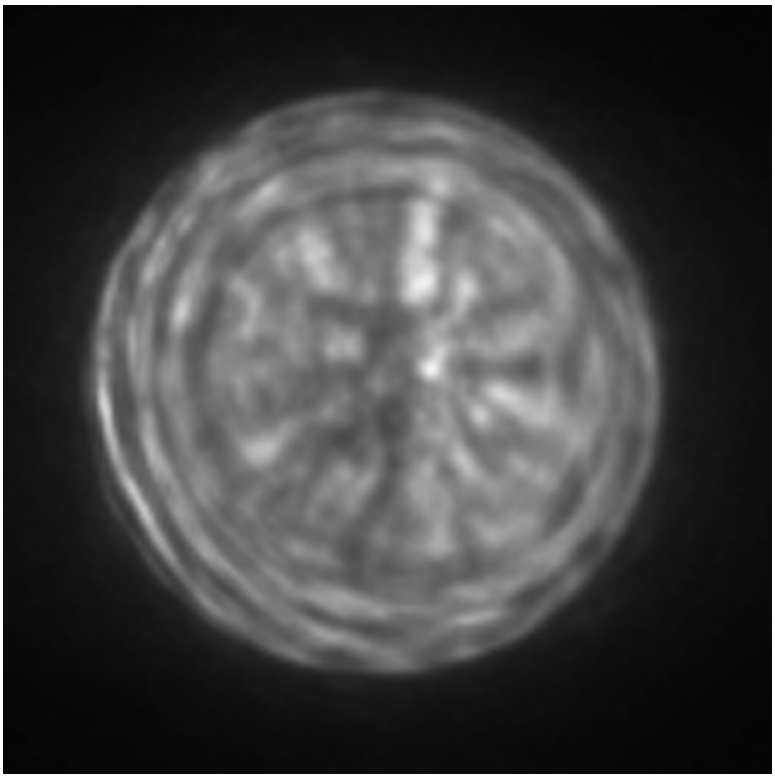

Figure 2.4: A ronchigram. The ronchigram is an image of the direct beam after passing through an amorphous region of the sample in STEM mode. The ronchigram contains information about defocus, astigmatism, coma, and other aberrations present in the microscope.

Additionally, zone axes that introduce nonlinear projections via the channeling effect [36] should be avoided or discarded afterwards. Simple diffraction effects, however, will average out in the reconstruction [37], and while they are a source of error, they do not preclude atomic resolution reconstructions.

An important consideration in high resolution tomography data acquisition is radiation damage. Radiation damage can manifest in a variety of ways, through atom displacement or sputtering, or through changes in the sample induced by electron beam heating [19]. A variety of beam interactions, both elastic and inelastic, can result in damage to the tiny area of interest. Some depend simply on the incident beam energy, while others may depend on current density [19]. For samples that are conductors or semiconductors, knock-on displacement due to elastic scattering is the most likely source of radiation damage [38]. "Knock-on" damage refers to an elastic scattering process wherein enough energy is transferred to an atom by the electron beam that the atom is displaced. Different species of atoms in different bonding configurations will have different knock-on damage thresholds. Therefore, to obtain the most stable set of images, the incident beam energy must be below the knock-on damage threshold. For a single species nanoparticle, the surface knock-on threshold will be lower than that of the bulk atoms [38]. For gold, the surface sputtering energy threshold is 407 keV, and for Pt, it is 560 keV [38]. Therefore imaging at 300 or 200 keV should not induce significant sputtering.

Elastic energy transfer can also induce surface diffusion of atoms, leading to instability. Adding a protective carbon coating, as described in Section 2.2.1 is a way to avoid this. However, the carbon coating must be incredibly clean- any additional hydrocarbons can result in contamination.

Another consideration, however, is that some radiation instability effects are dependent on incident beam current density [19]. Since a small probe is necessary for high resolution imaging, reducing the beam current is the only way to control

this type of damage. Taking a large number of images with lower current and combining them later results in less radiation damage than taking one high current image, even if the delivered dose is identical. In practice, this means that the sample is imaged for a longer time, which again makes it critical that the sample be free of hydrocarbon contamination, as carbon contamination will increase with exposure time [18].

Ultimately, radiation damage will limit the electron dose that can be delivered to the particles. For each new system, the dose should be optimized to ensure particle stability while maximizing the signal-to-noise ratio. The protocol used for nanoparticle data in this thesis is to take a data set with a pixel size of 0.48 Å or smaller, with a dose of around 5×10^5 e/Å^2 delivered via a beam current of 50 pA. If the particle is damaged under these conditions, the number of projections or beam current are reduced. If the particle is not damaged, the number of projections or beam current is increased until the damage threshold is found. Combining the sample production procedures from Section 2.2.1 with the low vibration and drift protocol mentioned above, as well as optimizing the dose for high signal to noise while maintaining particle stability, results in the best data set for atomic resolution reconstruction.

2.3 Summary

This chapter discusses a recipe for data acquisition of high resolution tilt series for atomic resolution tomographic reconstruction. This method has been optimized for 9-10 nm metallic nanoparticles to be reconstructed via equally sloped tomography. This method was developed for an an uncorrected FEI Titan S/TEM, and can now reliably obtain tilt series with sufficient quality for atomic scale resolution tomographic reconstructions. Combined with the equally sloped tomography algorithm, this methodology enables the characterization of many nanoparticle

systems at atomic resolution. The methodology described here will be applied to a gold nanoparticle in Chapter 3, and a platinum nanoparticle in Chapter 4.

CHAPTER 3

2.4Å resolution electron tomography [1]

3.1 Motivation

The need for atomic resolution imaging of materials in three dimensions has driven scientific and technological development for many years, especially with the increase in popularity of nanomaterials as functional materials. In biological applications, electron tomography is a widely used technique to image in three dimensions [13, 39]. In the last decade, electron tomography has been increasingly applied in materials science and nanoscience through the use of STEM [16, 17, 40]. However, while the resolution of aberration corrected TEMs and STEMs is ∼0.5Å in 2D [9], 3D resolution of electron tomography was previously limited to 1 nm^3 [16, 17]. This resolution is not sufficient to image many of the features that determine the

[1] This chapter is a version of is a version of "M.C. Scott, Chien-Chun Chen, Matthew Mecklenburg, Chun Zhu, Rui Xu, Peter Ercius, Ulrich Dahmen, B. C. Regan and Jianwei Miao, "Electron tomography at 2.4-angstrom resolution", *Nature*, 483, p. 444-447 (2012)", with author contributions as follows: J.M. conceived the overall project; M.C.S., M.M., C.Z., B.C.R. and J.M. designed and conducted the experiments; C.Z., R.X., C.C., P.E. and J.M. did multislice STEM calculations; C.C. and J.M. performed the data analysis and image reconstruction; U.D., J. M., C.C., M.C.S., M.M. and B.C.R interpreted the results, J.M., M.C.S., C.C. and M.M. wrote the manuscript. All authors commented on the manuscript.

functionality of nanomaterials- defects, strain, and internal grain boundaries. This chapter focuses on the implementation of high resolution electron tomography on an uncorrected microscope. A series of high-resolution ADF-STEM images were reconstructed via EST, resulting in an atomic scale 3D reconstruction of a gold nanoparticle. With this new technique, previously inaccessible features, such as 3D grains within the particle and even individual atoms in some areas, could be visualized. The 3D surface morphology and internal atomic structure revealed are consistent with an icosahedral multiply-twinned particle.

3.2 2.4 Å resolution electron tomography

3.2.1 Experimental acquisition of tilt series

To apply the EST method to an experimental dataset, ∼10 nm gold nanoparticles from Ted Pella were suspended on 5 nm thick silicon membranes. The silicon membranes can be more easily cleaned than the carbon membranes used ubiquitously in electron microscopy. In addition, silicon is conductive and scatters electrons significantly less than gold. The silicon grid is a typical 3 mm in size, with a thin (5 nm) window with size 100×1500 μm^2 and a 100 μm thick silicon frame, allowing for a tilt range of ±83°. To avoid breaking the membrane, a micromanipulator was used to place a small drop of solution onto the outer frame of the Si grid. After gently moving the drop onto the membrane, it was removed and not allowed to dry and leave excessive gold particles and contaminants. The Si grids were cleaned pre-deposition in a Gatan Solarus plasma cleaner (Model 950) for 20 seconds using a standard H_2/O_2 recipe. To further ensure removal of contaminant sources, the sample holder (Fischione Model 2020) was plasma cleaned for an hour prior to data acquisition using the same recipe.

The sample was imaged at 300 keV in an uncorrected FEI Titan microscope

at UCLA's California NanoSystems Institute. To reduce vibration and drift, the sample holder was allowed to settle for one hour after insertion, and for several minutes after moving to each new projectional angle. The tilt series was acquired by manually changing the acquisition angle according to the EST scheme. Based on the microscope's C_3 value of 1.2 mm, the measured convergence angle of 7.98 mrad and Equation 1.5, the resolution of the microscope in this configuration is 1.36 Å at a 300 keV operating voltage. By using a low-dose focusing scheme that involves viewing the direct beam placed on the membrane near the particles of interest, then acquiring an image for the tomography data set, a tilt series of 69 projections was acquired over a range of $\pm 72^\circ$ (Figures 3.1 and 3.2). Figure 3.2 confirms that a each projectional image's resolution was 2.4 Å or higher. The incident beam current was 70 pA, the dwell time per pixel was 45 μs, with a pixel size of 0.42 Å. The total dose (including images that were not used in the tomographic reconstruction) was 7.6×10^6 e/Å^2. To ensure that the low dose scheme did not cause significant changes in the particle's shape or structure, three 0° projections were taken before, during and after data acquisition (Figure 3.3).

3.2.2 Reconstruction via equally sloped tomography

To obtain the internal structure of the nanoparticle, the ADF-STEM tilt series was reconstructed via EST as described in Section 1.2.3. The 69 projections first had a linear background subtraction applied, and signal to noise was improved by performing 2×2 binning. To align the tilt series along the Y-axis, the projections were first projected onto the Y-axis and a set of 1D curves was generated. Using the 1D curve at 0° as a reference, the remaining curves are aligned to the reference. To align the projections along the X-axis, the CM alignment was used to align all the projections to a common axis. For this reconstruction, both positivity and a support were used as real space constraints. A very loose support was estimated, and 500 iterations of the EST algorithm were calculated. Next, a tighter support

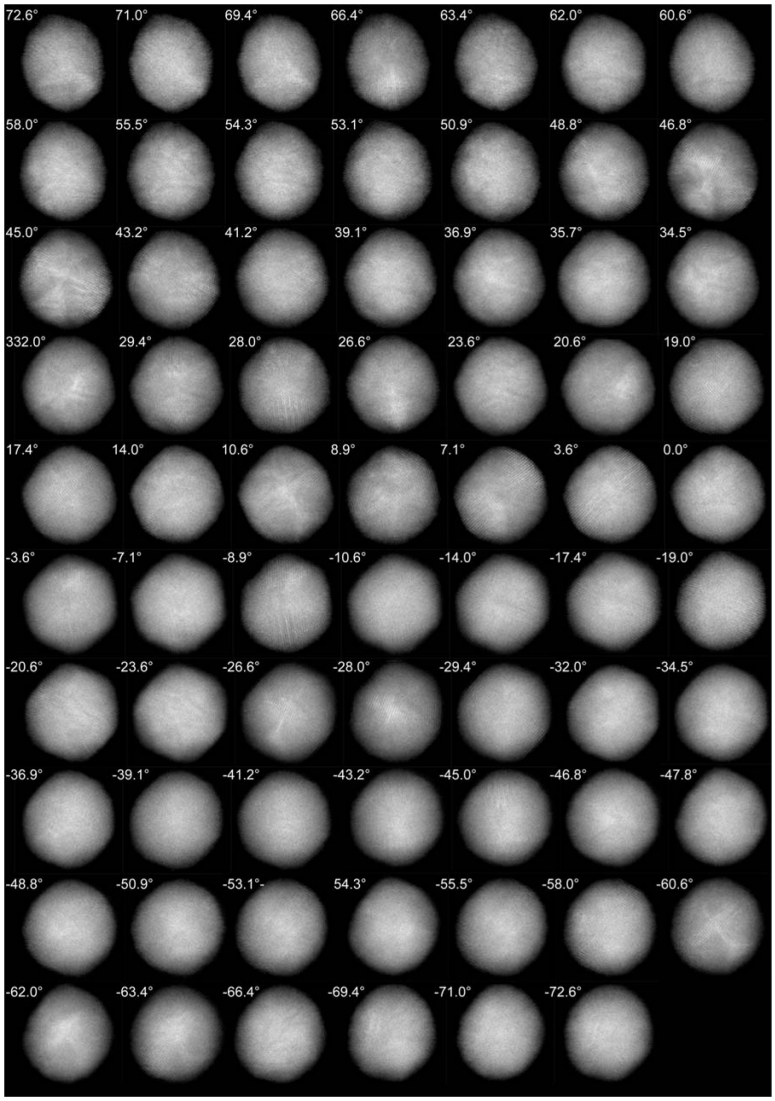

Figure 3.1: 69 ADF-STEM projections of a tomographic tilt series of a ∼10 nm gold nanoparticle, acquired over a range of ±72°.

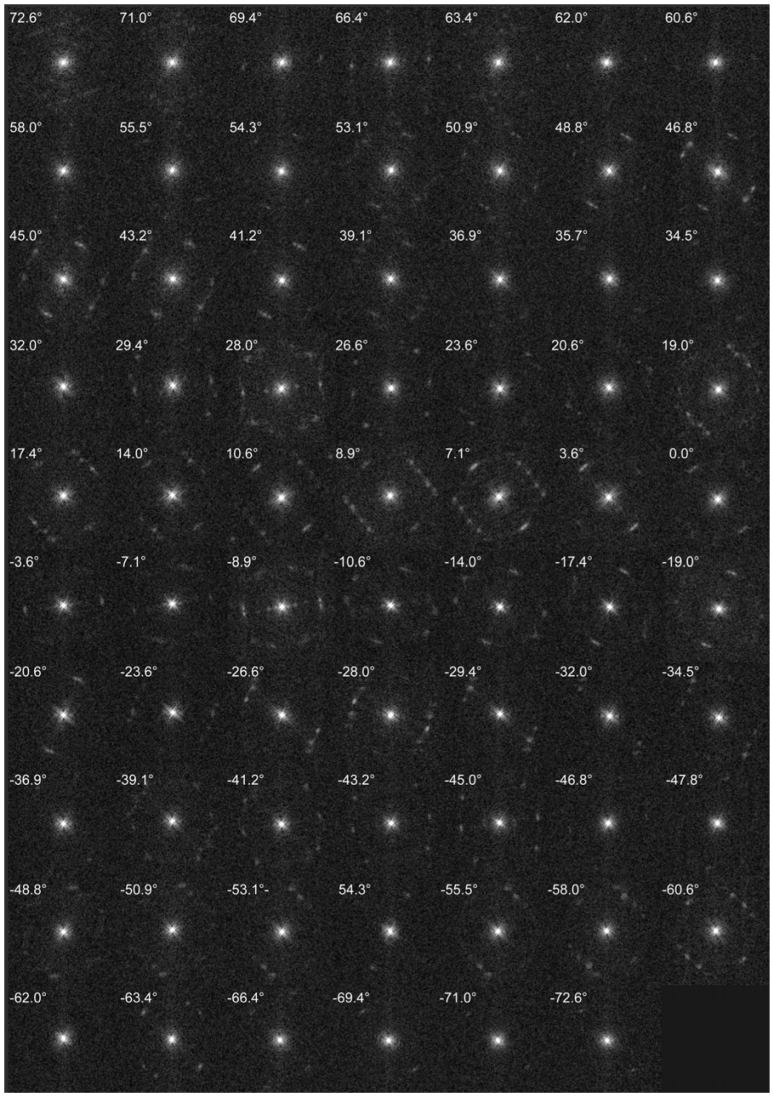

Figure 3.2: Fourier transforms of all 69 ADF-STEM projections of a topographic tilt series of a ∼10 nm gold nanoparticle, acquired over a range of ±72°. 2.4 Å resolution or higher is achieved in all projections.

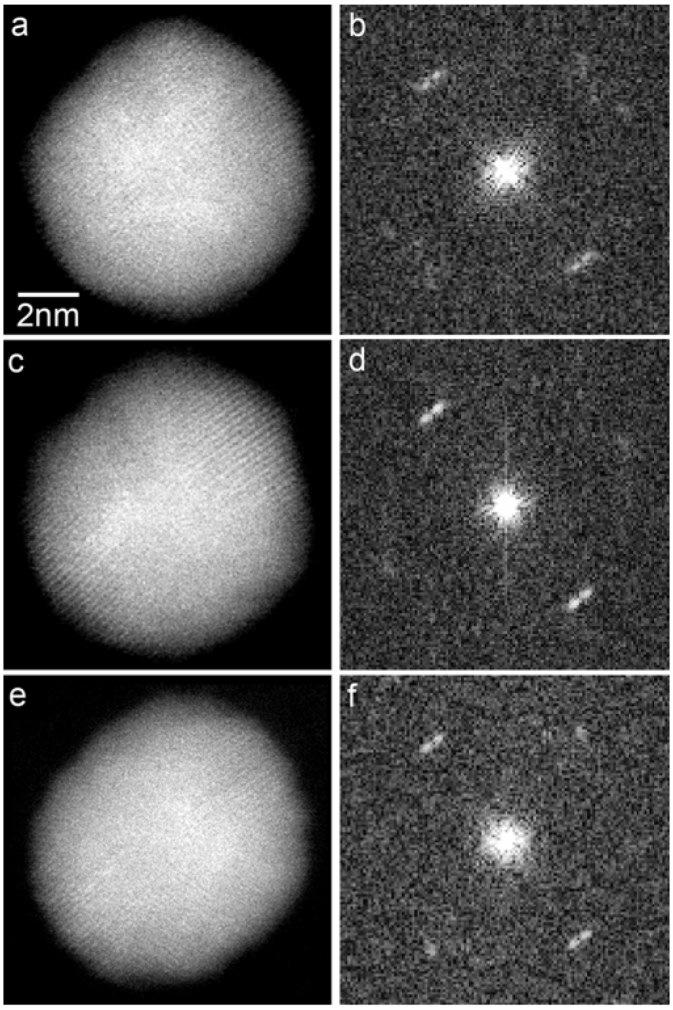

Figure 3.3: 0° projectional images acquired before (a) during (c) and after (e) the tomographic tilt series. b, d and f show the corresponding FFTs. Although some minor shape changes occurred, the crystal lattices and overall shape of the particle remained reasonably consistent throughout the experiment.

was estimated based on the reconstructed object. After 500 more iterations, the algorithm was terminated.

After reconstruction, the calculated 3D model was projected back to the original 69 angles. An error metric, R_{real} was calculated for each projection:

$$R_{real} = \frac{\sum_i ||f_c^i(x,y)| - |f_m^i(x,y)|}{\sum_i |f_m^i(x,y)||} \tag{3.1}$$

where $f_c^i(x,y)$ and $f_m^i(x,y)$ are the calculated and measured projections, respectively, at angle i. The average R_{real} for all 69 projections was 6.7%. Figure 3.4 shows a projection from the reconstruction compared to the same projection from the experimental dataset, indicating strong agreement between the two.

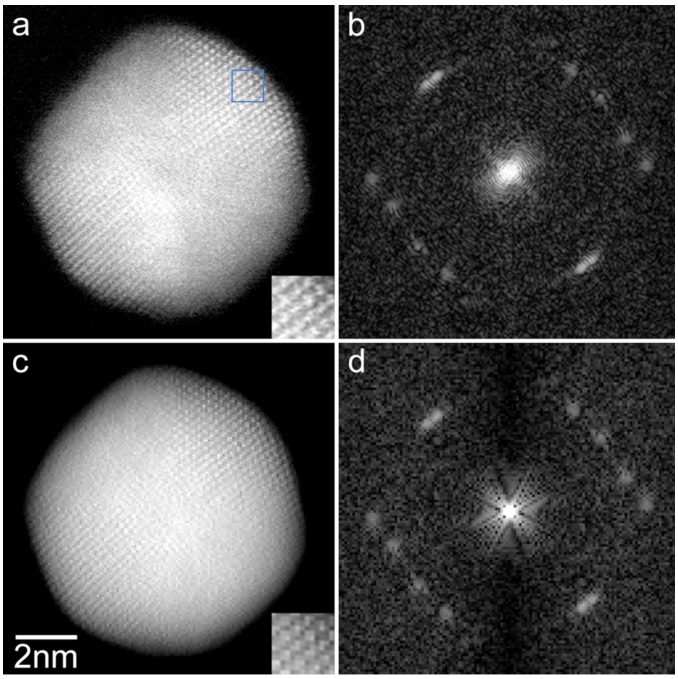

Figure 3.4: Representative measured **a** and calculated **c** projections and their Fourier transforms **b**,**d** at 7.1°, where insets show the projected atomic positions inside the blue square. The overall shape of the nanoparticle and the location of the Bragg peaks agree very well, indicating a good quality 3D reconstruction.

3.3 Results

To determine the resolution of the final reconstruction, interior slices of the reconstruction were examined. Three 3.36 Å slices through the reconstructed gold nanoparticle are shown in Figure 3.5. Also shown are corresponding Fourier transforms of the slices, indicating that 2.4 Å lattice features were resolved in all three (X, Y, Z) directions, even along the missing wedge direction. Single atoms are visible in both internal slices, but atomic structure disappears in some areas in Figure 3.5a and c, as the distance between adjacent lattice planes in these areas is below the resolution of 2.4 Å. To confirm this, two perpendicular slices (3.36 Å thick as well) with the particle rotated about the Y-axis by $\sim 60^{\circ}$ are shown in 3.5c. Figure 3.6 shows the two rotated slices and their Fourier transforms, where the atomic lattice structure is visible in the top and bottom areas of the particle, but is not present in Figure 3.5c. The apparent flattening of the particle along the beam axis was also observed in the 3D reconstructions of other gold nanoparticles, and was likely caused by interactions between the nanoparticle and the silicon substrate.

To visualize the internal structure and the morphology of the gold nanoparticle, 3D volume and iso-surface renderings of the reconstruction were generated, in which both surface and internal lattice structures are visible. Fig. 3.7a and b show volume renderings of the nanoparticle and their Fourier transforms (insets) at the 2- and 3-fold symmetry orientations. The corresponding iso-surface renderings at the same orientations are shown in Figs. 3.7c and d. The overall 3D shape and facets of the nanoparticle are consistent with an icosahedron (insets in Figs. 3.7c and d). To identify internal 3D grains, a 3D Fourier transform was applied to the reconstruction. By identifying the Bragg peaks of each major grain and applying the 3D inverse Fourier transform to the selected Bragg peaks, four major 3D grains inside the gold nanoparticle were identified. Fig. 3.8 shows a volume

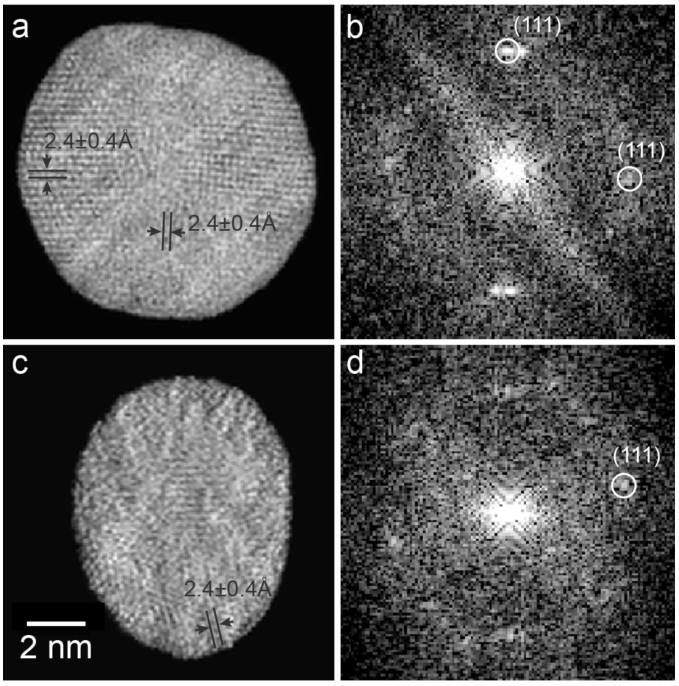

Figure 3.5: 3D resolution estimation of the reconstruction and single atom visualization inside the nanoparticle. **a** and **b**, A 3.36 Å thick central slice in the XY plane and its Fourier transform, indicating 2.4 Å resolution was achieved along the X- and Y-axes. **c** and **d**, A 3.36 Å thick slice in the ZY plane and its Fourier transform where the horizontal axis is along the Z-axis (beam direction). The resolution in the Z-axis was estimated to be 2.4 Å. Single atoms are visible in both slices.

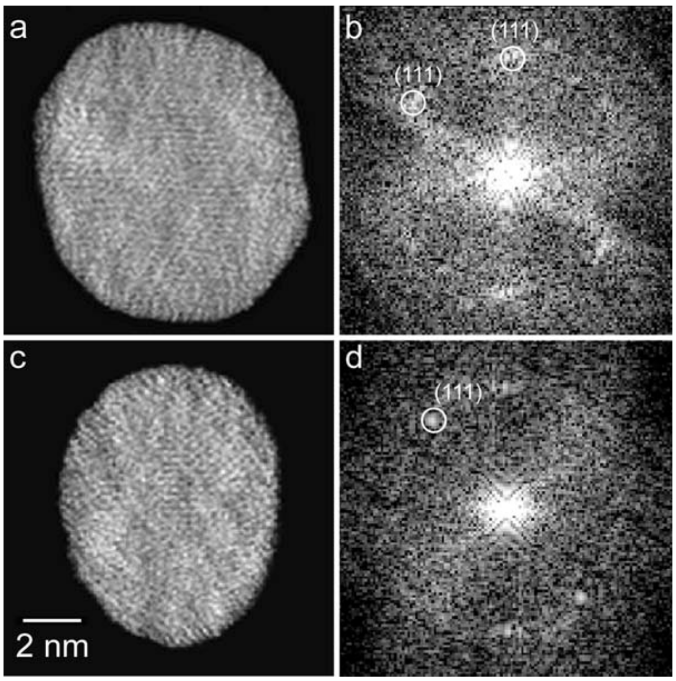

Figure 3.6: Two counterpart slices (**a**,**c**) of Figs. 2**a** and **c** and their Fourier transforms (**b**,**d**). The two 3.36 Å thick slices were obtained from the particle after it was rotated about the Y-axis in Fig. 3.5c by 60°. The atomic lattice structure is visible in the top and bottom areas in **a** and the top-right area in **c**, but is not present in Fig. 3.5**c**.

rendering of the four 3D grains at atomic scale resolution, in which grains 1, 2 and grains 3, 4 are related by mirror-reflection across the horizontal interfaces marked by dotted lines. The angle enclosed by close-packed planes across these interfaces was measured to be 69.9°±0.8° between grains 1 and 2, and 71.3°±0.8° between grains 3 and 4, both of which are consistent with the angle for an fcc twin boundary (70.53°). Applying the same method to weaker Bragg peaks identified 3D grains in the top and bottom parts of the particle (Figure 3.9). The surface morphology (facets) and the internal atomic structures (grains) suggest that this is an icosahedral multiply-twinned particle, typically found for nano-gold in the size range above 10 nm [41].

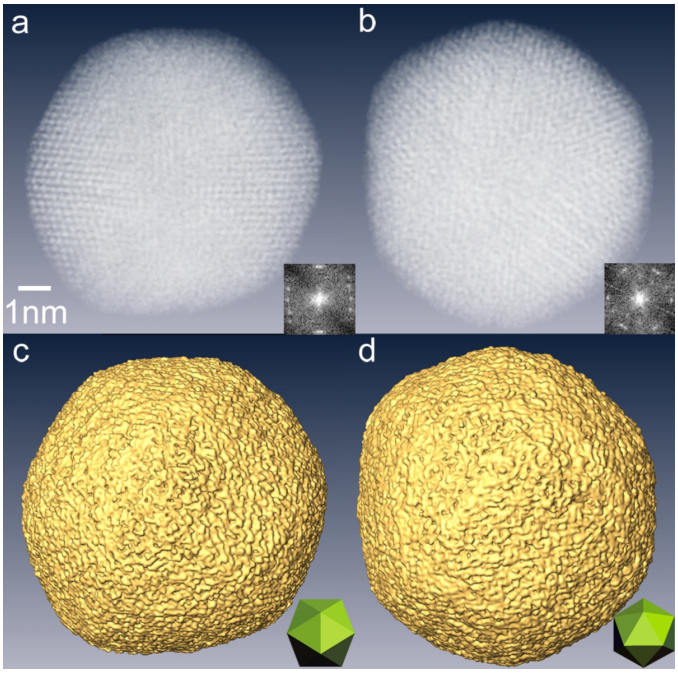

Figure 3.7: 3D structure of the reconstructed gold nanoparticle. a and b, 3D volume renderings of the nanoparticle and their Fourier transforms (insets) at the 2- and 3-fold symmetry orientations. c and d, Iso-surface renderings of the nanoparticle at the 2- and 3-fold symmetry orientations, compared to a model icosahedron at the same orientation (insets).

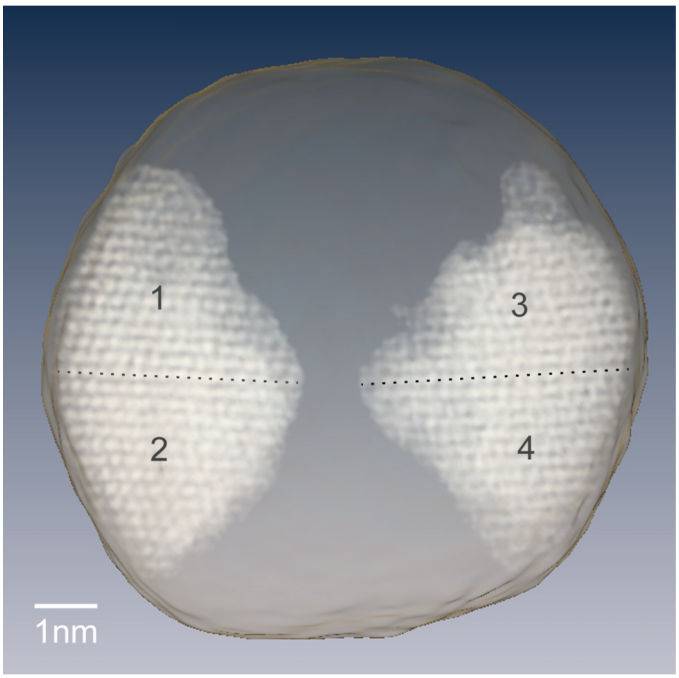

Figure 3.8: Identification of four major 3D grains inside the gold nanoparticle at atomic scale resolution. Grains 1, 2 and grains 3, 4 are related by mirror-reflection across the horizontal interfaces marked by dotted lines. The angle enclosed by close-packed planes across these interfaces was measured to be 69.9°±0.8° between grains 1 and 2, and 71.3°±0.8° between grains 3 and 4, both of which are consistent with the angle for an fcc twin boundary (70.53°)

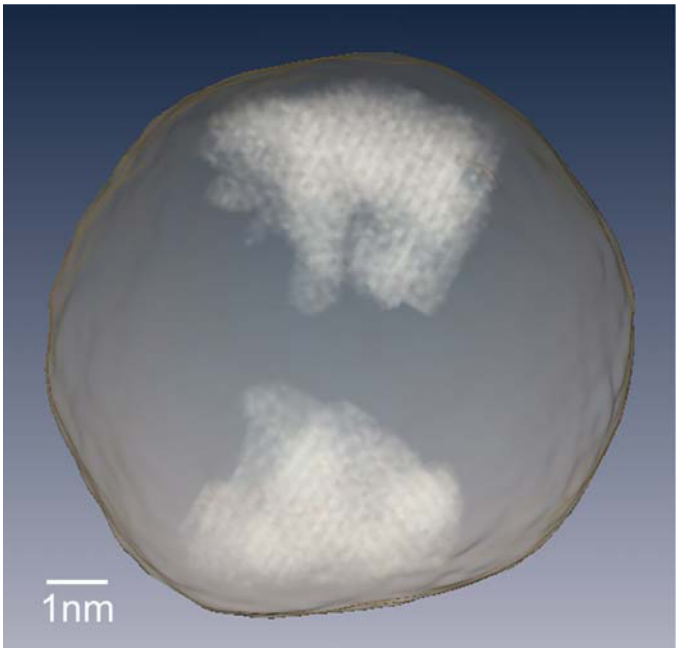

Figure 3.9: 3D grains were identified at the atomic scale resolution in the top and bottom parts of the particle that is oriented at the 3-fold symmetry direction.

3.4 Summary

The demonstration of 2.4 Å resolution tomography of a gold nanoparticle represents a milestone in electron tomography. Applying the CM alignment technique and EST reconstruction method to a tilt series of high resolution ADF-STEM images has revealed 3D structure of a ∼10 nm gold nanoparticle at 2.4 Å resolution, even though the tilt series was limited to 69 projections with a missing wedge. Single atoms inside the nanoparticle are visible and several internal grains were identified in three dimensions. This work represents the first 3D structural determination of a single metallic nanoparticle at atomic scale resolution without initial assumptions about the sample structure, and is a demonstration of a new technique for the high-resolution characterization of nanomaterials in three dimensions. Compared to atom-probe tomography [42], this non-destructive technique can not only handle isolated nanomaterials, but also provide 3D local structure

of complex materials at atomic scale resolution. This proof-of-principle uses a gold nanoparticle as the sample, but the methodology described in this chapter is general, and can be applied to determine the 3D atomic arrangement of a wide range of materials such as crystalline, polycrystalline, and disordered structures.

CHAPTER 4

Three-dimensional imaging of dislocations in nanoparticles at atomic resolution [1]

4.1 Motivation

Dislocations and their interactions strongly influence many of the properties of materials, ranging from the strength of metals and alloys to the efficiency of light-emitting diodes and laser diodes [43, 44]. Presently there are several experimental methods to visualize dislocations. Transmission electron microscopy (TEM) has long been used to image dislocations in materials [45], and high resolution electron microscopy can reveal dislocation core structures with increasing detail, particularly in annular dark field (ADF) where image interpretation is simpler [46]. A

[1] This chapter is a version of is a version of "C.-C. Chen, C. Zhu, E. R. White, C.-Y. Chiu, M.C. Scott, B. C. Regan, L. D. Marks, Y. Huang and J. Miao, "Three-dimensional imaging of dislocations in a nanoparticle at atomic resolution", *Nature*, 496, p. 74-77 (2013)", with author contributions as follows: J.M. directed the project; C.Y.C., C.Z., Y.H. and M.C.S. synthesized and prepared the samples; C.Z., E.R.W., B.C.R. and J.M. designed and conducted the experiments; C.C. and J.M. performed the CM alignment and EST reconstruction; J.M., C.C., C.Z. and L.D.M. analyzed and interpreted the results, J.M., C.C. and C.Z. wrote the manuscript. All authors commented on the manuscript.

TEM image, however, represents a 2D projection of a 3D object, although stereo TEM can provide limited information about 3D dislocations [47]. Techniques such as X-ray topography and atom probe tomography offer 3D information with limited resolution[48, 49]. Weak beam dark field and conventional STEM tomography also give 3D reconstructions with limited resolution. To understand defects in materials, 3D atomic resolution tomography is needed. Here, the methodology described in Chapter 2 and first implemented in Chapter 3 has been fine tuned to observe dislocations in a 9 nm Pt nanoparticle.

4.2 Atomic resolution electron tomography of a 9 nm Pt nanoparticle

4.2.1 Experimental data acquisition and reconstruction via EST

Pt nanoparticles were synthesized with selectively exposed crystal surfaces and particular shapes using facet-specific peptide sequences [50]. The Pt nanoparticles were then deposited on a 5-nm-thick silicon nitride membrane. The membrane, with a size of 100 μm $\times$ 1500 μm, is supported on a 100 μm thick silicon frame (TEMwindows.com). To dissipate charge efficiently and to reduce the knock on damage, a premium high-temperature ultrathin carbon coating (TEMwindows.com) was applied to the nanoparticles based on the following procedure. The silicon nitride membrane grid was first placed into a vacuum chamber with the temperature ramping up from 300 °C to 700 °C at a rate of 10 °C/s. The carbon was coated during a 5 minute soak at 700 °C. The chamber then naturally cooled to 450 °C over the next 5 minutes before the grid being removed. The silicon nitride membrane grid was finally loaded on a tomographic sample holder

(Fischione Model 2020) for data acquisition.

STEM images of the Pt nanoparticles were acquired on a FEI Titan 80-300 microscope (energy, 200 keV; spherical aberration, 1.2 mm; illumination semi-angle, 10.7 mrad). The 100 pA electron beam was focused to a probe with a 50 μm probe-forming aperture (C2) and rastered over the sample. The scattered electrons were captured by a Fischione Model 3000 HAADF detector with semi-angles between 35.2 and 212.3 mrad from the optical axis. The use of HAADF angles was to reduce the nonlinear intensities and diffraction contrast in the images. The maximum tilt angles were limited by the holder to $\pm 75^{\circ}$. To reduce vibration and drift during data acquisition, the sample holder was allowed to settle for one hour after insertion into the microscope and also for several minutes after moving to each new angle. Tilt series were manually acquired by changing the angle with equal slope increments [20, 25, 27, 28, 30]. When focusing an image, a nearby nanoparticle was first viewed (not the particle of interest), thus reducing the unnecessary radiation dose to the particle under study, and fine focusing was also performed by viewing the ronchigram [30]. Using this low exposure acquisition scheme, a tomographic tilt series of 104 projections with equal sloped increments and a tilt range of $\pm 72.6^{\circ}$ was acquired from a Pt nanoparticle. The probe current was $\sim$100 pA with a dwell time of 48 μs per pixel, and the magnification of each projection was 3.6×10^{6}. The total electron dose of the tilt series was estimated to be $\sim 2.5\times10^{7}$ e/Å^{2}. Since the pixel size in STEM mode may vary, a calibration image of an oriented single crystal Au foil (Ted Pella) was taken in STEM mode under the same conditions, and the STEM pixel size was characterized to be 0.35 Å. To enhance the signal to noise ratio in the projections of the tilt series, 1.5×1.5 pixel binning was performed for each projection. The pixel size of the binned projections is 0.53 Å. Figures 4.1 and 4.2 show the tilt series of 104 projections with equal sloped increments and a tilt range of $\pm 72.6^{\circ}$. To monitor the radiation damage effect on the Pt nanoparticle, three 0° projections were

measured during the acquisition of the tilt series (Fig. 4.3). The consistency of these projections indicates that the crystal lattice structure of the nanoparticle was stable throughout the experiment.

After background subtraction and CM alignment, the tilt series was reconstructed by the EST method [20, 25, 27, 28, 30], as described in Section 1.2.3. Figures. 4.4a and c show the 3D Fourier transform of the reconstruction and a 2.6 Å thick central slice in the XY plane, where the electron beam is along the Z-axis.

Due to dynamical scattering effects [36], the missing wedge problem [30, 46, 51] and Poisson noise in the tilt series, noise exists among the Bragg peaks in the 3D Fourier transform of the raw EST reconstruction (Figure 4.4a). As a result, while the crystal lattice structure and some individual atoms are visible, 3D dislocations within the nanoparticle cannot be identified at atomic resolution in the raw reconstruction (Figure 4.4c). To enhance the signal to noise ratio in the reconstruction, the reconstruction was further processed using a Bragg filter that selected {111} and {200} Bragg peaks. This strong filtering method was compared to a Weiner filter to confirm that no artifacts were introduced (Fig. 4.4).

4.3 Observation of edge dislocations, screw dislocations and stacking faults

After enhancing the signal to noise via Bragg filtering, 3D dislocations and defects were visible in the reconstruction of the Pt nanoparticle obtained from the experimental tilt series. Fig. 4.5 shows grain boundary comparisons between a 2D projection and 2.6Å thick internal slices of the particle. The experimentally measured projection in the XY plane suggests that this is a decahedral multiply-

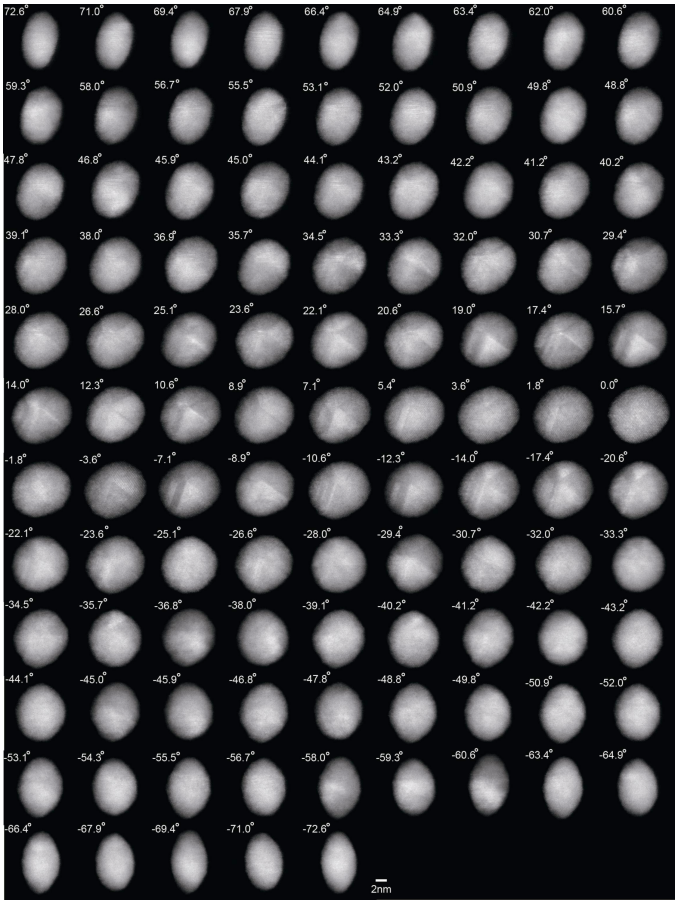

Figure 4.1: Experimental tilt series of 104 projections with a tilt range of $\pm 72.6^{\circ}$ and equal slope increments, acquired from a Pt nanoparticle using HAADF-STEM (energy, 200 keV; spherical aberration, 1.2 mm; illumination semi-angle: 10.7 mrad; detector inner and outer angles: 35.2 and 212.3 mrad; pixel size: 0.35 Å). The total electron dose of the tilt series was estimated to be $\sim 2.5 \times 10^7$ e/Å^2.

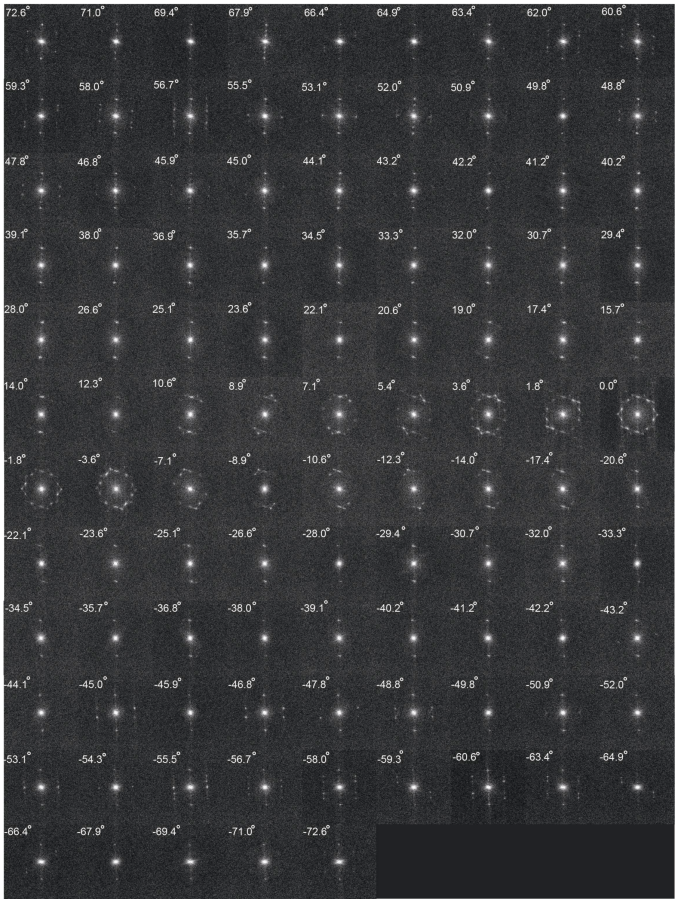

Figure 4.2: Fourier transforms of the 104 projections (Supplementary Fig. 1), in which Bragg peaks are visible in most projections.

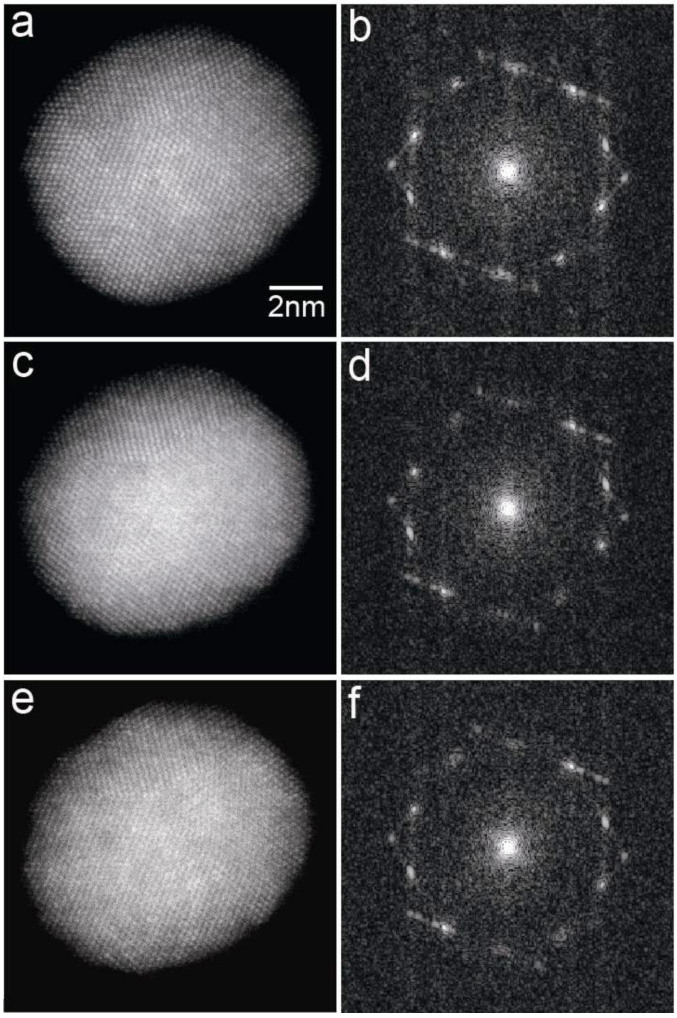

Figure 4.3: Three 0° projections (a,c,e) and their Fourier transforms (b,d,f) measured during the acquisition of the tilt series to monitor the radiation damage effects. The crystal lattice structure of the nanoparticle was consistent throughout the experiment.

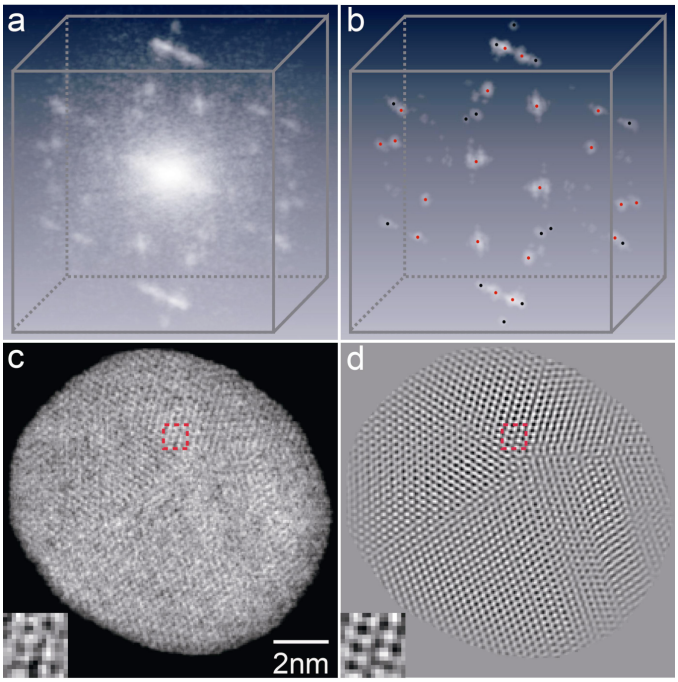

Figure 4.4: 3D reconstruction of a polycrystalline Pt nanoparticle before and after applying a 3D Bragg peak filter. a, 3D Fourier transform of the raw reconstruction of the nanoparticle. b, 3D Fourier transform of the reconstruction after 3D Bragg peak filtering where the {111} and {200} Bragg peaks are labelled with red and black dots, respectively. c, A 2.6 Å thick central slice in the XY plane of the raw reconstruction, where the Z-axis is along the beam direction d, The same slice of the 3D structure after applying a 3D Bragg peak filter, in which nearly all the atoms (in white) are visible. The clear boundary of the nanoparticle is due to the multiplication of the 3D structure with its 3D shape obtained from the EST reconstruction. The insets show a zoomed region of the atomic positions before and after applying a 3D Bragg peak filter.

twinned nanoparticle[52] and coherent twin grain boundaries (CTBs) are flat (Fig. 4.5a). However, a 2.6 Å thick internal slice in the XY plane and a zoomed view indicate the formation of atomic size steps along CTBs (Figs. 4.5b and 4.5c) that are not visible in the projectional image (Fig. 4.5a). Figs. 4.5d and e show zoomed views of the CTBs of a 2.6 Å thick slice above and below the slice of Fig. 4.5b, revealing that the atomic size steps vary in consecutive atomic layers. Although the formation of steps and jogs along CTBs in Cu has been observed in two dimensions with TEM[53], here we observed the formation of atomic size steps along CTBs in three dimensions. Fig. 4.5f shows a zoomed view of a stacking fault in the 2.6 Å thick internal slice ending at a grain boundary, which is in good agreement with the classical model for an extrinsic stacking fault[43] (inset in Figure 4.5f).

Besides CTBs and stacking faults, we also visualized the 3D core structure of edge and screw dislocations at atomic resolution in the Pt nanoparticle. Figs. 4.6a and b show a 7. 9Å thick internal slice of the nanoparticle and a zoomed view of an edge dislocation, where red dots label the position of atoms. By computationally sectioning through the 7.9 Å thick slice, we obtained three consecutive atomic layers each with 2.6 Å thick (Figs. 4.6c-e). The three consecutive atomic layers indicate the dislocation line is in the $[10\bar{1}]$ direction, and the Burgers vector of the edge dislocation was determined to be $\frac{1}{2}[101]$ (Figure 4.6b). To visualize a screw dislocation, a 5.3 Å thick slice (two atomic layers) in the $[\bar{1}11]$ plane was selected and then tilted to the [011] direction (Fig. 4.7a). Fig. 4.7b shows a zoomed view of the slice where the zigzag pattern, a characteristic feature of a screw dislocation, is visible. To visualize the screw dislocation, we display surface renderings of the zoomed region (Fig. 4.7c) where the atoms in green are on the top layer and those in red in the bottom layer. The zigzag pattern is more clearly visualized in the surface renderings, in which the green line connects the atoms on the top layer and the red line for the atoms in the bottom layer. The Burgers

vector of the screw dislocation was determined to be $\frac{1}{2}[01\bar{1}]$, and the width of the screw dislocation was estimated to be $\sim$8.9 Å , which is consistent with the high resolution TEM results for Au and Ir [54].

4.4 Summary

In conclusion, by developing a 3D Bragg peak filtering method and applying it to an EST reconstruction, we determined the 3D structure of a polycrystalline Pt nanoparticle at atomic resolution. The data for this experiment were obtained in a manner similar to those in Chapter 3, although a lower microscope accelerating voltage was used and more projections were taken. Additionally, a larger inner detector angle was used to improve the linearity of the projections. By improving the quality of the data and enhancing the signal to noise in the reconstruction using Bragg filtering, internal defects and dislocations were resolved inside the particle in atomic resolution 3D. We observed the formation of atomic size steps along CTBs in three dimensions that are not visible in the projectional image of the Pt nanoparticle. We also imaged the 3D core structure of edge and screw dislocations in the nanoparticle at atomic resolution. The significance of this work is twofold. First, it advances our fundamental understanding of dislocations in materials. Second, EST based ADF-STEM tomography in combination with 3D Bragg peak filtering represents a general method for determining the 3D atomic structure of polycrystalline materials.

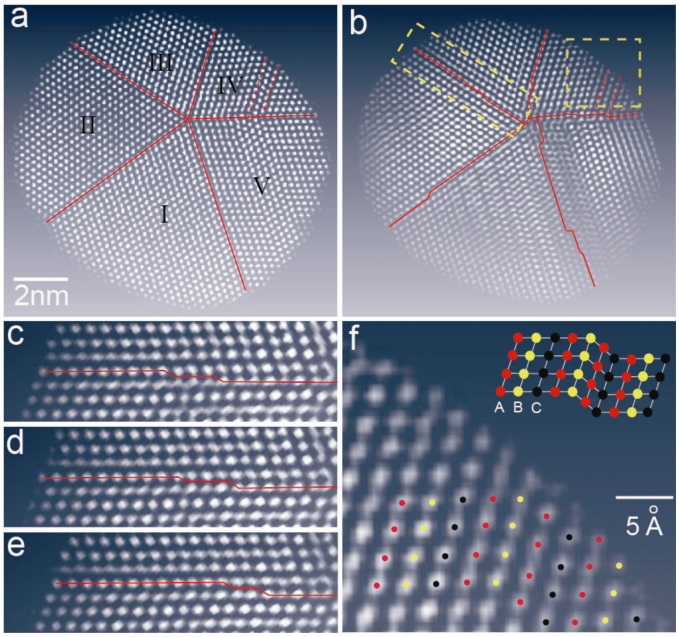

Figure 4.5: Grain boundary comparisons between a 2D experimental projection and several 2.6 Å thick internal slices of the reconstructed Pt nanoparticle. a, Experimental projection in the XY plane after 2D Bragg peak filtering, suggesting this is a decahedral multiply-twinned nanoparticle and the grain boundaries are flat. b, A 2.6 Å thick internal slice indicating the formation of atomic size steps in CTBs. c, Zoomed view of a CTB in (b). d, and e, a 2.6 Å thick slice above and below the slice of (c), revealing that the atomic size steps formed along CTBs vary in consecutive atomic layers. f, Zoomed view of a stacking fault in the 2.6 Å thick internal slice, which is in good agreement with the classical model for an extrinsic stacking fault (inset). These images as well as those in Figs. 3 and 4 are displayed with Amira.

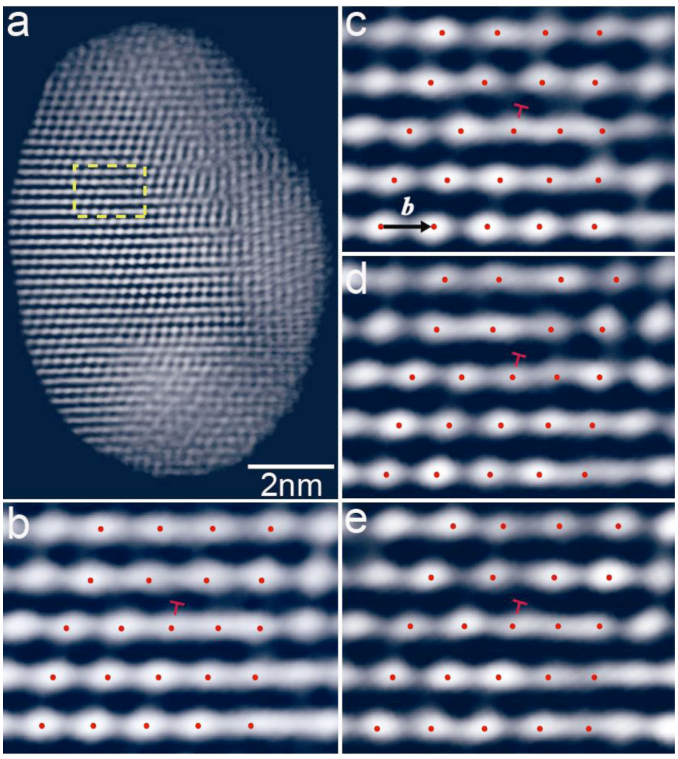

Figure 4.6: Observation of the 3D core structure of an edge dislocation at atomic resolution. a, A 7.9 Å thick internal slice of the nanoparticle. b, A zoomed view of an edge dislocation in (a) where red dots represent the position of the atoms. c, d and e, 2.6 Å atomic layers sectioning through the slice of (b). The three consecutive atomic layers indicate the dislocation line is in the $[10\bar{1}]$ direction. The Burgers vector of the edge dislocation was determined to be $\frac{1}{2}[101]$.

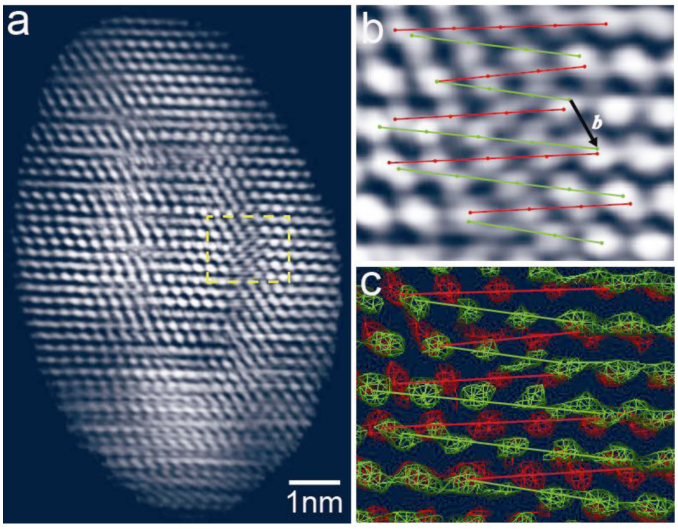

Figure 4.7: Observation of the 3D core structure of a screw dislocation at atomic resolution. a, Volume renderings of a 5.3 Å thick slice (two atomic layers) in the $(\bar{1}11)$ plane, tilted to the [011] direction in order to visualize the zigzag pattern that is characteristic of a screw dislocation. b, Zoomed view of a screw dislocation showing the zigzag pattern. c, Surface renderings of the screw dislocation where the atoms in green are on the top layer and those in red in the bottom layer. The zigzag pattern is more clearly visualized, the Burgers vector of the screw dislocation was determined to be $[01\bar{1}]$ and the width of the screw dislocation was estimated to be ∼8.9 Å.

CHAPTER 5

Atomic resolution tomography on an aberration corrected electron microscope

5.1 Motivation

To identify all of the atoms within a sample, identifying their coordinates in 3D space, it was necessary to develop tomography on an aberration corrected microscope. While the Bragg filtering described in Chapter 4 can be used to drastically reduce noise in a 3D reconstruction, this method cannot be used to identify point defects. Therefore, improving the resolution and signal-to-noise ratio in each projection is needed to determine all of the atomic positions within a sample precisely. The TEAM I microscope at the National Center for Electron Microscopy at Lawrence Berkeley National Labs was used for these experiments.

Many of the protocols used to collect data on an uncorrected microscope, such as choice of substrate and removal of hydrocarbon contamination, will be

the same as described in Chapter 2, and therefore are not repeated here. This chapter focuses on overcoming new challenges that arise with using an aberration corrected microscope to acquire tomographic data, as well as improvement in some areas beyond what is necessary for ~ 2.4Å tomography.

5.1.1 Sample geometry and sample stability

The TEAM I is aberration corrected, with a STEM probe size of 50 pm at 300 keV. The small probe size is achieved with a larger convergence angle, either 17 mrad for a ∼1 Å probe or 30 mrad for a ∼0.5 Å probe. This increase in convergence angle places a strict limit on the thickness of the sample, since the depth of field is only $\sim$ 10nm in the 30 mrad case.

Reducing the probe size also effectively increases the current density in the probe. Due to this, radiation damage must be carefully monitored throughout the dataset, as increased current density can increase some radiation damage effects [19] . Additionally, while some changes to the surface and minor shape changes were permissible for the input data in Chapters 3 and 4, true atomic resolution tomography requires near perfect stability. For metals, even the 300 keV beam is typically below the knock-on damage threshold [38], so reducing the current density by reducing the beam current and taking many images per angle is an effective way to increase stability. While in Chapter 2 this technique is employed primarily to combat sample vibration and stage drift, here it is necessary for particle stability. Figure 5.1 shows before and after images of two bimetallic FePt particles. While the dose for each particle is similar (in fact the total dose for particle 2 is higher than that of particle 1), particle 1's dose was delivered by a higher current density probe. Particle 1 shows signs of instability while particle 2 is stable. Particle 1's dose was delivered via a 63 pA probe with dose/area in each image of 6.6×10^3 $e/\text{Å}^2$, but with a total dose of 1.5×10^6 $e/\text{Å}^2$, while particle 2's

dose was delivered via a 52 pA probe with dose/area in each image of 4.1×10^3 $e/\text{Å}^2$, but with a total dose of 1.75×10^6 $e/\text{Å}^2$. 234 images were taken in particle 1's dataset, while 428 were taken in particle 2's. The probe current difference here is small, only 11 pA higher for particle 1, but the difference in stability is dramatic (Fig. 5.1).

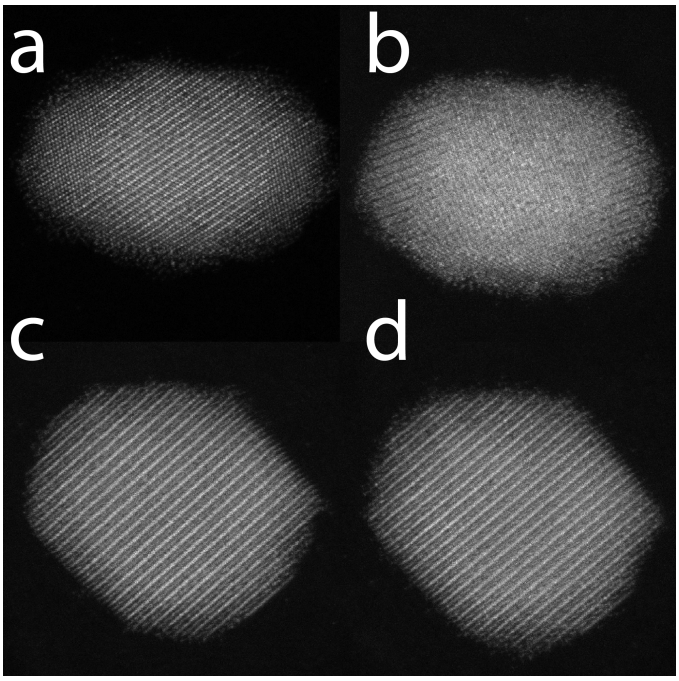

Figure 5.1: Two particles before and after tomography datasets. a) Particle 1, before the dataset b) particle 1 after the dataset. Particle 1's dose was delivered via a 63 pA probe with dose/area in each image of 46.6×10^3 $e/\text{Å}^2$, but with a total dose of 1.5×10^6 $e/\text{Å}^2$. c)Particle 2 before the dataset and d) after the dataset. Particle 2's dose was delivered via a 52 pA probe with dose/area in each image of 4.1×10^3 $e/\text{Å}^2$, but with a total dose of 1.75×10^6 $e/\text{Å}^2$. 234 images were taken in particle 1's dataset, while 428 were taken in particle 2's. Particle 2 exhibits near perfect stability, while particle 1 has undergone shape and lattice changes during the dataset.

5.1.2 The TEAM stage

As discussed in Chapter 2, sample vibration and stage drift can destroy resolution. For atomic resolution microscopy, even more stringent requirements are placed on the stability of the stage. During tomographic tilting, the stage is moved frequently, which can introduce drift. Rather than a mechanical tilting stage (like most commercial microscopes) TEAM I is also equipped with a unique, piezo controlled stage [55]. The TEAM stage is a 5 axis (x, y, z, α and γ) tilt stage that is entirely piezo controlled. This stage, which was custom built at NCEM, is unique and offers superior vibration and drift stability (Fig. 5.2) [55]. The stage consists of two "chopsticks" that hold a 1mm sample (Fig. 5.3). While the stage offers many advantages over a conventional mechanical stage, it is necessary to adapt the samples to fit into the 1mm holder.

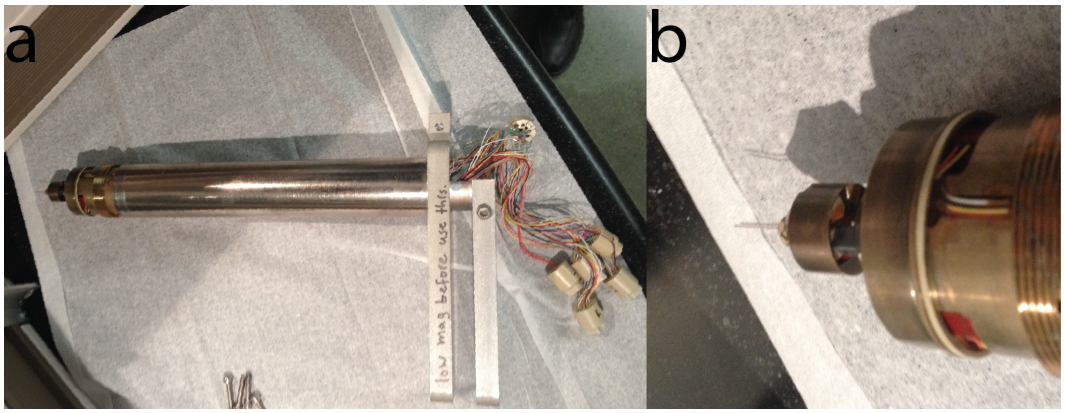

Figure 5.2: An image of the TEAM stage, (a) the entire stage and (b) a close up of the chopsticks. Normally the stage is permanently fixed in the microscope, but here it has been removed for repairs.

Despite its unconventional design, the TEAM stage can be used in a conventional tomography geometry (Fig. 5.3). In this setup, a 1mm silicon nitride grid with two long slits is used as a substrate. Nanoparticles are deposited onto the delicate grid using a nebulizer. This substrate, which was custom designed for

the TEAM stage, is glued into a 1 mm brass ring (Figs. 5.3 and 5.4). This ring holds the sample inside, while the outer part has a groove inside which the two chopsticks rest. The gamma motion of the stage is used to align these slits perpendicularly to the tilt axis for maximum tilt range. Then, α is changed throughout the tilt series. Due to the small size of this sample and the 100 μm frame thickness, the tilt range is typically limited to $\pm 65°$.

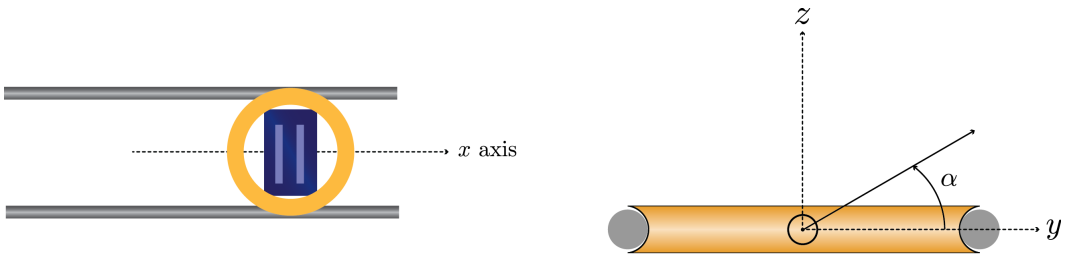

Figure 5.3: A schematic of the TEAM stage with a sample, viewed from above (left) and head on (right). The sample consists of a custom grid, with a 100 μm thick silicon frame and 50 μm$\times$450 μm, 5 nm thick silicon nitride windows. The windows are coated with carbon to enhance conductivity. This grid is mounted on a brass sample support (called a "puck") that is held by the chopsticks. The x-axis, which is the axis of α rotation, is along the two chopsticks, with the y-axis perpendicular to x and z extending vertically from the surface of the sample.

5.2 Tomography in a needle geometry

A limiting factor in conventional tomography is the missing wedge. Due to the limited tilt range of the mechanical tilting system of the microscope or due to the fact that a typical sample would be shadowed at high tilt angles, most tomographic data is limited to $\pm 80°$. These missing projections correspond to a wedge of missing information in Fourier space. The missing wedge induces artifacts (stretching and blurring) along the beam direction. However, the unique capabilities of the TEAM stage allow for full $\pm 360°$ rotation in γ. Therefore, if

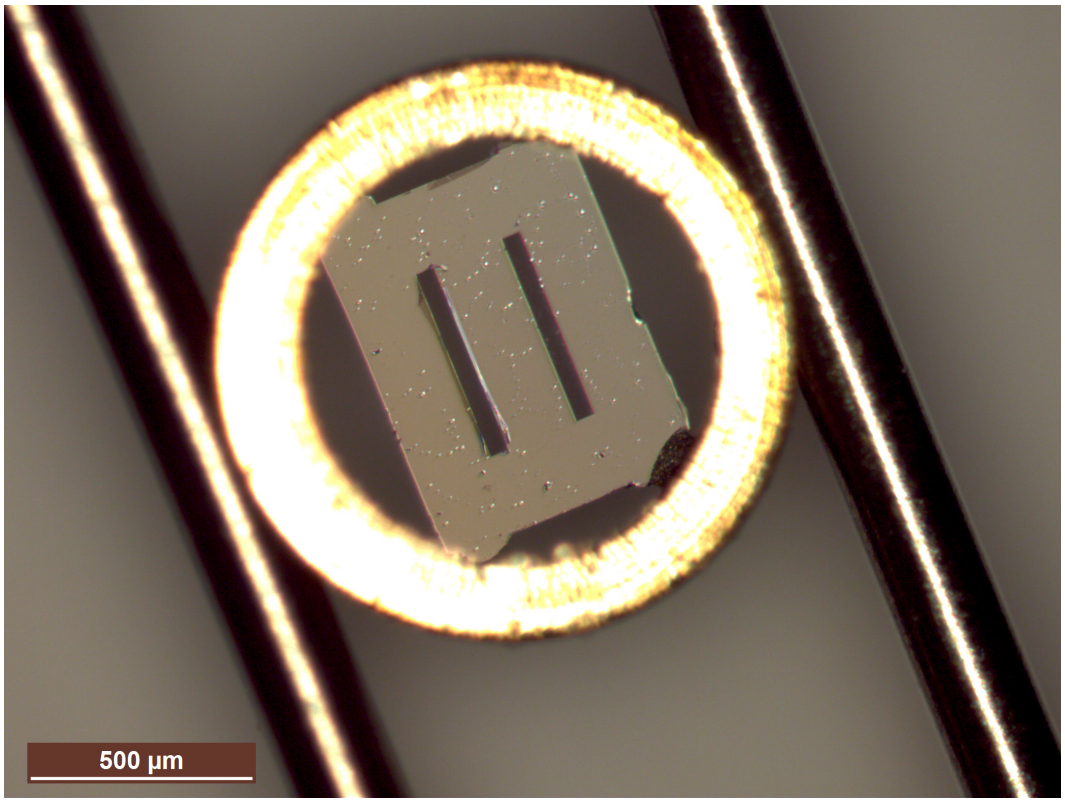

Figure 5.4: An image of an SiN grid mounted in a brass ring (puck) for the TEAM stage. The long slots will need to be oriented perpendicular to the tomography rotation axis.

the α angle is set to 90°, γ rotation can be used to collect a tomography data set, provided the sample has a needle shape (Figure 5.5). With this geometry, there is no missing wedge. Additionally, there is no background contribution from the substrate.

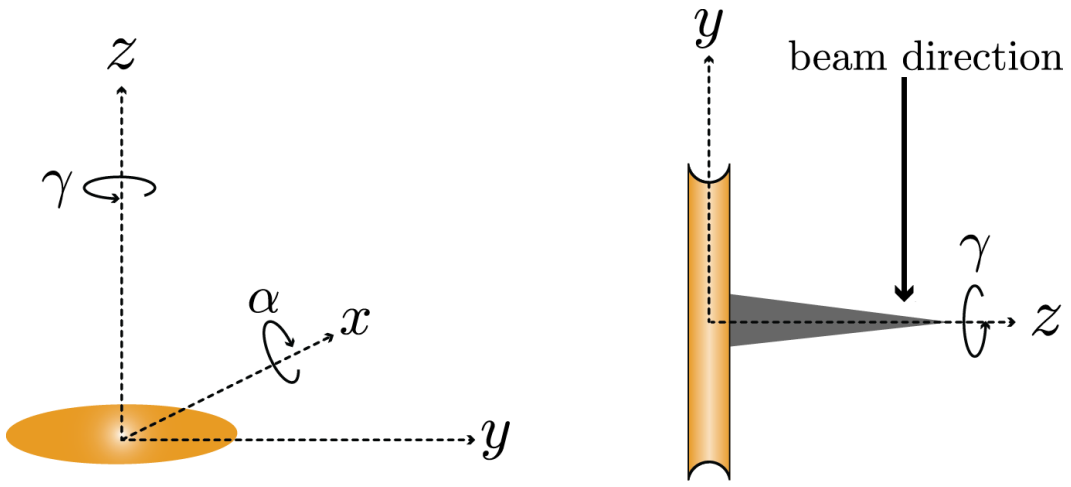

Figure 5.5: Basic setup for needle tomography, where γ is the tomography rotation angle. Here, the sample is first tilted to $\alpha = 90°$. This requires the sample geometry be a very sharp needle that extends perpendicularly from the sample surface.

Two style of samples can be produced for the needle geometry- in the first, a pillar is produced with a focused ion beam and mounted on a tomography puck, that is, a solid puck with a rounded outcropping (Fig. 5.6a). In the second, a sharpened wire is threaded through a puck with a small (250 μm) hole in the center (Fig. 5.7). The second style of sample is used in Chapter 6 to obtain a tilt series of a tungsten needle. Various needle samples are shown in Figure 5.8. This flexibility in sample production means that a wide variety of materials can imaged in this manner (Fig. 5.8).

Tomography data can be acquired using γ motion only, however in the case of crystalline samples, both angles can be used to rotate about a specific crystalline zone axis, as shown in Figure 5.9. This more complicated tilt scheme allows for

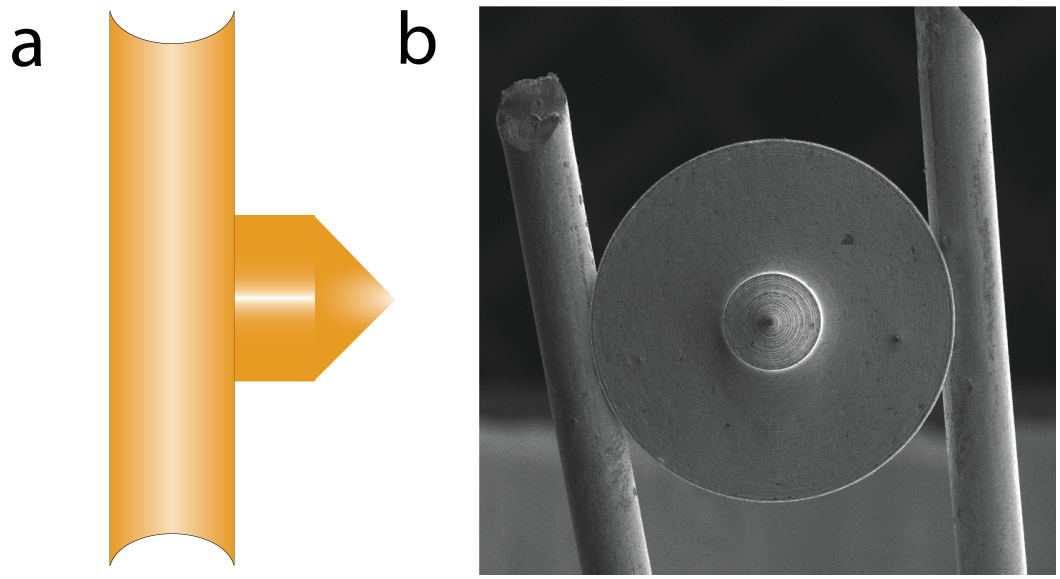

Figure 5.6: a) A schematic of a tomography puck, with an outcropping on which a needle can be mounted using a focused ion beam. b) An SEM image of a tomography puck.

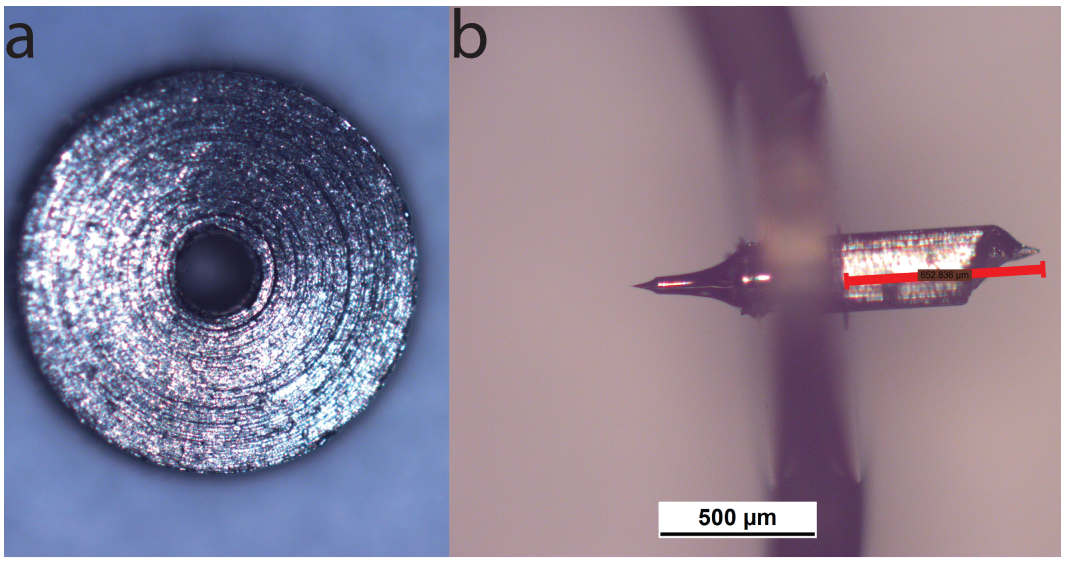

Figure 5.7: a) A front view of a puck for mounting a wire to be imaged in the TEAM I. b) A side view of a wire tomography puck with a wire mounted.

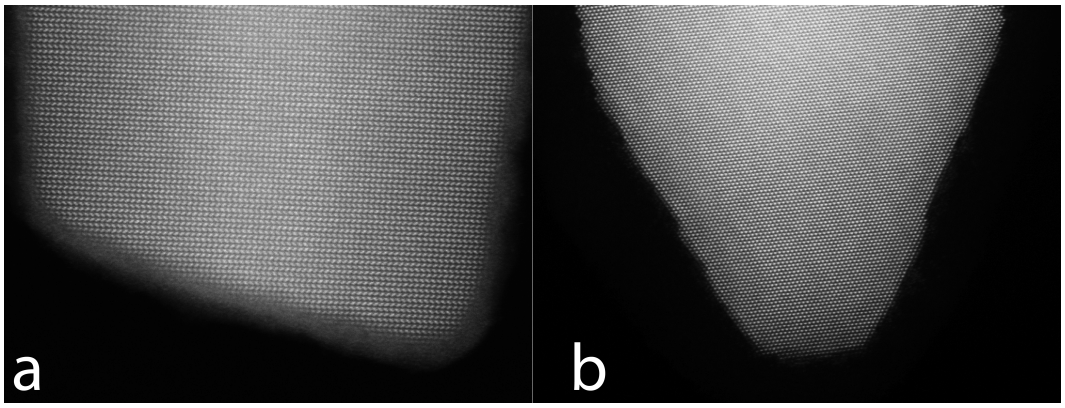

Figure 5.8: a) A GaAs needle with In inclusions imaged along a <210>axis. This needle was produced using a focused ion beam and mounted on a tomography puck. b) A tungsten needle mounted in a wire puck imaged a long a <111>direction. Once mounted in the appropriate puck, data acquisition is identical for these two styles of sample.

additional calibrations and checks on the data to be performed, as the crystal orientation with respect to the tomography tilt axis is exactly known. The calculation to determine the stage angles necessary to rotate to a set of equally sloped projection angles about a specific crystal axis is given in Appendix A.2.

5.2.1 Preparation of tungsten needle samples [1]

Sharp tungsten tips were prepared by electrochemical etching in an aqueous solution of sodium hydroxide, NaOH. The tungsten wire to be etched acts as the anode and a tungsten loop surrounding the wire acts as the cathode. At the cathode, the reaction that occurs is [56]

$$6\mathrm{H_2O} + 6e^- \rightarrow 2\mathrm{H_2}(g) + 6\mathrm{OH^-} \tag{5.1}$$

[1] Sample etching station was developed by W. Theis, Nanoscale Physics Research Laboratory, School of Physics and Astronomy, University of Birmingham, Edgbaston, Birmingham B15 2TT, UK.

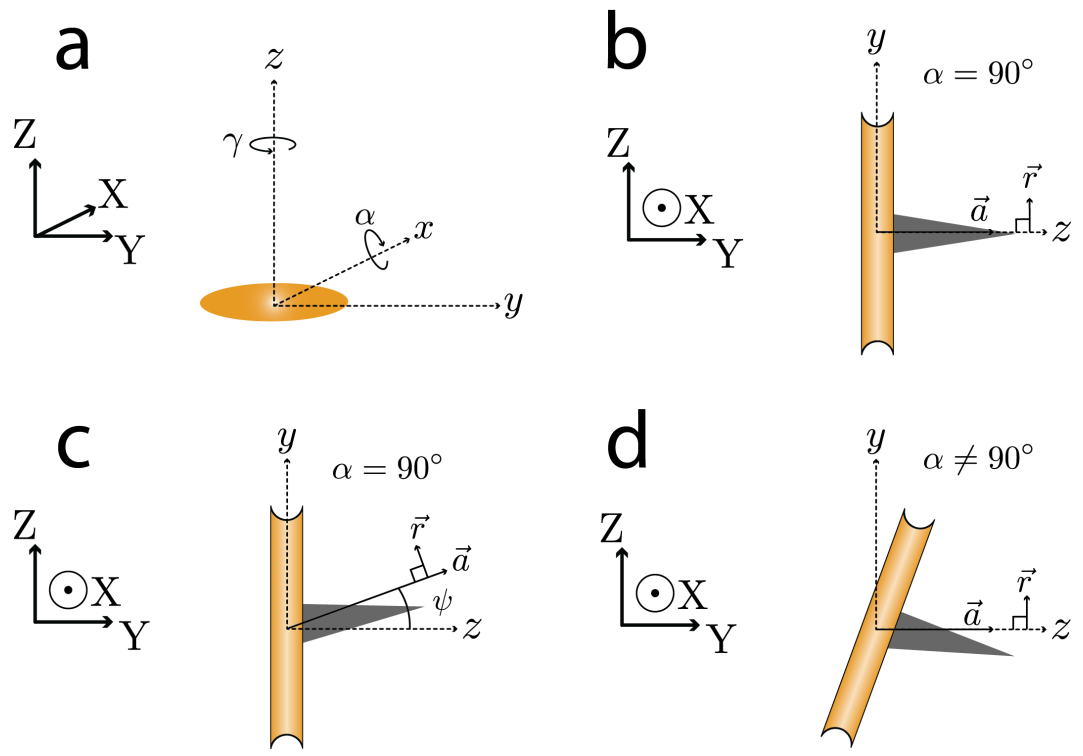

Figure 5.9: Schematic for gamma tomography. Stage coordinates are indicated by x, y, and z, which move with the sample. Lab coordinates are indicated by X, Y, and Z, which are fixed. The beam direction is the -Z direction. a) The two angular degrees of freedom of the TEAM stage, α and γ. $\vec{a}$ indicates the axis of interest (the axis about which rotation occurs) and $\vec{r}$ is the projection direction, which is $\perp$ to $\vec{a}$. b) In an ideal geometry, only γ needs to be changed during the tomographic data set, with $\alpha = 90°$. c) In a more realistic sample geometry, $\vec{a}$, the axis of interest, will be at an angle ψ from the $\alpha = 90°$ axis. d) In the geometry described in (c), both α and γ motion is needed.

While at the anode

$$\mathrm{W}(s) + 8\mathrm{OH} \rightarrow \mathrm{WO}_4^{2-} + 4\mathrm{H_2O} + 6e^-. \tag{5.2}$$

Combining Equations 5.1 and 5.2, the total reaction is

$$\mathrm{W}(s) + 2\mathrm{OH}^- + 2\mathrm{H_2O} \rightarrow \mathrm{WO}_4^{2-} + 2\mathrm{H_2}(g). \tag{5.3}$$

At the anode, this reaction can be described as an oxidation of the tungsten wire, creating tungstate (WO_4^{2-}), which is water soluble and subsequently dissolved into the solution. At the cathode, water is reduced into OH^- and hydrogen gas [56]. The overall result is thinning of the tungsten wire, forming a notch, which is thinned and eventually will break off, resulting in a sharp tip.

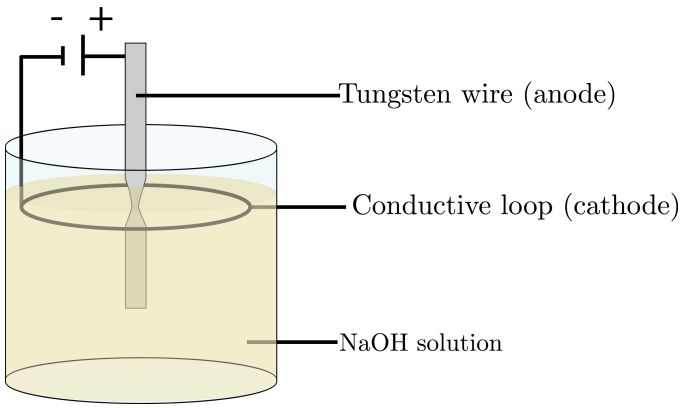

Figure 5.10: A schematic of the tungsten tip etching setup.

To prepare a sample for etching, a 250 μm diameter tungsten wire (99.95% purity) is first annealed under tension until breaking, creating a large crystalline domain with the [011] direction aligned along the long axis of the wire. The wire is then etched into a needle via a two-step etching process. In the first step (Fig. 5.11a), a 5M aqueous sodium hydroxide solution was used to create a notch shape in the wire, while also thinning the portion of the wire surround the notch to 230 μm, with the notch being 100 μm in diameter. After cleaning in deionized water, a 1M solution is used to further thin the wire, eventually breaking it to form a

sharp tip shape (Fig. 5.11a). This method results in tips that vary in size but are typically <50 nm in diameter at the smallest point (Fig. 5.11). After thinning, the wire can be annealed to remove any oxide growth, and then it is mounted by hand in a wire tomography puck (Fig. 5.7). The excess wire on the back of the sample can either be removed via a pulsed laser mill, or etched away in a process similar to etching the tip. Once sharpened, the tips themselves can be imaged, or layers of thin metal or even nanoparticles can be deposited on the tips.

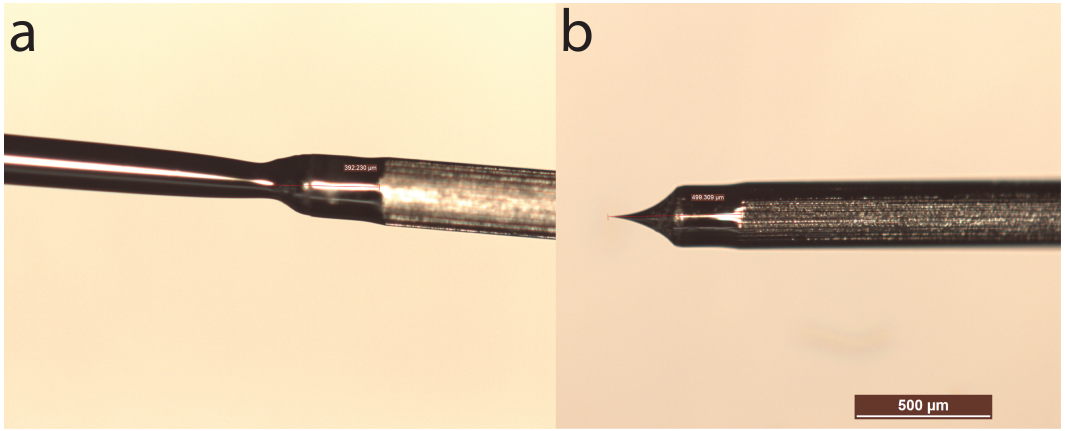

Figure 5.11: A tungsten wire during the the two-step etching process. a) After completion of the first etch in 5M NaOH, the wire is notched, and a portion is smoothed. b) The second etch produces the tip in 1M NaOH. The hyperbolic shape is indicative of a sharp tip.

5.3 Data post processing

To produce an accurate atomic resolution tomographic reconstruction, additional calibrations and checks must take place to ensure that the data is as close to perfect as possible. One source of error that needs to be addressed at this level of accuracy is scanning coil distortion. As mentioned in Chapter 1, STEM images are formed via a scanning probe, which rasters across the sample in a grid to

form a pixelated image. Normally, these pixels are assumed to be square, however this is not actually the case- imperfect calibration of the lenses in the microscope that control scanning in the X and Y directions can result in pixels that are rhombohedral, instead of square (Fig. 5.12a). This can be corrected by calculating a distortion matrix and applying a shear correction to the image using Fourier methods [57]. The distortion matrix is calculated by measuring Bragg peaks of a known crystal lattice (Fig. 5.12b).

To calculate the distortion matrix, the location of two or more Bragg peaks are measured from an image of a known crystal lattice and described by two vectors ($\overrightarrow{v_1}$ and $\overrightarrow{v_1}$ in Figure 5.12b). One vector is selected as a reference (in this case, $\overrightarrow{v_1}$). Then the matrices V_{exp} and V_c are given by

$$\mathrm{V}_{exp} = \begin{pmatrix} \overrightarrow{v_1} \\ \overrightarrow{v_2} \end{pmatrix} \text{ and } \mathrm{V}_c = \begin{pmatrix} \overrightarrow{v_1} \\ \overrightarrow{v_{2c}} \end{pmatrix} \tag{5.4}$$

where $\overrightarrow{v_{2c}}$ is the theoretical value of $\overrightarrow{v_2}$ in relation to $\overrightarrow{v_1}$. Then the correction matrix M is given by

$$\mathrm{V}_c = \mathrm{M}\mathrm{V}_{exp} \text{ or } \mathrm{M} = \mathrm{V}_c\mathrm{V}_{exp}^{-1}. \tag{5.5}$$

Figure 5.13 shows a Si (100) test sample (a) and its Fourier transform before (b) and after (c) scanning coil correction. In Figure 5.13b, the Bragg peaks are not perpendicular to each other, while in (c) they are. The correction applied to these data corresponds to $\sim 2^\circ$ of shear, which creates a noticeable effect in the reconstruction if not corrected. To correct tomographic data, a correction matrix calculated on a test sample using similar imaging conditions. In the case of Chapter 6, the sample itself was used to calculate M. Additional corrections to the data, such as correction of the rotation axis, can be bundled into this correction and performed in one step. If more than one image is taken, a linear drift coefficient is also calculated and compensated for in this step. Once these preprocessing steps have taken place, the data can be aligned and reconstructed

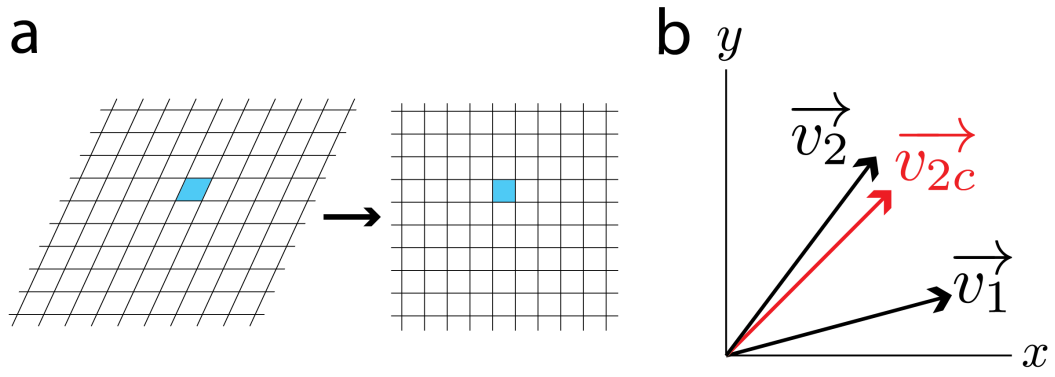

Figure 5.12: a) Scanning error in the microscope can cause the measured grid points to sample on a rhombohedral grid, rather than square. This error will result in lattice distortion in the final reconstructed object if not corrected. b) A correction matrix can be measured using the Bragg peaks of a known crystal. If scanning distortion is present, both the relative angle and location of the peaks will be affected. Here, $\overrightarrow{v_1}$ and $\overrightarrow{v_2}$ represent the measured Bragg peaks. $\overrightarrow{v_{2c}}$ represents the corrected Bragg peak $\overrightarrow{v_2}$ with respect to $\overrightarrow{v_1}$.

as usual using EST.

5.4 Summary

Developing true atomic resolution tomography has required not only using an aberration corrected microscope to collect the data, but also significant development of sample preparation and data post processing. The TEAM I microscope allows for a unique tomography geometry which allows for for full $\pm 180^\circ$ tilt, eliminating the missing wedge. Tungsten needle samples have been developed not just as an interesting sample, but also as a potential sample mount for nanoparticles. Chapters 6 and 7 discuss the application of aberration corrected electron tomography to two different systems. Chapter 6 discusses the application of atomic resolution tomography to a needle sample, while Chapter 7 discusses its applica-

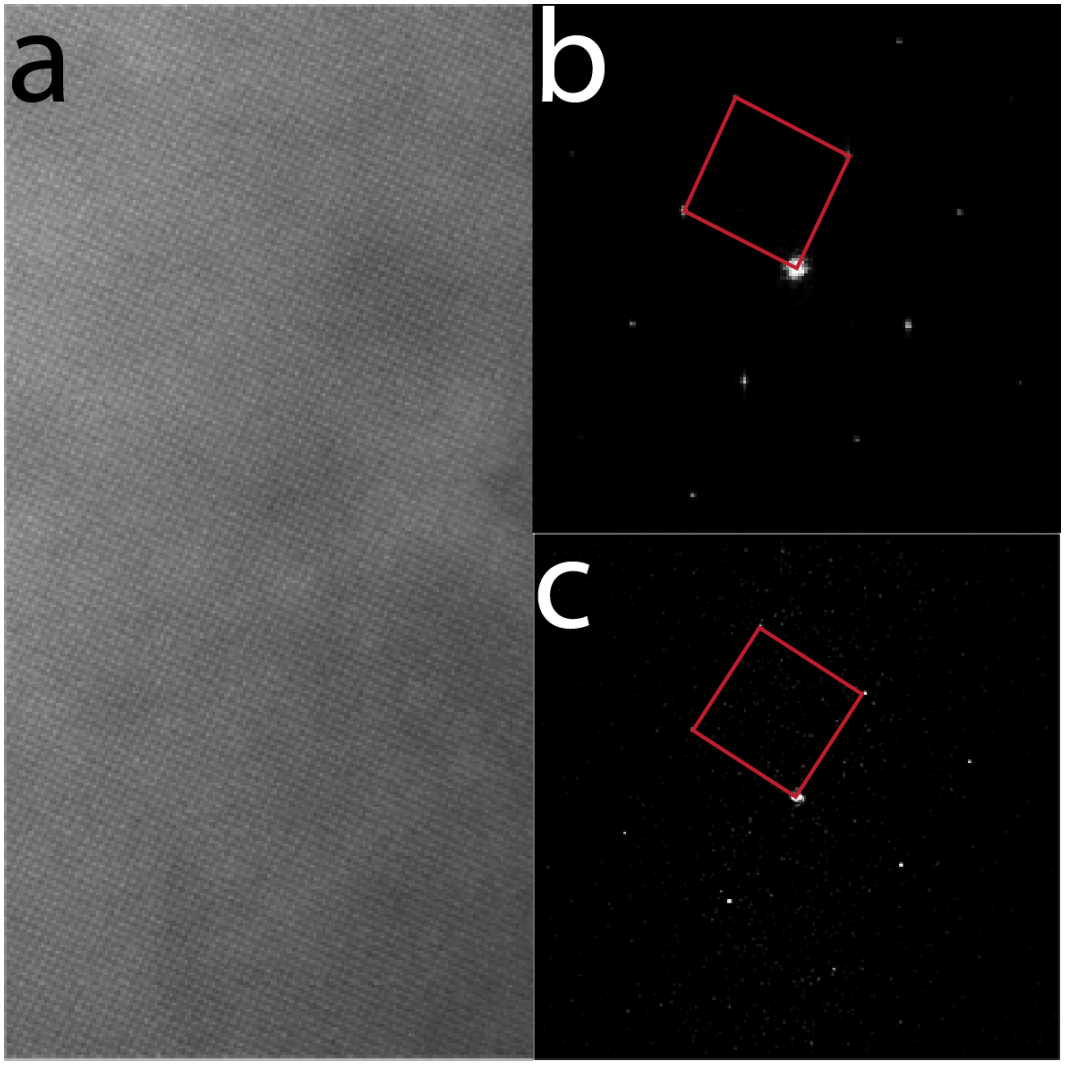

Figure 5.13: a) An ADF-STEM image of a Si (100) test sample. b) The Fourier transform of the uncorrected sample. Although in this orientation the Bragg peaks should be at right angles to each other and equidistant from the origin, in the uncorrected data they are not. c) After the correction, the Fourier transform of the silicon sample matches the known values for this crystal.

tion to a bimetallic nanoparticle system in a conventional tomography geometry.

CHAPTER 6

Three-dimensional positions of individual atoms revealed by electron tomography [1]

6.1 Motivation

In 1959, Richard Feynman challenged the electron microscopy community to locate the positions of individual atoms in substances [58]. Over the last 55 years, significant advances have been made in electron microscopy. With the development of aberration-corrected electron optics [59, 60], two-dimensional TEM imaging has reached sub-0.5 Å resolution [61]. Uncorrected electron tomography combined with EST [25], has achieved the results described in Chapters 3 and

[1] This chapter is a version of is a version of "Rui Xu, Chien-Chun Chen, Li Wu, M. C. Scott, W. Theis, Colin Ophus, Matthias Bartels, Yongsoo Yang, Hadi Ramezani-Dakhel, Michael R. Sawaya, Hendrik Heinz, Laurence D. Marks, Peter Ercius and Jianwei Miao,"Three-dimensional positions of individual atoms in materials revealed by electron tomography", (2015) (submitted)", with author contributions as follows: J.M. directed the project; W.T. prepared the samples, W.T. and M.C.S. acquired the data; C.-C.C., L.W., M.B., R.X. and J.M. conducted the image reconstruction and atom tracing; R.X., M.R.S. and J.M. performed the atom refinement; R.X. and J.M. conducted the multislice calculations; C.O., R.X., W.T., P.E., M.C.S., Y.Y., L.D.M. and J.M. analyzed and interpreted the results; L.D.M. did the DFT calculations; H.H., H.R.D., W.T. and C.O. carried out the MD simulations; J.M., C.O., R.X., W.T., M.B., L.W., M.C.S., P.E., H.R.D., H.H. and L.D.M. wrote the manuscript.

4. More recently, TEM has been used to determine the 3D atomic structure of gold nanoparticles by averaging 939 particles[62]. Notwithstanding these important developments, however, Feynman's 1959 challenge - 3D localization of the positions of atoms in a substance without using averaging or a priori knowledge of sample crystallinity - remains elusive. Here, aberration corrected electron tomography has been combined with the advanced EST reconstruction algorithm to determine the 3D positions of 3,769 individual atoms in a tungsten needle, as well as a point defect inside the needle. The individual atomic positions can be compared to a perfect bcc lattice to calculate the atomic displacement field and the full strain tensor in three dimensions.

6.1.1 Data acquisition and image preprocessing

The sharp tungsten tip sample was produced as described in Chapter 5. Tomographic data was acquired using the TEAM I at the National Center for Electron Microscopy operated at 300 kV accelerating voltage in ADF-STEM mode (convergence semi-angle: 30 mrad; detector inner and outer semi-angles: 38 mrad and 200 mrad; aberration-corrected probe size: 50 pm; beam current: 70 pA). The tomography rotation axis was chosen to be the [011] crystallographic axis of the W sample. A tomographic tilt series of 62 projections was acquired from the W sample at EST angles calculated as in Appendix A.2, covering the complete angular range of $\pm 90^{\circ}$. Two images of 1024×1024 pixels each with 6 μs dwell time and 0.405 Å pixel resolution were acquired at each angle. To focus the projections, a small focus box was placed on a portion of the tip that was not used in the reconstruction. This area was used to focus carefully to avoid damaging the tip. Throughout the dataset, astigmatism was checked periodically on a portion of the tip not used in the reconstruction.

Preprocessing of images involved compensating for constant sample drift and

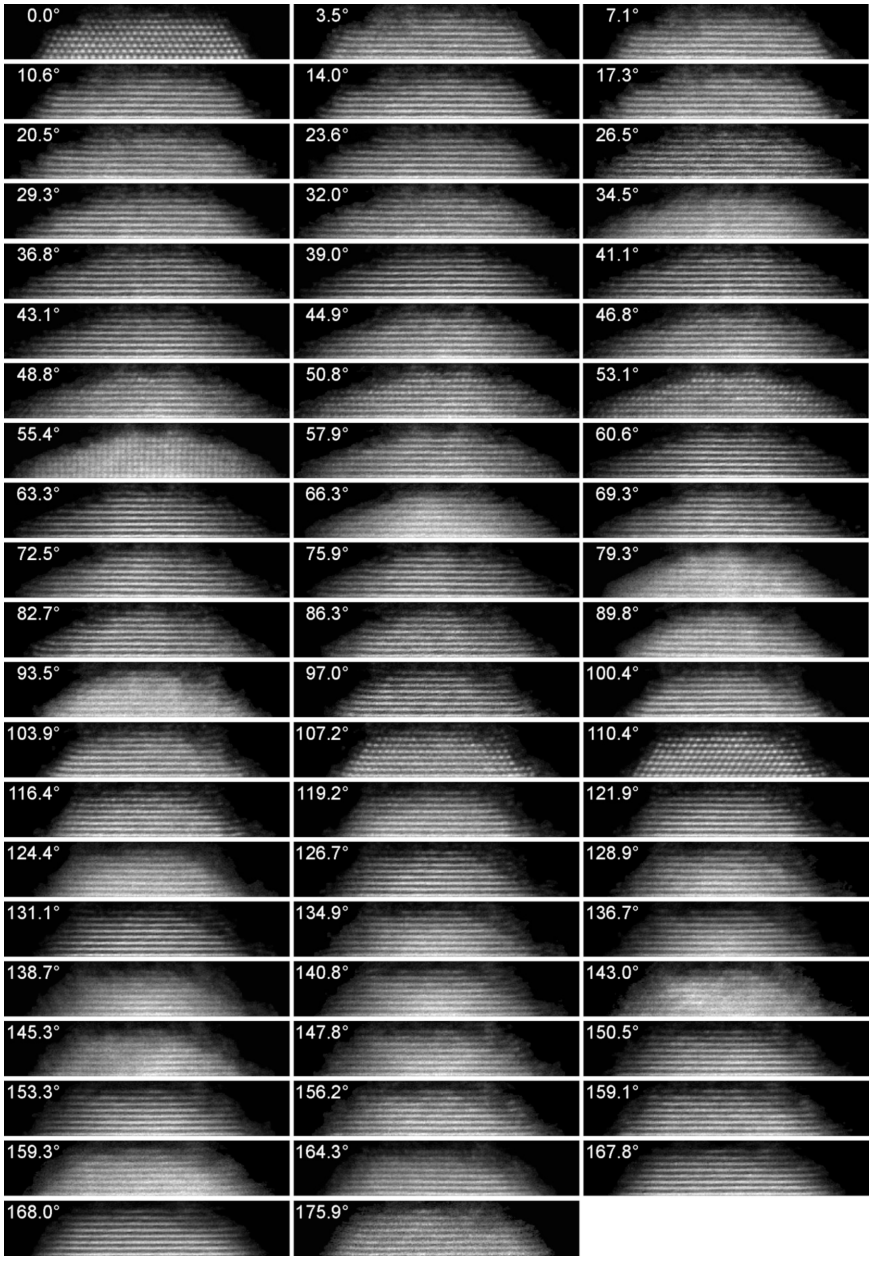

Figure 6.1: A tilt series of 62 experimental projections of the apex of a tungsten needle after performing sample drift, scan distortion correction and background subtraction, where the vertical image axis is the tilt axis.

STEM scanning coil distortion. Sample drift was determined from the relative shift of the pairs of images taken for each EST projection angle. The STEM scanning coil distortion was determined from the Fourier transform of a region 18.5 nm from the apex in the 0° projection assuming a bulk bcc tungsten lattice structure in this region. The ADF-STEM images were remapped by Fourier-based methods [57] to correct for effects of the measured drift and to achieve square pixels of 0.405 Å pixel size. Due to the nature of the tilt series, the tomography axis has a different in-plane orientation in the ADF-STEM image for each EST angle. The Fourier transform of the region 12.5 nm from the apex in the individual projections was used to determine the orientation of the [011] tomography axis. The images were individually rotated using Fourier methods [57] to align the [011] direction along the image vertical. The final tilt series, after preprocessing and background subtraction, is shown in Figure 6.1.

6.1.2 Reconstruction, atom tracing, and refinement

The 62 projections were aligned and reconstructed by EST as described in Chapter 1 and similarly to the reconstructions in Chapters

From this reconstruction, the positions of individual atoms can be calculated by fitting a Gaussian to local maxima in the reconstruction. This method was used on three different reconstructions- the raw reconstruction, a reconstruction from projections that were denoised, and a reconstruction that was gently Weiner filtered [63]. Once the positions were calculated, they were refined by comparison to the original data. The final atomic positions are shown in Figures 6.3 and 6.4.

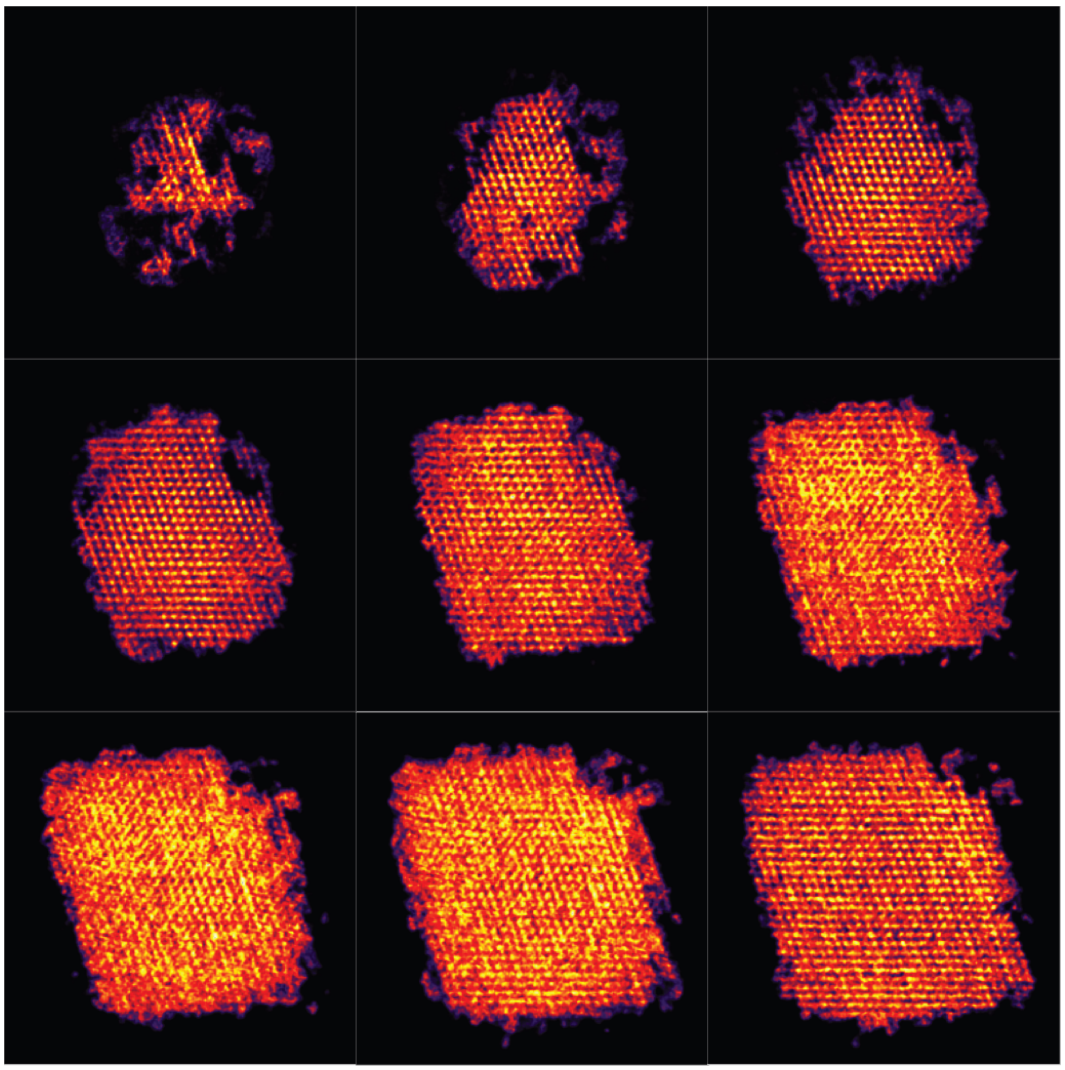

Figure 6.2: Slices through the reconstructed density of the tungsten tip. This reconstruction has been smoothed but has not been filtered in any way.

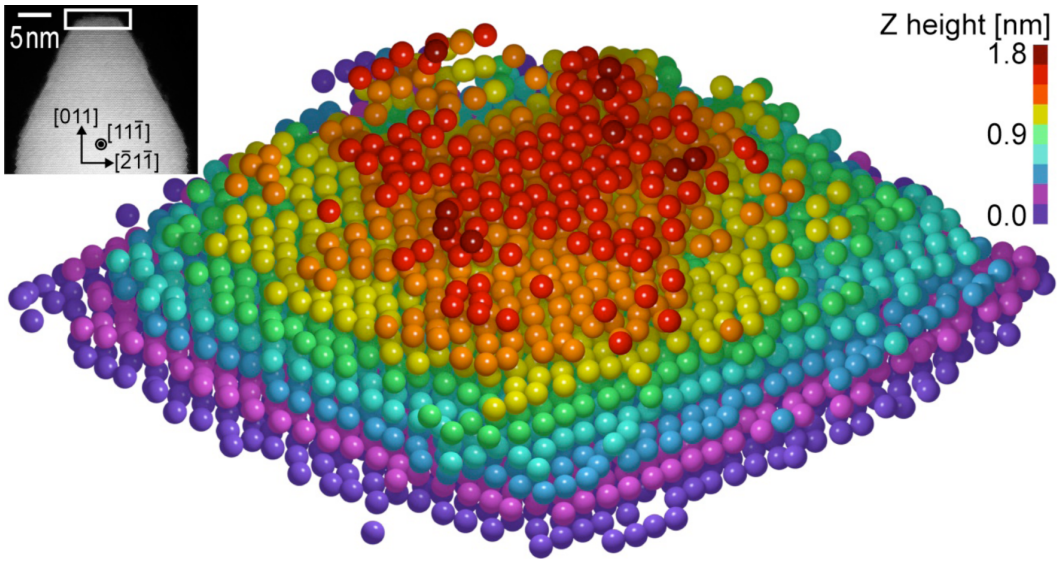

Figure 6.3: 3D positions of individual atoms in a tungsten needle sample revealed by electron tomography. The experiment was conducted using an aberration-corrected STEM. A tilt series of 62 projections was acquired from the sample by rotating it around the [011] axis. The inset shows a representative projection at 0°. After post data analysis, the tilt series of the apex part of the sample (labelled with a rectangle in the inset) was reconstructed by the EST method. The 3D positions of individual atoms were then traced from the reconstructions and refined using the 62 experimental projections. The 3D atomic model of the sample consists of 9 atomic layers along the [011] direction, labelled with crimson (dark red), red, orange, yellow, green, cyan, blue, magenta and purple from layers 1 to 9, respectively.

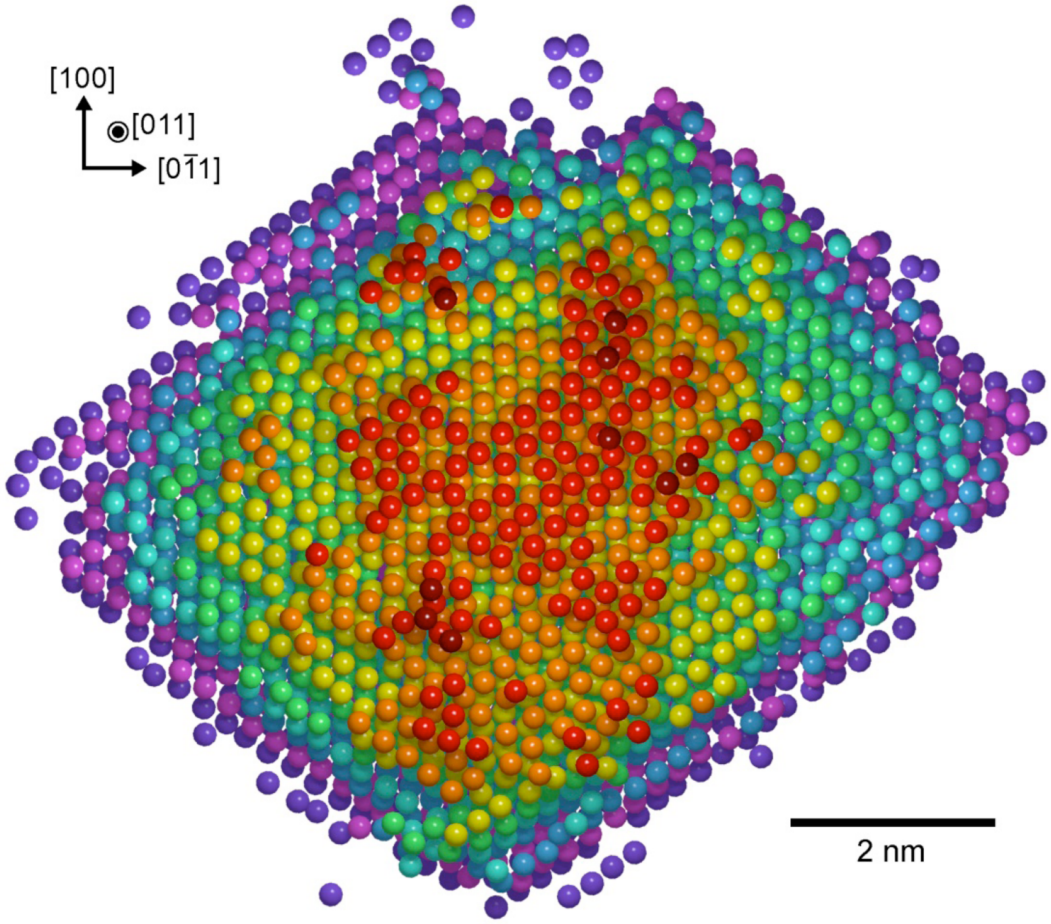

Figure 6.4: Top view along the tilt axis of the 3D atomic model obtained from the 62 experimental projections of the apex of the tungsten needle. Layers 1-9 (from the top to bottom) are labelled with crimson (dark red), red, orange, yellow, green, cyan, blue, magenta and purple, respectively. Several isolated atoms in layer 9 are supported on layer 10, which was not reconstructed.

6.2 Results

6.2.1 Identification of individual atoms and a point defect

Figures 6.3 and 6.4 shows the final 3D atomic model after reconstruction and refinement, consisting of 9 atomic layers along the [011] direction. The average R_1-factor between the experimental and calculated projections was 17.1%. The precision of the 3D atomic positions was determined from the experimentals data to be ∼19 pm, with contributions of approximately 10.5, 15 and 5.5 pm along the x-, y- and z-axes, respectively.

The ability to determine the positions of single atoms with high precision allowed the identification of a point defect in the tungsten material in three dimensions. Figures 6.5d and e show the 3D volume and surface renderings of three consecutive layers of atoms surrounding the point defect. A quantitative comparison of the density in the defect site and its surrounding atoms for all three reconstructions (raw, Wiener filtered and sparsity denoised) all strongly indicate a tungsten atom is not located at this site. While a substitutional point defect cluster of light atoms is energetically favorable in tungsten [64], a definitive identification of the substitutional atom species requires an experimental tilt series with a better signal to noise ratio.

6.2.2 Determination of 3D strain

With the atomic positions identified, 3D displacement and strain fields could be calculated. Projectional images of zone axes indicate that the apex of the tip is strained, while the bulk is not (Fig. 6.6). The center of the tip was used to measure the unstrained bcc lattice of the tungsten tip. After excluding atoms that didi not lie on the bcc lattice, the displacement field was determined by

comparison to the unstrained bcc lattice.

Figures 6.5a-c and 6.7 show the 3D atomic displacement field calculated as the difference between the measured atomic positions and the corresponding ideal bcc lattice sites. The tip exhibits expansion along the $[0\bar{1}1]$ direction (x-axis) and compression along the [100] direction (y-axis). The atomic displacement field in the z-axis is less than half the magnitude of that in the x- and y-axes. The 3D atomic displacement field was used to determine the full strain tensor in the material.

Calculation of the strain tensor requires differentiation of the displacement field making it more sensitive to noise. Thus, the atomic displacement field was convolved with a 5.5 Å wide 3D Gaussian kernel to increase the signal to noise ratio, but also reduced the 3D spatial resolution to ∼1 nm. Figures 6.8a-d show the distribution of the atoms in layers 2-9 and the corresponding smoothed 3D displacement field along the x-, y- and z-axes, respectively. The six components (ε_{xx}, ε_{yy}, ε_{zz}, ε_{xy}, ε_{xz} and ε_{yz}) of the full strain tensor (Figs. 6.8e-j) were determined from the smoothed displacement field with a precision of $\sim 10^{-3}$. The ε_{xx}, ε_{yy}, ε_{xz} and ε_{yz} maps exhibit features directly related to lattice plane bending, expansion along the x-axis and compression along the y-axis. Shear in the x-y plane is most visible in the ε_{xy} map. Compared to the other components, the ε_{zz} map is more uniform. By calculating the eigenvalues and eigenvectors, we obtained the principle strains to be approximately 0.81%, -0.87%, and -0.15% along the [0.07 0.78 -0.63], [1.00 -0.08 0.01], and [0.04 0.63 0.78] directions, respectively.

To understand the origin of the strain field, the 3D model was projected along the [100], $[0\bar{1}1]$, and $[1\bar{1}1]$ directions (Fig. 6.9). A comparison of the projected atomic positions with an ideal bcc lattice showed that the atomic displacements become larger closer to the surface particularly near steps (Fig. 6.9a). This suggests that the tungsten positions and/or the chemical composition changed near the surface. Carbon intercalation between the tungsten layers leading to a local

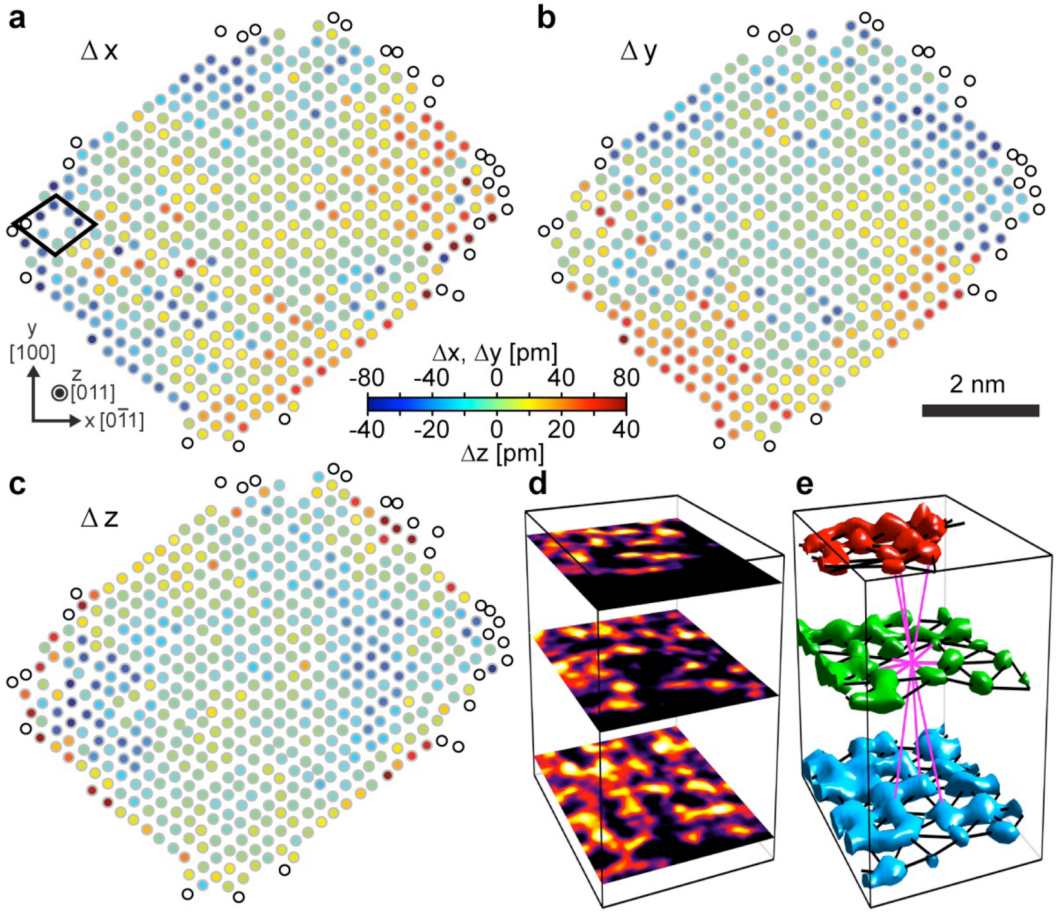

Figure 6.5: 3D atomic displacement field and 3D determination of a point defect in the tungsten needle sample. a, b and c, Atomic displacements in layer 6 of the tungsten sample along the x-, y- and z-axes, respectively, exhibiting expansion along the [0$\bar{1}$1] direction (x-axis) and compression along the [100] direction (y-axis). The atomic displacements in the z-axis are smaller than those in the x- and y-axes. The atoms with white dots are excluded for displacement field measurements due to their relatively large deviations from a bcc lattice. The atomic displacement field in other layers is shown in Figure 6.7. d and e, 3D volume and surface renderings of a point defect in the tungsten sample (diamond-shaped region in (a)), clearly indicating no tungsten atom density at the defect site.

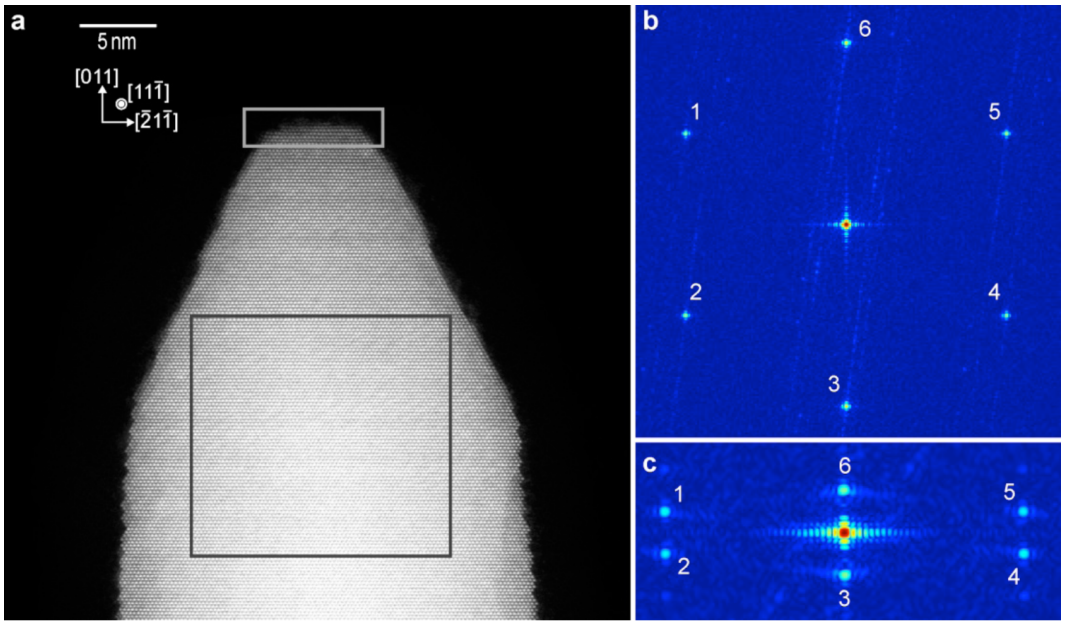

Figure 6.6: a, Experimental projection at 0° of the tungsten needle sample. b, Magnitude of the Fourier transform of a bulk region (black square), displayed in a logarithmic scale. The positions of the six discrete peaks are all 0.447 $Å^{-1}$ from the origin. The angles between two neighboring discrete peaks (from 1 to 6 counter-clockwise) are 60.07°, 59.98°, 59.95°, 60.07°, 59.98°, and 59.95°, respectively. As a reference, for an ideal bcc lattice, the positions of the corresponding six discrete peaks are 0.447 $Å^{-1}$ from the origin and the angle between two neighboring discrete peaks is 60°. c, Magnitude of the Fourier transform of the apex of the needle (white rectangle). Due to the rectangular shape of the selected region, the pixel size along the horizontal and vertical axes in (c) is different. The positions of six discrete peaks 1-6 from the origin are 0.445, 0.445, 0.444, 0.445, 0.445, and 0.444 $Å^{-1}$, respectively. The corresponding angles (from 1 to 6 counter-clockwise) between two neighboring discrete peaks are 59.53°, 60.28°, 60.19°, 59.53°, 60.28°, and 60.19°, respectively. These results indicate that the structure of the bulk part of the needle is consistent with an ideal bcc lattice, and the apex part is strained.

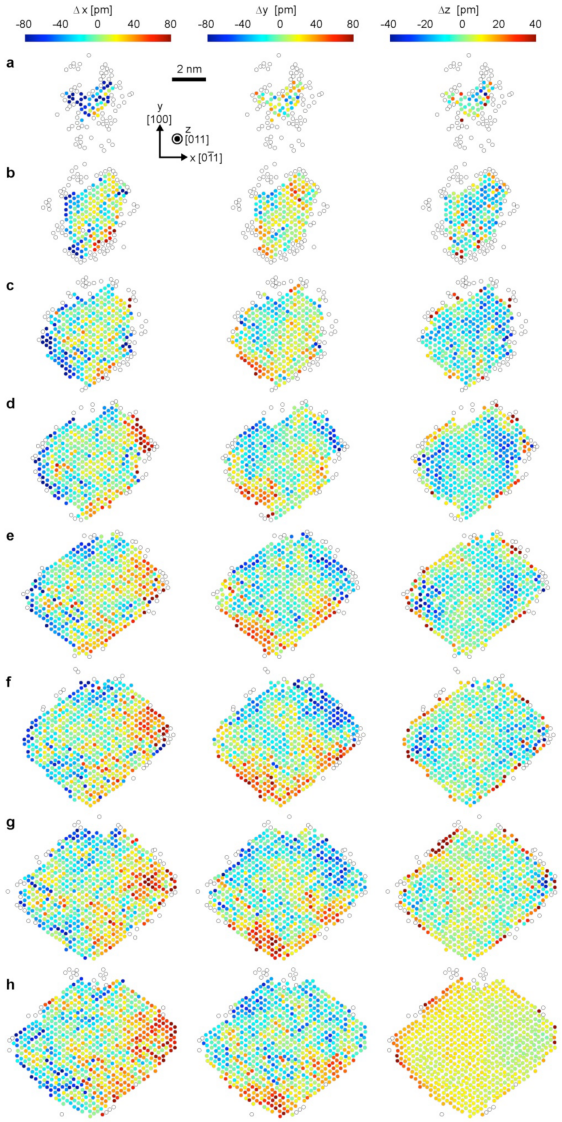

Figure 6.7: Atomic displacements in layers 2-9 of the tungsten sample along the x-, y- and z-axes, respectively, exhibiting expansion along the [0$\bar{1}$1] direction (x-axis) and compression along the [100] direction (y-axis). The atomic displacements in the z-axis are smaller than those in the x- and y-axes (note the colour scales). The atoms indicated by white dots and all atoms in layer 1 were excluded for displacement field measurements due to their relatively large deviations from a bcc lattice.

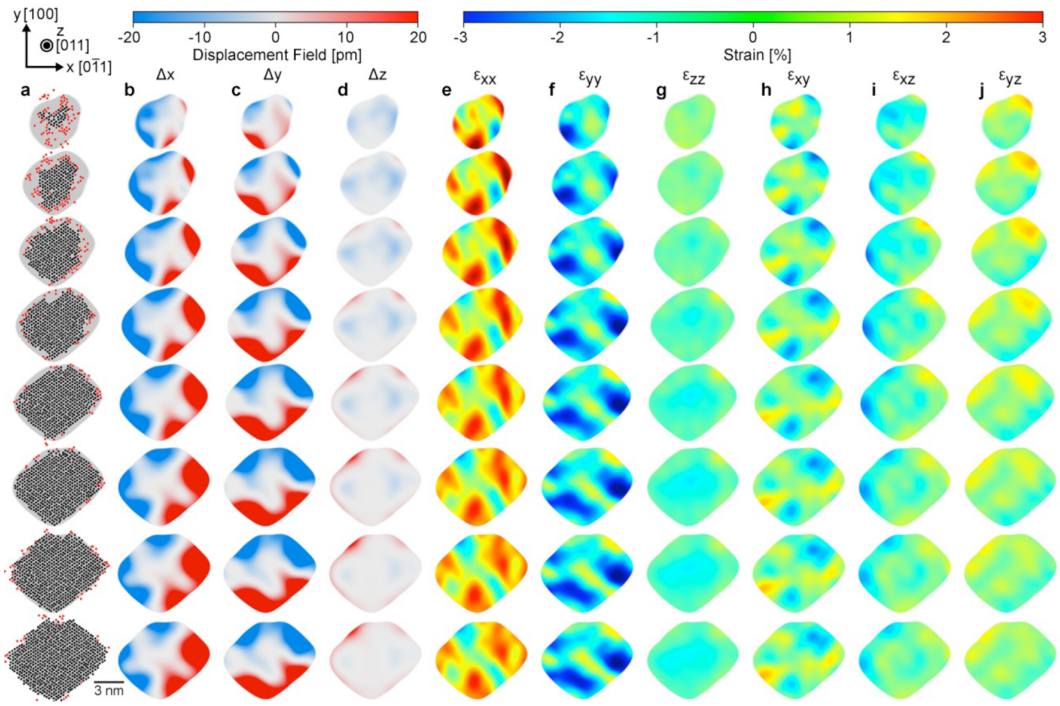

Figure 6.8: 3D strain tensor measurements in the tungsten needle sample. a, Atoms in layers 2-9 used for determining the 3D strain tensor, where layer 1 and other surface atoms in red are excluded for displacement field and strain measurements. b, c, and d, 3D lattice displacement field for layers 2-9 along the x-, y-, and z-axes, respectively, obtained by convolving the 3D atomic displacements with a 5.5-Å-wide 3D Gaussian kernel to reduce the noise and increase the precision. Expansion along the [0$\bar{1}$1] direction (x-axis) and compression along the [100] direction (y-axis) are clearly visible. e, f, g, h, i, and j, Maps of the six components of the full strain tensor, where ε_{xx}, ε_{yy}, ε_{xz}, and ε_{yz} exhibit features directly related to lattice plane bending, expansion and compression along the along the x- and y-axis, respectively. ε_{xy} shows shear in the x-y plane and ε_{zz} is more homogenously distributed.

expansion with octahedral coordination of the carbon is qualitatively in agreement with Figure 6.9. To understand the bending of tungsten lattice, another tungsten needle was prepared using the same sample preparation procedure, except that carbon was deposited on the needle before heating to 1200 °C in vacuum. ADF and bright-field STEM images along the [100] and [111] directions show clearer bending of the atomic columns (Fig. 6.10), with the density functional theory (DFT) calculation positions in good agreement with the ADF images (Figs. 6.9 and 6.10). Molecular dynamics (MD) simulations of a tungsten needle with and without the presence of carbon (6.11 and 6.12) show that the strain tensor approaches zero in the carbon-free needle. However, with intercalated carbon, the tungsten needle exhibits expansion and compression along the $[0\bar{1}1]$ and [100] directions, respectively, in agreement with the experimental measurements (Fig. 6.8). Thus, the experimental results, DFT calculations and MD simulations all indicate that the strain in the tungsten needle is induced by surface WC_x and the diffusion of carbon atoms several layers below the tungsten surface.

6.3 Summary

While TEM, electron diffraction and holography can measure strain in materials at 1 nm or better resolution [65–67], they are mainly applicable in two dimensions. Coherent diffractive imaging and X-ray diffraction microscopy can be used to image the full 3D strain tensor [68–70], but the resolution is presently limited to ∼30 nm [71]. This chapter describes an experimental method for measuring the full strain tensor in materials with a 3D resolution of ∼1 nm^3 and a precision of $\sim 10^{-3}$, which is expected to profoundly expand the understanding of the properties and functionality of materials at the nanoscale.

In conclusion, a general 3D structure determination method has been developed to localize the positions of individual atoms and point defects in materials.

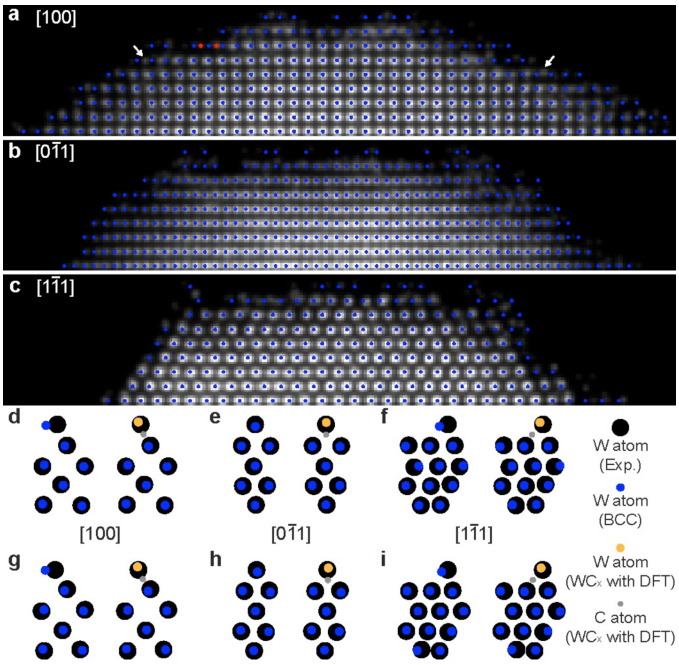

Figure 6.9: Projection of the experimental 3D atomic model along the [100], [0$\bar{1}$1], and [1$\bar{1}$1] directions, respectively, where the blue dots correspond to an ideal bcc lattice. In (a), some atomic columns on the left side are bent to the left and some on the right are bent to the right relative to the bcc lattice (white arrows). The atomic column displacements become larger closer to the surface, suggesting carbon atoms diffuse into the tip. In (b), some atomic columns on the left are slightly bent to the right and some on the right are slightly bent to the left. Atomic column positions match well with the bcc lattice in (c). These results further confirm the observation of expansion along the [0$\bar{1}$1] direction and compression along the [100] direction. d-i, Comparison of the locations of two surface atoms (red dots in (a)) and their neighbouring atoms for the experimental atomic model (in black), ideal bcc lattice (in blue) and DFT calculations (W atoms in yellow and C atoms in grey) along the [100], [0$\bar{1}$1] and [1$\bar{1}$1] directions, respectively. The good agreement between the experimental atomic model and DFT indicates the two surface atoms belong to WC_x.

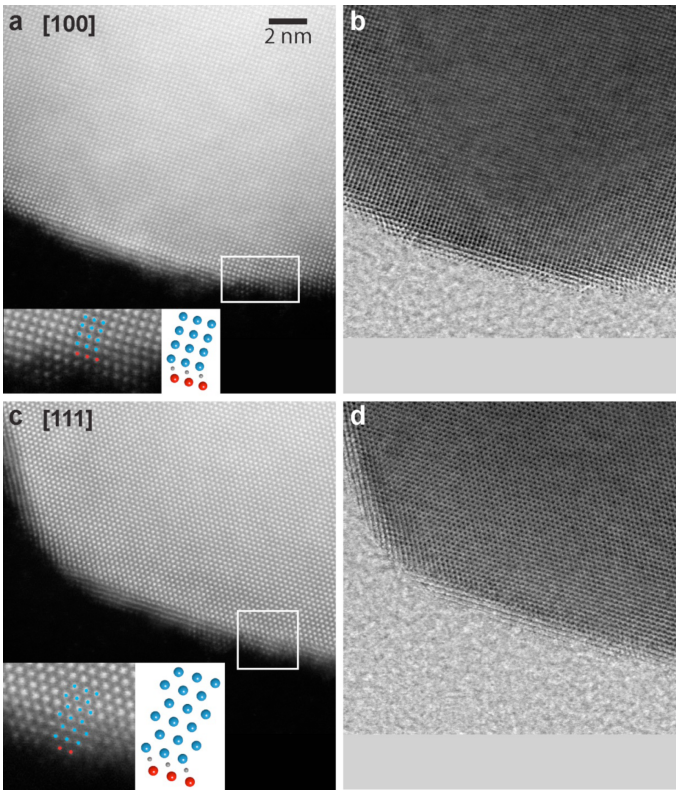

Figure 6.10: Another tungsten needle prepared under the same sample preparation procedure except that carbon was deposited on the tip before heating to 1200 °C in vacuum. a-d, ADF and bright-field STEM images of the needle sample at the [100] and [111] directions, respectively. Lattice bending near the surface is visible in (a) and (b). Two insets indicate the experimental surface structure agrees with the DFT calculations, where atoms in red and grey are the W and C atoms in WC_x and atoms in blue are the W atoms in a bcc lattice.

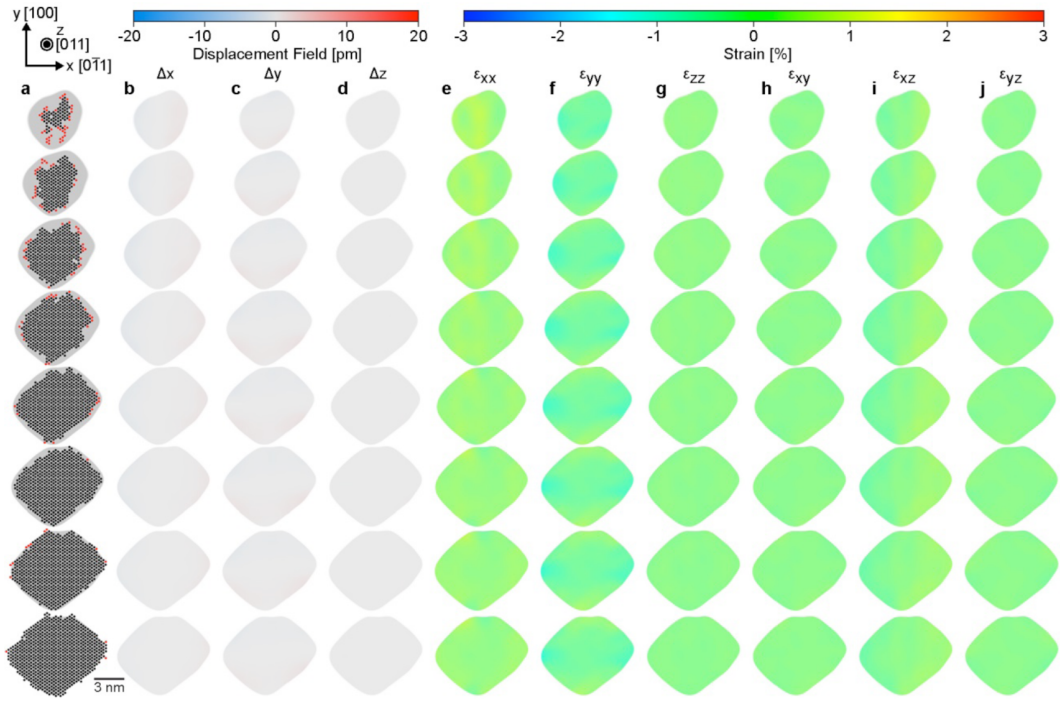

Figure 6.11: 3D strain tensor obtained from MD simulations of a carbon-free tungsten tip. a, Atoms in layers 2-9 were used to calculate the 3D strain tensor. b, c and d, 3D lattice displacement field for layers 2-9 along the x-, y-, and z-axes, respectively. e, f, g, h, i, and j, Maps of the six components of the full strain tensor (ε_{xx}, ε_{yy}, ε_{zz}, ε_{xy}, ε_{xz} and ε_{yz}). The procedure to calculate the atomic displacement field and the full strain tensor using the MD data was identical ,to that used in the analysis of the experimental data (Fig. 3). The MD simulation results show that the strain tensor approaches zero in the absence of carbon in the tip.

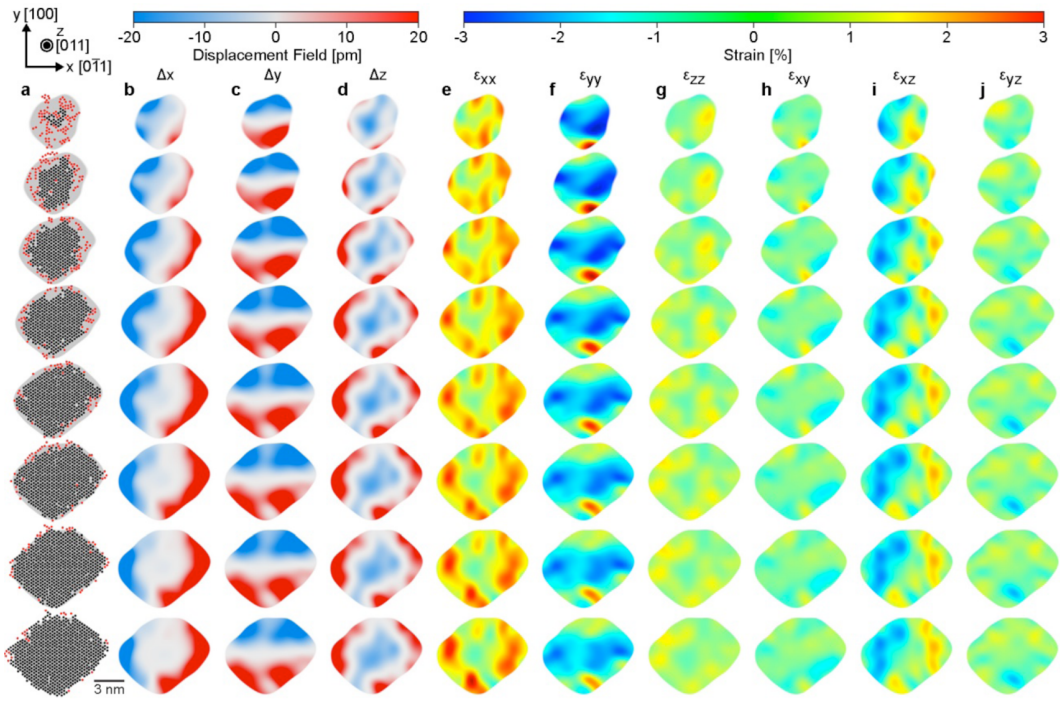

Figure 6.12: 3D strain tensor obtained from MD simulations of a tungsten tip containing carbon. a, Atoms in layers 2-9 were used to calculate the 3D strain tensor. b, c, and d, 3D lattice displacement field for layers 2-9 along the x-, y-, and z-axes, respectively. e, f, g, h, i, and j, Maps of the six components of the full strain tensor (ε_{xx}, ε_{yy}, ε_{zz}, ε_{xy}, ε_{xz}, and ε_{yz}). The procedure to calculate the atomic displacement field and the full strain tensor using the MD data was identical to that used in the analysis of the experimental data. The MD simulation of the carbon-containing tungsten tip shows expansion and compression along the [0$\bar{1}$1] and [100] respectively, in agreement with the experimental results (Fig. 3).

Compared with discrete tomography that requires a priori structural information to determine the 3D surface morphology of a small crystalline nanoparticle at atomic resolution [14], this method does not make assumptions about the crystal structure of the sample, thus allowing precise measurements of the atomic displacement field and the full strain tensor in three dimensions. Furthermore, the sample geometry of this experiment is very similar to that of atom probe tomography [49] and can be widely applied to other materials. While this experiment resolved the positions of individual tungsten atoms, numerical simulation results indicate that this method can be used to determine the 3D positions of other types of individual atoms, including silicon and oxygen atoms in amorphous materials [72].

CHAPTER 7

Towards Z-contrast in atomic resolution tomography

7.1 Motivation

Bimetallic FePt nanoparticles have found application in high-density magnetic memory devices due to their large uniaxial magnetic anisotropy and overall stability [73]. These particles form an ordered $L1_0$ state (Figure 7.1), in which the Fe and Pt segregate into alternately stacked (100) planes. While it is well known that the magnetic anisotropy in this material arises from the $L1_0$ phase [73], to understand the functionality of this material, it is necessary to determine the atomic arrangement and defect structures in the interior of the particles. Not only are physical defects in the crystal structure, such as those studied in Chapter 4 important, but ordering defects will also affect the magnetic susceptibility of these particles. Therefore it is not only necessary to determine the atomic positions of the atoms within these particles, but also the atomic species. To do this, we have undertaken an atomic resolution tomographic study of 8-10 nm bimetallic

FePt nanoparticles in the $L1_0$ state. This work employs the moethods described in Chapter 5 to collect tilt series in a conventional single tilt geometry using an aberration corrected microscope.

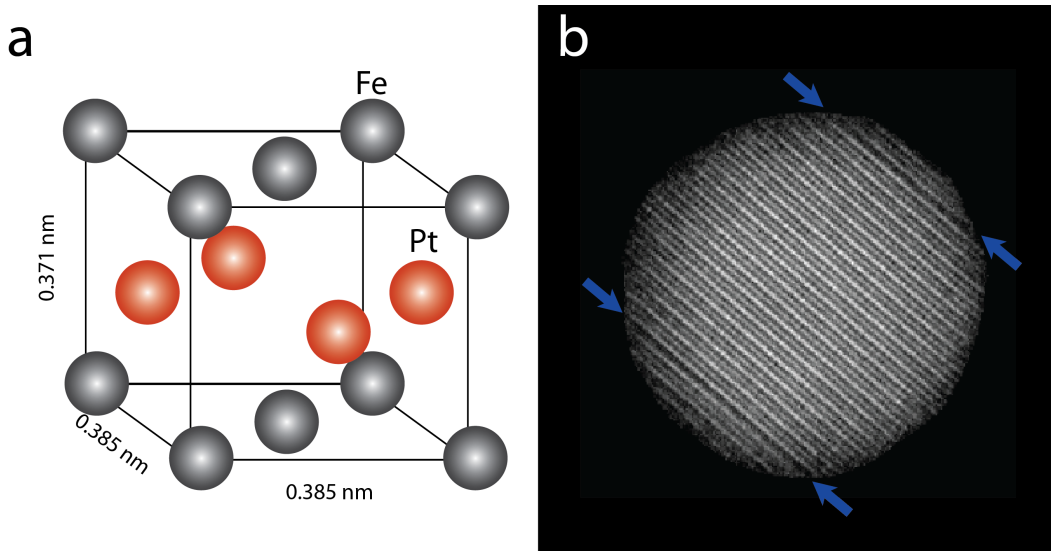

Figure 7.1: a) A schematic of the $L1_0$ unit cell. The crystal structure of this material consists of a modified fcc, wherein along one axis, Fe and Pt segregate into alternating sheets. Along this axis, the unit cell is slightly compressed [74]. b) An ADF-STEM image of an FePt particle, after being annealed to induce the $L1_0$ phase. Due to the native Z contrast of ADF-STEM, platinum atoms appear brighter than iron, and the species segregation is apparent in the image. Blue arrows indicate a feature in the particle where a row of dim atoms appears, with spacing that is not consistent with the $L1_0$ state.

7.2 Data collection on the TEAM I microscope

To study the FePt particles, several tilt series taken on the TEAM I were reconstructed. Samples were prepared of 8-10 nm FePt particles from solution, which were then dropcast and subsequently annealed to produce an $L1_0$ phase. The substrate was a custom silicon nitride grid (Fig. 5.3) designed to be mounted in

a holder for the TEAM I stage. Each particle under study was 8-10 nm in size.

Data were acquired using the TEAM I at a 300 kV accelerating voltage in ADF-STEM mode (convergence semi-angle: 30 mrad; aberration-corrected probe size: 50 pm; beam current: <55 pA). Each tilt series consists of 70 or more projections. The pixel size is ∼0.4 Å in each 512×512 image. To enhance signal to noise further and to reduce the effects of drift, multiple fast images were taken at each tilt angle. A 30mrad convergence angle was used for all data sets. To examine the effect of inner detector angle, two different inner angles were used: 38 mrad and 48 mrad.

Preprocessing the images involved correcting for scanning coil distortion. This time, a distortion matrix was calculated based on a silicon calibration sample. The sample was imaged along the <100>direction under similar imaging conditions to the data sets. Based on the Bragg peaks of the Fourier transform and their known symmetry, a correction matrix was calculated and the data was corrected using Fourier methods [57]. The repeated images for each angle were averaged using cross correlation.

The images were aligned by the CM method as described in Chapters 3 and 4. The aligned projections were then reconstructed by EST as described in Section 1.2.3. Figure 7.2 shows an experimental projection and a corresponding reconstructed slice.

7.3 Differentiating between atomic species and identifying ordering defects

Despite a larger missing wedge than the data from UCLA, the FePt reconstructions exhibit excellent resolution and contrast, even in the beam (missing wedge) direction. Figure 7.3 shows a projection of a reconstruction (38 mrad convergence

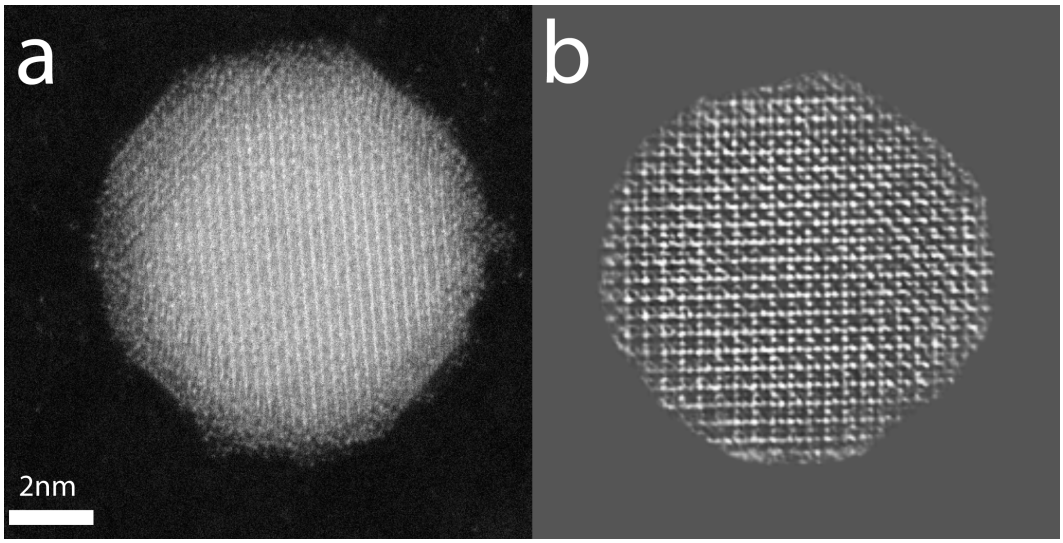

Figure 7.2: (a) The experimental 0° projection of an FePt dataset. (b) A corresponding 2.5Å slice through the reconstruction at the same orientation. Atoms are clearly visible in the reconstruction.

angle) and its Fourier transform, with the missing wedge direction indicated. As indicated in Figure 7.3b, the EST algorithm has successfully recovered missing information in the missing wedge.

Figure 7.4 shows another 2.5Å slice through the reconstruction. In this slice, which has been weakly Wiener filtered ($\lambda = 1$), atoms of different intensity are visible (Fig. 7.4b). The brighter atoms in the reconstruction correspond to platinum, and the lighter atoms are iron. In Figure 7.4c, labeling the species indicates that an antiphase boundary is present in this area. This type of ordering defect would not be visible without Z contrast in the reconstruction.

As a preliminary way to differentiate between atomic species in the reconstruction, the intensities of the traced atoms in the reconstruction can be ranked, with the higher intensities corresponding to Pt. Figure 7.5 shows three orthogonal slices through a reconstruction. Although this method needs verification, it is clear that the interior of the particle is quite complicated, and not a simple single crystal in the $L1_0$ as might appear in Figures 7.1b and 7.2. Figure 7.6 shows a feature

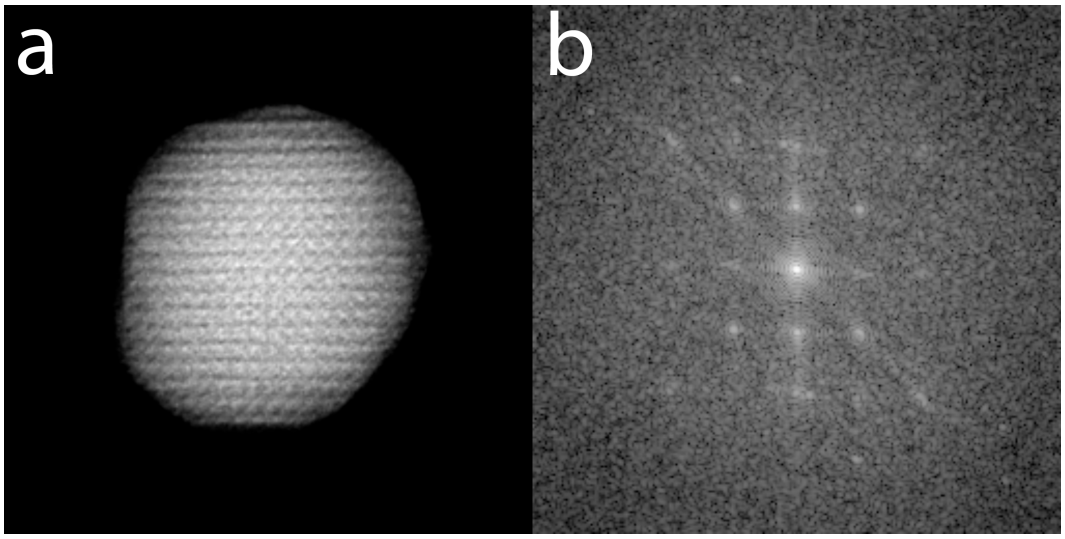

Figure 7.3: A projection (a) and its Fourier transform (b) of a reconstructed FePt nanoparticle. The missing wedge direction is vertical. In (b), Bragg peaks appear in the missing wedge direction, indicating that the EST algorithm has recovered information that was not included in the experimental data set.

that corresponds to the unusually spaced dim area in Figure 7.1b. It appears that these features correspond to a missing row of Fe atoms, possibly with a carbon substitution between the Pt rows.

7.4 Summary

Due to the native Z contrast in STEM, differentiating between atomic species in atomic resolution reconstructions is theoretically possible [72]. While methods have not yet been optimized to label all the atoms in the reconstructions shown here, work is underway to perfect these calculations.

This experiment demonstrates that while a needle geometry can remove the missing wedge problem (Chapter 6), given sufficiently high quality input data, missing wedge information can still be recovered by using the EST iterative algorithm.

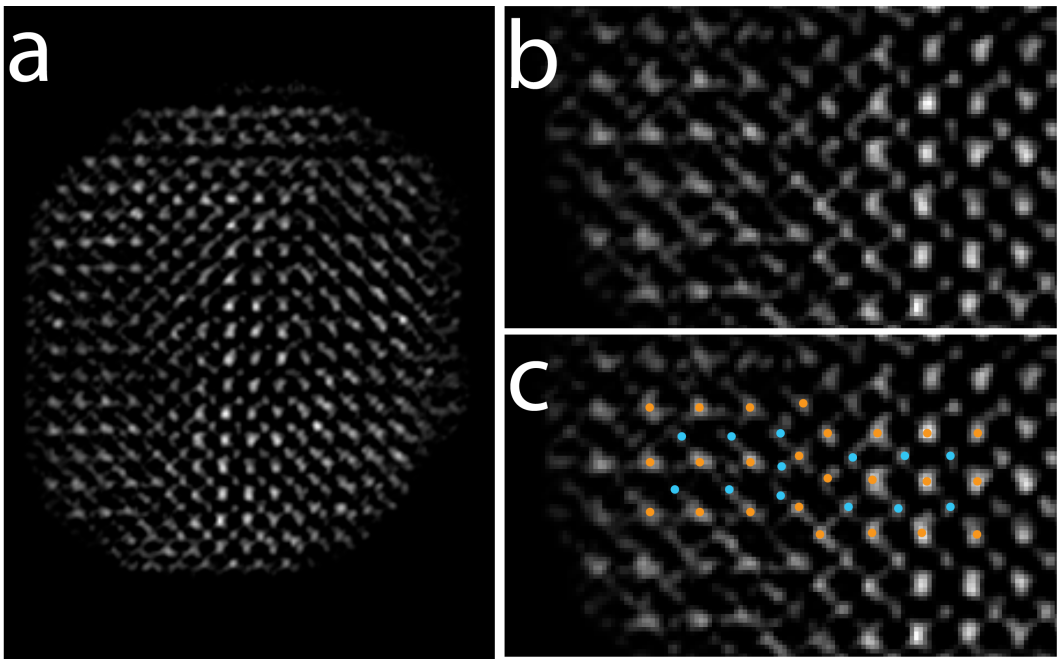

Figure 7.4: a) a 2.5 Å slice through the FePt reconstruction, which has been gently Wiener filtered. b) and c), the same zoomed in section of the slice. In b) Pt atoms are clearly brighter than the Fe. In c), the atoms positions have been indicated by orange (Pt) and blue (Fe). In b) and c), it is clear that there is an antiphase boundary present.

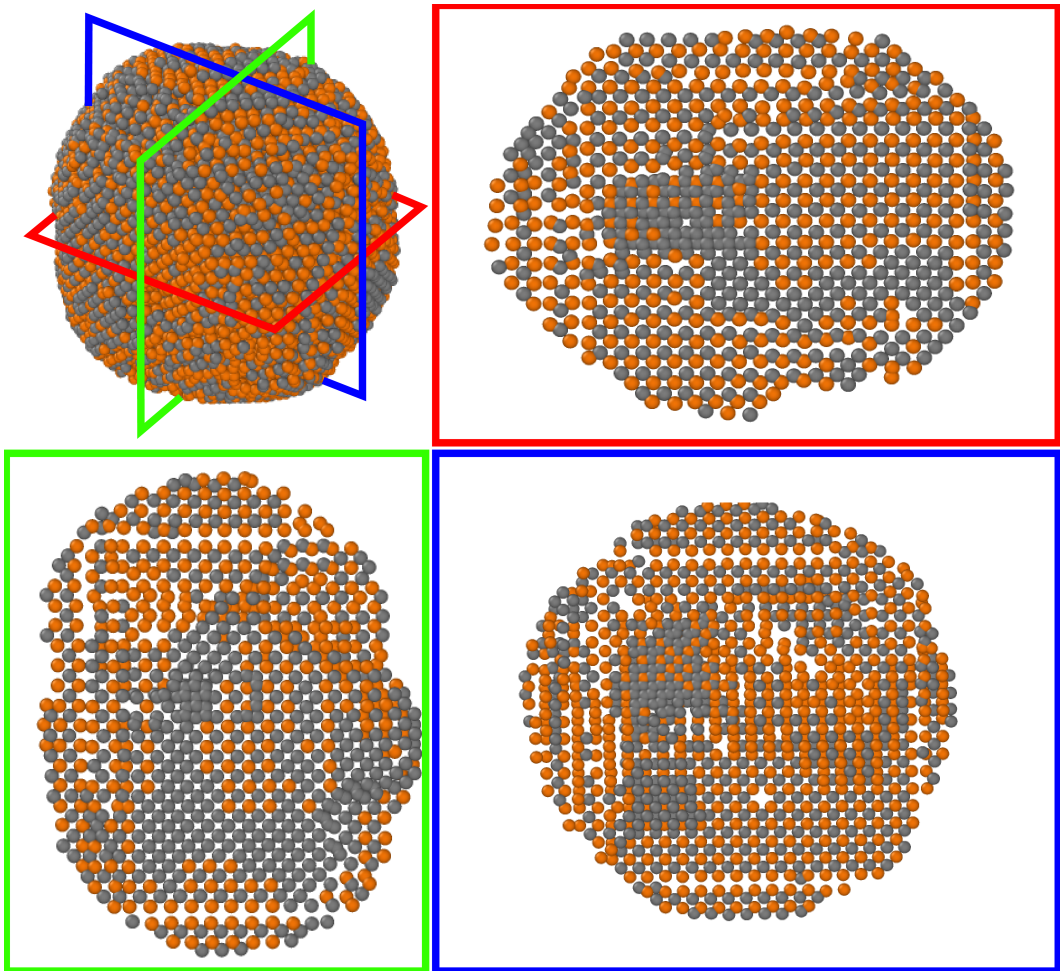

Figure 7.5: Three orthogonal slices through the traced and labeled FePt reconstruction. The internal structure exhibits both structural and ordering defects, and is very complicated, with multiple grains and directions of $L1_0$ ordering.

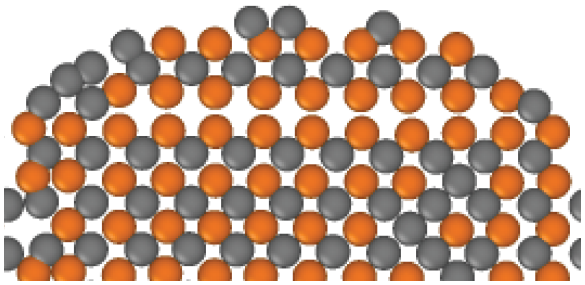

Figure 7.6: The feature seen in projection in 7.1b corresponds to a missing row of Fe atoms.

CHAPTER 8

Conclusions

8.1 Thesis summary

This thesis has described the experimental implementation of atomic resolution electron tomography. Chapter 2 discussed the development of atomic scale electron tomography on an uncorrected electron microscope. Chapters 3 and 4 are applications of this technique. Chapter 3 is a proof of principle demonstration of high resolution electron tomography using EST, which reconstructs a gold nanoparticle at 2.4 Å resolution, revealing the interior twin boundaries and grain structure. In chapter 4, improved data acquisition and a Bragg filtering technique revealed edge and screw dislocations as well as stacking faults within a decahedral platinum nanoparticle. This is first time the atomic arrangement these features has been experimentally visualized in three dimensions. These two chapters demonstrate the power of the electron tomography methodology developed in Chapter 2.

Next, considerations for aberration corrected tomography were presented in Chapter 5. Not only were the additional requirements of an aberration corrected microscope discussed, but a novel needle sample geometry was introduced. The

application of aberration corrected electron tomography to a needle sample is presented in Chapter 6. The results of this experiment were an atomic resolution reconstruction in which the position of every atom in the region of interest is precisely identified. From these positions, high resolution displacement and strain maps can be identified. Furthermore, a point defect was observed in 3D for the first time. This work represents the highest resolution tomographic reconstruction ever demonstrated.

Chapter 7 discussed aberration corrected electron tomography applied to a more conventional sample geometry. This work demonstrates that even with a significant missing wedge, the improved contrast and resolution of this experiment can reconstruct the atoms in a nanoparticle and recover high resolution information in the missing wedge. This work is ongoing as efforts to identify the atomic species in the bimetallic particle are still underway.

8.2 Future work

The ability to characterize materials in three dimensions at atomic resolution opens the door to many future experiments. Currently, work is underway to characterize nanomaterials at atomic resolution while including information about atomic species within the sample. Once this is accomplished, systems such as interfaces and core shell nanoparticles can be studied in great detail. Other applications of this technique include the study of amorphous or quasicrystalline materials. Combining these experimental 3D atomic maps with computational techniques such as molecular dynamics simulations and density functional theory calculations not only gives information about the energetics of the specific atomic arrangement, but can also test the validity of these techniques.

APPENDIX A

Derivations

A.1 The projection-slice theorem

Given an object A in 3D Cartesian space, the projection at an angle $\theta = 0$ is

$$P(x,z) = \int_{-\infty}^{+\infty} A(x,y,z)dy \tag{A.1}$$

Where y is the projection direction and z is the rotation axis. The 2D Fourier transform of P is then

$$\mathcal{F}(P(x,z)) = \iint_{-\infty}^{+\infty} \Big[\int_{-\infty}^{+\infty} A(x,y,z)dy \Big] e^{-2i\pi(xk_x+zk_z)}dxdz. \tag{A.2}$$

Conversely, the 3D Fourier transform of the object is

$$\mathcal{F}_{3D,A}(k_x,k_y,k_z) = \mathcal{F}(A(x,y,z)) = \iiint_{-\infty}^{+\infty} A(x,y,z)e^{-2i\pi(xk_x+yk_y+zk_z)}dxdydz \tag{A.3}$$

and a slice through the $\mathcal{F}_{3D}(A(x,y,z))$ at $\theta = 0$ is

$$\begin{aligned}\mathcal{F}_{3D,A}(k_x,0,k_z) &= \iiint_{-\infty}^{+\infty} A(x,y,z)e^{-2i\pi(xk_x+zk_z)}dxdydz \\ &= \iint_{-\infty}^{+\infty}\Big[\int_{-\infty}^{+\infty} A(x,y,z)dy\Big]e^{-2i\pi(xk_x+zk_z)}dxdz \\ &= \mathcal{F}(P(x,z))\end{aligned} \tag{A.4}$$

This is easily generalized to non-zero θ by letting $x \to x'$ and $y \to y'$, where $x' = x\cos\theta - y\sin\theta$, $y' = x\sin(\theta) + y\cos\theta$, and $dy' = -\sin\theta dy$

A.2 Stage angles required to rotate to a set of equally sloped angles about a specified axis

Derivation of the relationship between stage angles (α, γ) and EST angles (ϕ)

1. **Definitions**

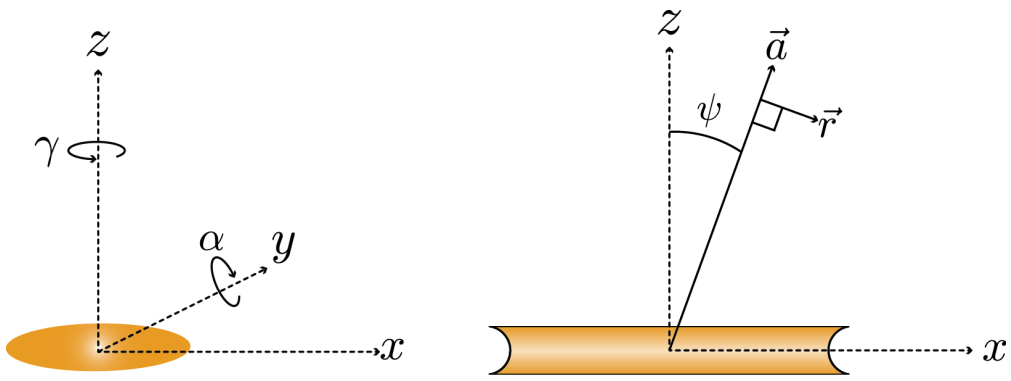

Figure A.1: Geometry of the tungsten tip tomography setup.

(a) y is the tilt axis, α rotation is about y

(b) z is the vertical axis, γ rotation is about z

(c) $\vec{a}$ is the axis we want to rotate about

(d) $\vec{r}$ is $\perp$ to $\vec{a}$ and its projection defines the tomography tilt direction

(e) ψ is the angle between $\vec{a}$ and the horizontal (z) axis

(f) Both $\vec{a}$ and $\vec{r}$ initially have zero y component:

$$\vec{a} = \begin{pmatrix} \cos\psi \\ 0 \\ -\sin\psi \end{pmatrix}, \vec{r} = \begin{pmatrix} \sin\psi \\ 0 \\ \cos\psi \end{pmatrix}$$

2. **Relationship between α, γ and ϕ**

γ and α rotation matrices are

$$\mathrm{R}_\gamma = \begin{pmatrix} \cos\gamma & -\sin\gamma & 0 \\ \sin\gamma & \cos\gamma & 0 \\ 0 & 0 & 1 \end{pmatrix} \text{ and } \mathrm{R}_\alpha = \begin{pmatrix} \cos\alpha & 0 & -\sin\alpha \\ 0 & 1 & 0 \\ \sin\alpha & 0 & \cos\alpha \end{pmatrix}$$

Then can write

$\mathrm{R}_\alpha \mathrm{R}_\gamma \vec{u} = \mathrm{R}_\alpha \vec{u}' = \vec{u}''$

For simplicity let $y = 0$ for $\vec{u}$. Then

$$\vec{u}' = \begin{pmatrix} \cos\gamma & -\sin\gamma & 0 \\ \sin\gamma & \cos\gamma & 0 \\ 0 & 0 & 1 \end{pmatrix} \begin{pmatrix} x \\ 0 \\ z \end{pmatrix} = \begin{pmatrix} x\cos\gamma \\ x\sin\gamma \\ z \end{pmatrix} = \begin{pmatrix} x' \\ y' \\ z' \end{pmatrix}$$

$$\text{and } \vec{u}'' = \begin{pmatrix} \cos\alpha & 0 & -\sin\alpha \\ 0 & 1 & 0 \\ \sin\alpha & 0 & \cos\alpha \end{pmatrix} \begin{pmatrix} x\cos\gamma \\ x\sin\gamma \\ z \end{pmatrix} = \begin{pmatrix} x\cos\alpha\cos\gamma - z\sin\alpha \\ x\sin\gamma \\ x\sin\alpha\cos\gamma + z\cos\gamma \end{pmatrix}$$

Now demand that

1. $\mathrm{R}_\alpha \mathrm{R}_\gamma \vec{a}|_z = 0$

2. $\mathrm{R}_\alpha \mathrm{R}_\gamma \vec{r}|_z = \cos\phi$,where ϕ is the tomography angle.

This gives

I. $\sin\alpha\cos\gamma\sin\psi + \cos\alpha\cos\psi = 0$

II. $\sin\alpha\cos\gamma\sin\psi - \cos\alpha\sin\psi = \cos\phi$

Solve for $\cos\gamma$ and equate **I** and **II**:

III. $\cos\gamma = -\dfrac{\cos\alpha\cos\psi}{\sin\alpha\sin\psi} = \dfrac{\cos\phi + \cos\alpha\sin\psi}{\sin\alpha\cos\psi}$

Solve for $\cos\alpha$ in terms of ϕ and ψ:

IV. $-\dfrac{\cos\alpha}{\sin\psi} = \cos\phi \rightarrow \cos\alpha = -\cos\phi\sin\psi$

Then from **III** and **IV**, solve for $\cos\gamma$ in terms of ϕ and ψ:

$$\cos\gamma = \frac{\cos\phi\cos\psi}{\sin\alpha}$$

Now have the required stage angles for a given set of ϕ with a given offset ψ:

$$\boxed{\begin{array}{l}\cos\alpha = -\cos\phi\sin\psi \\ \\ \cos\gamma = \dfrac{\cos\phi\cos\psi}{\sin\alpha}\end{array}}.$$

Bibliography

[1] David B Williams and C Barry Carter. *The Transmission Electron Microscope*. Springer, 1996.

[2] A Bogner, P-H Jouneau, Gilbert Thollet, D Basset, and Catherine Gauthier. A history of scanning electron microscopy developments: towards wet-STEM imaging. *Micron*, 38(4):390–401, 2007.

[3] J-O Malm and MA O'keefe. Deceptive lattice spacings in high-resolution micrographs of metal nanoparticles. *Ultramicroscopy*, 68(1):13–23, 1997.

[4] Rolf Erni. Aberration-corrected imaging in transmission electron microscopy. *Imperial College Press*, 3:1, 2010.

[5] Peter W Hawkes and John CH Spence. *Science of Microscopy*. Wiley Online Library, 2007.

[6] O Scherzer. Some defects of electron lenses. *Z. Phys*, 101:593–603, 1936.

[7] Harald H Rose. Historical aspects of aberration correction. *Journal of Electron Microscopy*, page dfp012, 2009.

[8] O Scherzer. The theoretical resolution limit of the electron microscope. *Journal of Applied Physics*, 20(1):20–29, 1949.

[9] Maximilian Haider, Stephan Uhlemann, Eugen Schwan, Harald Rose, Bernd

Kabius, and Knut Urban. Electron microscopy image enhanced. *Nature*, 392 (6678):768–769, 1998.

[10] Max Haider, Harald Rose, Stephan Uhlemann, Eugen Schwan, Bernd Kabius, and Knut Urban. A spherical-aberration-corrected 200 kV transmission electron microscope. *Ultramicroscopy*, 75(1):53–60, 1998.

[11] Huolin L Xin, Varat Intaraprasonk, and David A Muller. Depth sectioning of individual dopant atoms with aberration-corrected scanning transmission electron microscopy. *Applied Physics Letters*, 92(1):013125, 2008.

[12] Huolin L Xin and David A Muller. Aberration-corrected ADF-STEM depth sectioning and prospects for reliable 3d imaging in S/TEM. *Journal of Electron Microscopy*, 58(3):157–165, 2009.

[13] J. Frank. *Electron Tomography*. Plenum, 1992.

[14] Sandra Van Aert, Kees J Batenburg, Marta D Rossell, Rolf Erni, and Gustaaf Van Tendeloo. Three-dimensional atomic imaging of crystalline nanoparticles. *Nature*, 470(7334):374–377, 2011.

[15] C.L. Jia, S.B. Mi, J. Barthel, D.W. Wang, R.E. Dunin-Borkowski, K.W. Urban, and A. Thust. Determination of the 3d shape of a nanoscale crystal with atomic resolution from a single image. *Nature Materials*, 13(11):1044–9, 2014.

[16] Paul A Midgley and Rafal E Dunin-Borkowski. Electron tomography and holography in materials science. *Nature Materials*, 8(4):271–280, 2009.

[17] I Arslan, TJV Yates, ND Browning, and PA Midgley. Embedded nanostructures revealed in three dimensions. *Science*, 309(5744):2195–2198, 2005.

[18] Akihiro Kumao, Hatsujiro Hashimoto, and Kensuke Shiraishi. Studies on

specimen contamination by transmission electron microscopy. *Journal of Electron Microscopy*, 30(3):161–170, 1981.

[19] RF Egerton, P Li, and M Malac. Radiation damage in the TEM and SEM. *Micron*, 35(6):399–409, 2004.

[20] Edwin Lee, Benjamin P Fahimian, Cristina V Iancu, Christian Suloway, Gavin E Murphy, Elizabeth R Wright, Daniel Castaño-Díez, Grant J Jensen, and Jianwei Miao. Radiation dose reduction and image enhancement in biological imaging through equally-sloped tomography. *Journal of Structural Biology*, 164(2):221–227, 2008.

[21] G.T. Herman. *Image Reconstruction from Projections: The Fundamentals of Computerized Tomography*. Computer Science and Applied Mathematics Series. Academic Press, 1980.

[22] Stanley R Deans. *The Radon transform and some of its applications*. Courier Corporation, 2007.

[23] Peter Gilbert. Iterative methods for the three-dimensional reconstruction of an object from projections. *Journal of Theoretical Biology*, 36(1):105–117, 1972.

[24] William L Briggs et al. *The DFT: An Owners' Manual for the Discrete Fourier Transform*. Siam, 1995.

[25] Jianwei Miao, Friedrich Förster, and Ofer Levi. Equally sloped tomography with oversampling reconstruction. *Physical Review B*, 72(5):052103, 2005.

[26] Amir Averbuch, Ronald R Coifman, David L Donoho, Moshe Israeli, and Yoel Shkolnisky. A framework for discrete integral transformations i-the pseudopolar fourier transform. *SIAM Journal on Scientific Computing*, 30(2):764–784, 2008.

[27] Benjamin P Fahimian, Yu Mao, Peter Cloetens, and Jianwei Miao. Low-dose X-ray phase-contrast and absorption CT using equally sloped tomography. *Physics in Medicine and Biology*, 55(18):5383, 2010.

[28] Yu Mao, Benjamin P Fahimian, Stanley J Osher, and Jianwei Miao. Development and optimization of regularized tomographic reconstruction algorithms utilizing equally-sloped tomography. *IEEE Transactions on Image Processing*, 19(5):1259–1268, 2010.

[29] David H Bailey and Paul N Swarztrauber. The fractional Fourier transform and applications. *SIAM Review*, 33(3):389–404, 1991.

[30] MC Scott, Chien-Chun Chen, Matthew Mecklenburg, Chun Zhu, Rui Xu, Peter Ercius, Ulrich Dahmen, BC Regan, and Jianwei Miao. Electron tomography at 2.4-angstrom resolution. *Nature*, 483(7390):444–447, 2012.

[31] Chien-Chun Chen, Chun Zhu, Edward R White, Chin-Yi Chiu, MC Scott, BC Regan, Laurence D Marks, Yu Huang, and Jianwei Miao. Three-dimensional imaging of dislocations in a nanoparticle at atomic resolution. *Nature*, 496(7443):74–77, 2013.

[32] Thomas C Isabell, Paul E Fischione, Catherine O'Keefe, Murat U Guruz, and Vinayak P Dravid. Plasma cleaning and its applications for electron microscopy. *Microscopy and Microanalysis*, 5(02):126–135, 1999.

[33] T Irie, G Yamada, and M Sonoda. Natural frequencies of square membrane and square plate with rounded corners. *Journal of Sound and Vibration*, 86 (3):442–448, 1983.

[34] RF Egerton. Control of radiation damage in the TEM. *Ultramicroscopy*, 127:100–108, 2013.

[35] AR Lupini, P Wang, PD Nellist, AI Kirkland, and SJ Pennycook. Aberra-

tion measurement using the ronchigram contrast transfer function. *Ultramicroscopy*, 110(7):891–898, 2010.

[36] A Howie. Diffraction channelling of fast electrons and positrons in crystals. *Philosophical Magazine*, 14(128):223–237, 1966.

[37] John Maxwell Cowley. *Diffraction Physics*. Elsevier, 1995.

[38] RF Egerton, R McLeod, F Wang, and M Malac. Basic questions related to electron-induced sputtering in the TEM. *Ultramicroscopy*, 110(8):991–997, 2010.

[39] Vladan Lucic, Friedrich Förster, and Wolfgang Baumeister. Structural studies by electron tomography: from cells to molecules. *Annu. Rev. Biochem.*, 74: 833–865, 2005.

[40] PA Midgley and Matthew Weyland. 3d electron microscopy in the physical sciences: the development of Z-contrast and EFTEM tomography. *Ultramicroscopy*, 96(3):413–431, 2003.

[41] Amanda S Barnard, Neil P Young, Angus I Kirkland, Marijn A Van Huis, and Huifang Xu. Nanogold: a quantitative phase map. *ACS Nano*, 3(6): 1431–1436, 2009.

[42] Ilke Arslan, Emmanuelle A Marquis, Mark Homer, Michelle A Hekmaty, and Norman C Bartelt. Towards better 3-d reconstructions by combining electron tomography and atom-probe tomography. *Ultramicroscopy*, 108(12): 1579–1585, 2008.

[43] D.J. Bacon D. Hull. *Introduction to Dislocations 5th ed.* Butterworth-Heinemann, 2011.

[44] Shuji Nakamura. The roles of structural imperfections in ingan-based blue

light-emitting diodes and laser diodes. *Science*, 281(5379):956–961, 1998.

[45] P Hirsch, D Cockayne, J Spence, and M Whelan. 50 years of TEM of dislocations: Past, present and future. *Philosophical Magazine*, 86(29-31): 4519–4528, 2006.

[46] S.J. Pennycook and P.D. Nellist. *Scanning Transmission Electron Microscopy: Imaging and Analysis*. Springer, 2011.

[47] GC Hua, N Otsuka, DC Grillo, Y Fan, J Han, MD Ringle, RL Gunshor, M Hovinen, and AV Nurmikko. Microstructure study of a degraded pseudomorphic separate confinement heterostructure blue-green laser diode. *Applied Physics Letters*, 65(11):1331–1333, 1994.

[48] W Ludwig, P Cloetens, J Härtwig, J Baruchel, B Hamelin, and P Bastie. Three-dimensional imaging of crystal defects by topo-tomography. *Journal of Applied Crystallography*, 34(5):602–607, 2001.

[49] Thomas F Kelly and Michael K Miller. Atom probe tomography. *Review of Scientific Instruments*, 78(3):031101, 2007.

[50] Chin-Yi Chiu, Yujing Li, Lingyan Ruan, Xingchen Ye, Christopher B Murray, and Yu Huang. Platinum nanocrystals selectively shaped using facet-specific peptide sequences. *Nature Chemistry*, 3(5):393–399, 2011.

[51] Huolin L Xin, Peter Ercius, Kevin J Hughes, James R Engstrom, and David A Muller. Three-dimensional imaging of pore structures inside low-κ dielectrics. *Applied Physics Letters*, 96(22):223108, 2010.

[52] A Howie and LD Marks. Elastic strains and the energy balance for multiply twinned particles. *Philosophical Magazine A*, 49(1):95–109, 1984.

[53] L Lu, R Schwaiger, ZW Shan, M Dao, K Lu, and S Suresh. Nano-sized twins

induce high rate sensitivity of flow stress in pure copper. *Acta Materialia*, 53 (7):2169–2179, 2005.

[54] TJ Balk and KJ Hemker. High resolution transmission electron microscopy of dislocation core dissociations in gold and iridium. *Philosophical Magazine A*, 81(6):1507–1531, 2001.

[55] Peter Ercius, Markus Boese, Thomas Duden, and Ulrich Dahmen. Operation of team i in a user environment at ncem. *Microscopy and Microanalysis*, 18 (04):676–683, 2012.

[56] JP Ibe, PP Bey Jr, SL Brandow, RA Brizzolara, NA Burnham, DP DiLella, KP Lee, CRK Marrian, and RJ Colton. On the electrochemical etching of tips for scanning tunneling microscopy. *Journal of Vacuum Science & Technology A*, 8(4):3570–3575, 1990.

[57] Kieran G Larkin, Michael A Oldfield, and Hanno Klemm. Fast fourier method for the accurate rotation of sampled images. *Optics Communications*, 139(1): 99–106, 1997.

[58] Anthony JG Hey. Feynman and computation. *Reading, MA: Perseus*, 1999.

[59] Maximilian Haider, Stephan Uhlemann, Eugen Schwan, Harald Rose, Bernd Kabius, and Knut Urban. Electron microscopy image enhanced. *Nature*, 392 (6678):768–769, 1998.

[60] PE Batson, Niklas Dellby, and OL Krivanek. Sub-angstrom resolution using aberration corrected electron optics. *Nature*, 418(6898):617–620, 2002.

[61] Rolf Erni, Marta D Rossell, Christian Kisielowski, and Ulrich Dahmen. Atomic-resolution imaging with a sub-50-pm electron probe. *Physical Review Letters*, 102(9):096101, 2009.

[62] Maia Azubel, Jaakko Koivisto, Sami Malola, David Bushnell, Greg L Hura, Ai Leen Koh, Hironori Tsunoyama, Tatsuya Tsukuda, Mika Pettersson, Hannu Häkkinen, et al. Electron microscopy of gold nanoparticles at atomic resolution. *Science*, 345(6199):909–912, 2014.

[63] LD Marks. Wiener-filter enhancement of noisy hrem images. *Ultramicroscopy*, 62(1):43–52, 1996.

[64] Yue-Lin Liu, Hong-Bo Zhou, Shuo Jin, Ying Zhang, and Guang-Hong Lu. Dissolution and diffusion properties of carbon in tungsten. *Journal of Physics: Condensed Matter*, 22(44):445504, 2010.

[65] Martin J Hÿtch and Andrew M Minor. Observing and measuring strain in nanostructures and devices with transmission electron microscopy. *MRS Bulletin*, 39(02):138–146, 2014.

[66] Martin Hÿtch, Florent Houdellier, Florian Hüe, and Etienne Snoeck. Nanoscale holographic interferometry for strain measurements in electronic devices. *Nature*, 453(7198):1086–1089, 2008.

[67] Jamie H Warner, Neil P Young, Angus I Kirkland, and G Andrew D Briggs. Resolving strain in carbon nanotubes at the atomic level. *Nature Materials*, 10(12):958–962, 2011.

[68] Jianwei Miao, Pambos Charalambous, Janos Kirz, and David Sayre. Extending the methodology of X-ray crystallography to allow imaging of micrometre-sized non-crystalline specimens. *Nature*, 400(6742):342–344, 1999.

[69] Marcus C Newton, Steven J Leake, Ross Harder, and Ian K Robinson. Three-dimensional imaging of strain in a single ZnO nanorod. *Nature Materials*, 9 (2):120–124, 2010.

[70] BC Larson, Wenge Yang, GE Ice, JD Budai, and JZ Tischler. Three-dimensional X-ray structural microscopy with submicrometre resolution. *Nature*, 415(6874):887–890, 2002.

[71] Wenge Yang, Xiaojing Huang, Ross Harder, Jesse N Clark, Ian K Robinson, and Ho-kwang Mao. Coherent diffraction imaging of nanoscale strain evolution in a single crystal under high pressure. *Nature Communications*, 4:1680, 2013.

[72] Chun Zhu, Chien-Chun Chen, Jincheng Du, Michael R Sawaya, MC Scott, Peter Ercius, James Ciston, and Jianwei Miao. Towards three-dimensional structural determination of amorphous materials at atomic resolution. *Physical Review B*, 88(10):100201, 2013.

[73] Shouheng Sun, Christopher B Murray, Dieter Weller, Liesl Folks, and Andreas Moser. Monodisperse FePt nanoparticles and ferromagnetic FePt nanocrystal superlattices. *Science*, 287(5460):1989–1992, 2000.

[74] B. Aktas, L. Tagirov, and F. Mikailov. *Magnetic Nanostructures*. Springer Series in Materials Science. Springer Berlin Heidelberg, 2007.